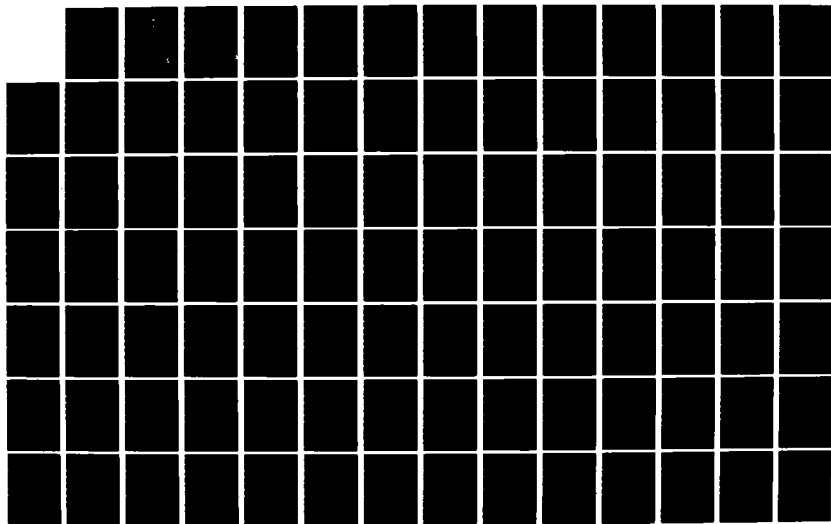AD-A124 679   FAR-INFRARED PHOTOCONDUCTIVITY OF HIGH PURITY N-GAAS IN   1/2
               A MAGNETIC FIELD..(U) AIR FORCE INST OF TECH
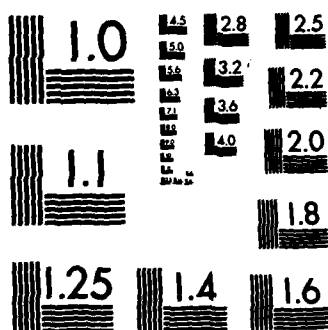   WRIGHT-PATTERSON AFB OH SCHOOL OF ENGI..   D P SVETZ
UNCLASSIFIED   DEC 82 AFIT/GEP/PH/82D-22   F/G 20/12   NL

1.0

4.5
5.0
5.6
6.3
7.1

2.8

2.5

3.2

2.2

3.6

1.1

4.0

2.0

1.8

1.25

1.4

1.6

MICROCOPY RESOLUTION TEST CHART
NATIONAL BUREAU OF STANDARDS-1963-A

AD A 124679

FAR-INFRARED PHOTOCONDUCTIVITY OF
HIGH PURITY n-GaAs IN A MAGNETIC
FIELD USING RAPID-SCAN FOURIER
TRANSFORM SPECTROSCOPY

THESIS

AFIT/GEP/PH/8 D-22   David P. Svetz
                            Captain   USAF

DTIC
SELECTE
FEB 2 2 1983

A

DEPARTMENT OF THE AIR FORCE

AIR UNIVERSITY (ATC)

AIR FORCE INSTITUTE OF TECHNOLOGY

Wright-Patterson Air Force Base, Ohio

C FILE COPY

83   02   022 155

FAR-INFRARED PHOTOCONDUCTIVITY OF
HIGH PURITY n-GaAs IN A MAGNETIC
FIELD USING RAPID-SCAN FOURIER
TRANSFORM SPECTROSCOPY

THESIS

AFIT/GEP/PH/82D-22   David P. Svetz
                          Captain   USAF

DTIC
ELECTE
FEB 2 2 1983

A

Approved for public release; distribution unlimited

FAR-INFRARED PHOTOCONDUCTIVITY OF HIGH PURITY

n-GaAs IN A MAGNETIC FIELD USING

RAPID-SCAN FOURIER TRANSFORM

SPECTROSCOPY

THESIS

Presented to the Faculty of the School of Engineering

of the Air Force Institute of Technology

Air University

in Partial Fulfillment of the

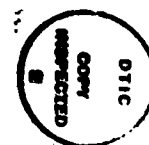Requirements for the Degree of

Master of Science

by

David P. Svetz, B.S.

Captain   USAF

Graduate Engineering Physics

December 1982

Approved for public release; distribution unlimited

Preface

This thesis summarizes my work over the summer on far-infrared photoconductivity of high purity GaAs in a magnetic field. This project was a new area of experimental research for the Avionics Laboratory, Wright-Patterson AFB. Previously samples were sent to MIT or the University of Illinois to be characterized. This experimental apparatus will complement the other areas of research on GaAs at the Avionics Laboratory.

I learned a great deal of experimental physics during my work and am greatly indebted to a number of individuals. Dr. Don Shankland (AFIT advisor) and Dr. Bill Theis (Laboratory advisor) provided the guidance, expertise, patience and encouragement for my work. Dr. Cole Litton provided his knowledge and assistance. Dr. Dave Look provided the samples for the experiment and his knowledge. Gene Johnson drafted and fabricated equipment needed for the project. John Hoelscher helped me to set up and operate the experimental equipment. Dr. George Norris and Tim Cooper also provided assistance in the project.

The experiment was stopped short of its full completion. The first magnet used broke and a second was taken out of storage to continue the experiment. The experiment ended prematurely when the second magnet dewar exploded.

My deepest appreciation is for Jeanne, my wife, who always gave me support and was able to put up with my long hours of work.

Contents

Contents

Contents

List of Figures

List of Tables

List of Symbols

A^O Angstrom (10^{-10} m)

a_B Bohr radius for an electron

a_O Lattice spacing of the semiconductor

AFN   Three letter computer command for apodization functions

APE   Three letter computer command for the iris aperture

BX   Boxcar apodization function

cm^{-1} Inverse centimeters, wavenumber

CS   Cosine apodization function

DSV   Spherical volume at the center of a magnet's bore

E_D Donor binding energy

f_1, f_2 Focal lengths

f_{1s-2p} Oscillator strength

FL   Full aperture

FPx   Three letter command to Fourier process the given data file (x=B(Background file),D(Destination file),R(Reference file),S(Sample file))

FTIR   Fourier transform infrared

g_1 Degeneracy of the ground state of the impurity center

GaAs   Gallium Arsenide

Ge   Germanium

G_S Ground wire for the GaAs sample

HeNe   Helium-Neon

HG   Happ-Genzel apodization function

Hg	Mercury
I-V	Current-Voltage
kG	10^3 gauss
m^*	Electron effective mass
m_D^*	Conduction band density-of-states effective mass
m_o^*	Electron effective mass at the bottom of the conduction band
M	10^6 ohms
mbe	Molecular beam epitaxial
meV	10^{-3} electron volts
MD	Medium aperture
MIR	Three letter computer command to change mirror position
MOCVD	Metalorganic chemical vapor deposition
n_i	Displacement of point i from the start of scan
N_A	Number of acceptors
N_D	Number of donors
NDP	Number of data points
NSS	Number of scans to be taken and put into sample file
NTP	Number of transform points
OFHC	Oxygen free high conductivity
Pb	Lead
PCx	Three letter computer command to phase calculate the given data file (x=B(Background file), D(Destination file),R(Reference file),S(Sample file))
R_H	Hall constant

r_H	Hall coefficient factor
R_L	Top of the load resistor wire
R_S	Top of the sample wire
R_y*	Effective Rydberg for hydrogenic donors
RL	Load resistor resistance
RS	Sample resistance
Res	Resolution
RF	Radio frequency
Se	Selenium
Si	Silicon
SM	Small aperture
S/N	Signal to noise ratio
Sn	Tin
SRC	Three letter computer command for control of the light sources
SSP	Three letter computer command for control of the sample spacing
TGS	Pyroelectric detector
TI	Triangle apodization function
TP	Trapezoidal apodization
V_b	DC bias voltage
V_s	Sample voltage
VEL	Three letter computer command to control the velocity of the moveable mirror
vpe	Vapor phase epitaxial
z_o	Location of zero path difference

Roman Letter Symbols

B	Magnetic field
c	Speed of light
D	Diameter
e	Charge of the electron
f	Frequency
H	Magnetic field
I	Current
l	Thickness of Mylar
m	Mass of the electron
n	Carrier concentration
R	Reflection coefficient or Resistance
t	Time
T	Transmission coefficient
V	Voltage
v	Velocity
x,y,z	Dimensions of crystal used in Hall measurements

Greek Letter Symbols

β	Number used by the computer to determine the size of the iris aperture
δ	Path difference
Ω	Ohms
ε_o	Static dlelectric constant for the semiconductor
$\mathcal{F}$	Fourier transform
λ	Wavelength

μ	Mobility
μa	10^{-6} amps
μm	10^{-6} meters
ω	Angular frequency
ω_c	Cyclotron frequency
ρ	Resistivity
σ	Conductivity
σ_1	Wavenumber

Abstract

The donor impurities in high purity n-GaAs can be described using a hydrogenic model. In a magnetic field the hydrogenic donor levels will split and the chemical shifts of the 1s-2p Zeeman transitions between donor states can be used to identify the impurities. The 1s-2p (m=±1) transitions are the strongest and best to use to identify the impurities.

A rapid-scan Fourier transform spectrometer is used in conjunction with gold coated lightguide optics and a 125kG superconducting magnet to obtain photoconductivity spectra. The experimental arrangement and procedure are described in detail. This is the first known use of a rapid-scan Fourier transform spectrometer for this type of experiment.

The necessary experimental data that had to be obtained on equipment, filters, temperature and electrical properties of GaAs to include carbon resistor resistances at cryogenic temperatures, spectral response of low pass optical filters, current-voltage characteristics of GaAs, Hall measurements, GaAs resistance versus temperature, and the best computer spectrum collection parameters for a Nicolet 8000 Fourier Transform Spectrometer are discussed. Zero field spectra from a sample with a carrier concentration of $1.25 \times 10^{14} cm^{-3}$ and liquid nitrogen

mobility of $1.5 \times 10^5 \, cm^2$/V-sec are presented and discussed
along with the problems in setting up the experiment and
obtaining spectra in a magnetic field.

150000 sq. cm

FAR-INFRARED PHOTOCONDUCTIVITY OF HIGH PURITY

n-GaAs IN A MAGNETIC FIELD USING

RAPID-SCAN FOURIER TRANSFORM

SPECTROSCOPY

I.   Introduction

Background

Gallium Arsenide (GaAs) has important uses as a laser, semiconductor, and infrared detector (20). It is important to identify impurities in GaAs since they determine its electrical properties. It is difficult to identify concentrations of impurities in GaAs below 10^{16} atoms per cubic centimeter using chemical or mass spectroscopic techniques. Far-infrared photoconductivity in a magnetic field is a useful method to identify low concentrations of impurities (1).

The impurity atoms in GaAs have an extra electron and positive charge in their nucleus relative to the atoms they replace. The n-type impurities in GaAs produce shallow donor levels since their extra electron is not used in the covalent bonding of the crystal and has a small binding energy. The binding energy is approximated using the Bohr model of the hydrogen atom with a dielectric constant and electron effective mass used in the Bohr formula to account

1

for the electronic polarization of the medium and the
periodic potential of the crystal (see Eqs (20) and (21)).
Besides the ground state, there are a number of excited
levels for the donors similar to those in hydrogen (Figure 1;
Eqs (22) and (23)).

> There are, however, small corrections to this
> formula [Bohr], known as central cell effects, arising
> from the deviation of the potential from the simple
> Coulombic relation close to the impurity site. These
> corrections are most significant for the ground state
> because of the appreciable amplitude of the 1s wave-
> function close to the origin (14).

Differences in transition energies between different
energy levels (1s-2p, 1s-3p, etc.), due to the different
donors, are impossible to see in a zero field spectrum.
Applying a magnetic field to the sample causes Zeeman split-
ting of the 2p, 3p, etc., levels (Figure 17). More impor-
tantly, the donor electron's wavefunction is compressed and
distorted by the magnetic field. Thus, the shift in the 1s
energy (central cell correction), which is different for
the different donors, becomes more pronounced. Also, the
spectral transition lines narrow with increasing magnetic
field. Therefore, for example, the 1s-2p (m=-1) transition
energy is different for the various impurities in the GaAs
sample and can now be identified using photoconductivity
in a magnetic field.

By illuminating a sample of GaAs with modulated
light from a Fourier transform spectrometer, the donor
electrons, for the different impurities, are excited from the
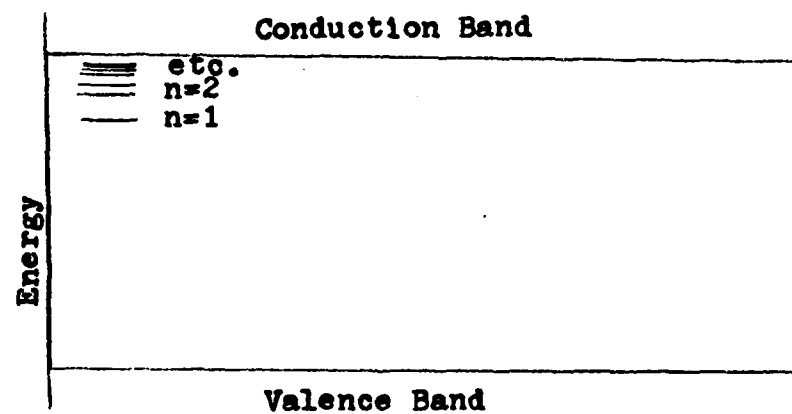
Fig.1 . Donor impurity levels

1s to 2p level. The electrons now in the 2p level are excited further, by thermal excitation, into the conduction band where they produce a change in conductivity which is detected. A photoconductive spectrum, due to the various hydrogen-like transitions, is obtained by plotting photo-conductive response versus wavenumber at a constant magnetic field (Figure 2). The peaks that are strongest and best to use in identifying impurities are the 1s-2p (m=±1) (1; 2; 38). In theory, far-infrared photoconductivity in a magnetic field can determine the various chemical impurities in GaAs (33).

Problem

The primary objective of this project was to design, fabricate and set up the necessary equipment to observe photoconductivity of GaAs in zero field and in magnetic fields up to 125kG using rapid-scan Fourier transform spectroscopy. Prior to that, the necessary experimental data had to be obtained on equipment, filters, temperature and electrical properties of GaAs.

Scope

This report deals with the theory of hydrogenic donors in GaAs, electrical characteristics of GaAs, zero field photoconductivity, photoconductivity in a magnetic field and Fourier transform spectroscopy. Emphasis is placed on the equipment and procedures used to obtain a
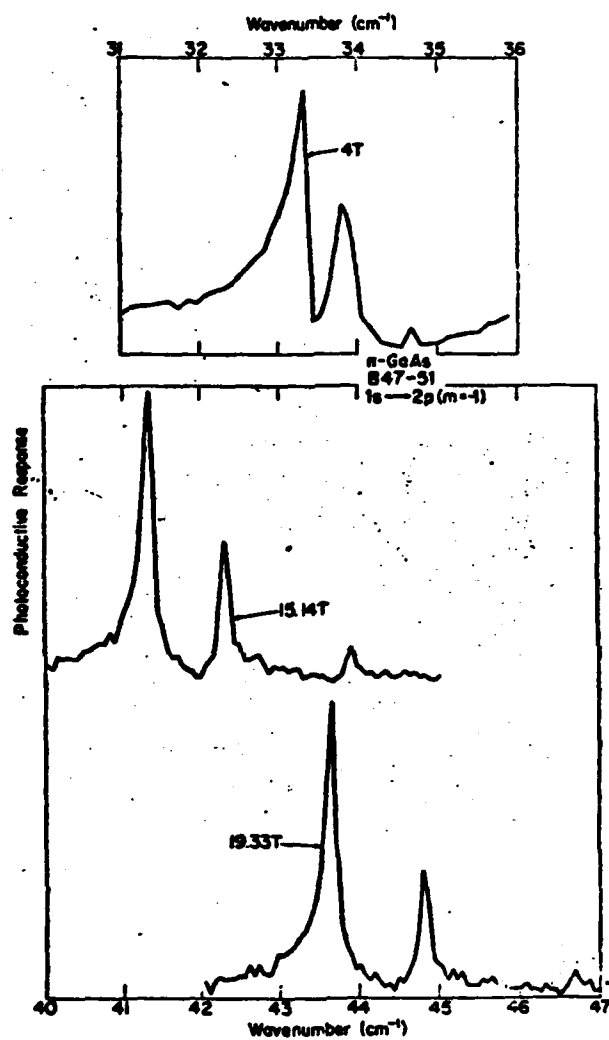
Fig. 2. 1s-2p (m=-1) transition of a n=.9 E 14
sample at three magnetic fields. The large peak
is due to silicon and small one due to germanium.
(2)

5

photoconductive spectrum. The GaAs samples were cooled to 4.2^OK and magnetic fields up to 125kG were available. The wavenumber region of interest is $0-120cm^{-1}$.

The experimental results will include:

1. The resistance of carbon resistors at 296^OK, 77^OK, 4.2^OK.

2. The spectral response of the various filters available for the two superconducting magnet systems used.

3. The current-voltage characteristics of GaAs at 4.2^OK.

4. A GaAs sample's resistance versus temperature.

5. Hall measurements for five samples.

6. The best computer spectrum collection parameters for the Nicolet 8000 Fourier Transform Spectrometer in the region $1-120cm^{-1}$ with a resolution of $.05cm^{-1}$.

7. Two zero field photoconductivity spectra and the reasons why nonzero magnetic field data was not obtained.

Assumptions

The photoconductivity measurements of GaAs in a magnetic field rely on the hydrogen-like properties of impurity electrons in GaAs. Application of a magnetic field causes Zeeman splitting of these lines and each impurity can be identified by its 1s-2p (m=±1) transition. At a given magnetic field, the 1s-2p (m=±1) transition energy differs for each element since they all have different central cell corrections for the 1s state.

Sequence of Presentation

A brief review is presented in Chapter II of the current literature concerning photoconductivity in a magnetic field. Chapter III contains the theory of the hydrogenic model, Fourier transform spectroscopy, photoconductivity and photoconductivity in a magnetic field. A detailed description of all the equipment used is in Chapter IV. The experimental procedure for obtaining a photoconductive spectrum in a magnetic field along with other experimental procedures are reviewed in Chapter V. The results of a number of experiments done to set up the photoconductivity experiment properly and the zero field photoconductivity spectra are in Chapter VI. Also in that chapter are the reasons why nonzero magnetic field spectra were not obtained. Chapter VII has suggestions and recommendations.

II. Literature Review

This is a review of current literature concerning the identification of residual donors in high purity epitaxial Gallium Arsenide (GaAs) by the use of far-infrared photoconductivity in a magnetic field. The review covers a number of recent scientific journal articles about photo-conductivity in GaAs. The discussion covers several groups who contribute most to photoconductivity research.

Articles by Stillman and Others

Stillman and his coworkers did some of the first work on identifying donors in GaAs using a magnetic field.

In his 1971 paper he outlines the process used for magnetospectroscopy and identifies various hydrogen-like transitions in GaAs. He shows that the hydrogenic model was useful in explaining these transitions and that the 1s-2p (m=±l) lines dominate at higher magnetic fields (38).

His chapter in Willardson and Beer provides excellent background material on the experimental and theoretical concepts of photoconductivity and photoconductivity in a magnetic field (37).

In 1977, he identified a number of donors such as lead (Pb), selenium (Se), tin (Sn), silicon (Si), sulfur (S), and germanium (Ge) (48). A number of these identifications, however, are now believed to be incorrect.

Stillman recently has used molecular beam epitaxial samples in his research. He views the 1s-2p (m=-1) transition at various magnetic fields to determine the donors in GaAs. A vapor phase epitaxial (vpe) sample is used as a reference since its transition lines are very sharp (Figure 20). Molecular beam epitaxial (mbe) samples are, at present not as pure as vpe GaAs; therefore, their lineshapes are broad. Thus, it is difficult to identify donors in mbe material. Molecular beam epitaxial grown GaAs does offer, when perfected, the possibility of more controlled doping of impurities in samples. Then it would be easier to identify a donor with its transition line location (24).

Stillman identifies lead, silicon, selenium, and sulfur in his mbe samples. He admits his silicon line identification is in disagreement with other researchers. All of the mbe samples tested, grown at different laboratories, had the same four impurities in them: Si, Pb, Sn, S (24).

In his recent work, he corrects his identification of sulfur (25) and silicon (26). Using photoconductivity data for undoped and S-doped samples grown by metalorganic chemical vapor deposition (MOCVD), he says the spectral peak X_2 (25) is due to S donors. Silicon is confirmed to be the X_1 spectral peak (26) by a reexamination of the data from mbe GaAs samples.

Articles by Button and Afsar

Afsar and Button are doing research with GaAs for
the Air Force. What follows is a summary of three of their
papers (1; 2; 3). Their samples for the first two papers
came from the Air Force Avionics Laboratory (1; 2) and the
third from Bell Laboratories (3).

Afsar and Button look at impurity spectra as other
researchers do by plotting photoconductive response versus
wavenumber (Figure 2). They obtain a number of peaks due
to the various hydrogen-like transitions. The peak that is
the strongest and best to use in identifying impurities is
the 1s-2p (m=-1) (1; 2).

What they claim they do differently from others is
plot a "signature curve for each contaminant by measuring
the energy of its 1s-2p (m=-1) transition at several values
of magnetic field intensity" (1) (Figure 3). They claim
identifying elements is easier using the signature curves
since the points for a given element will fall on a single
line. It is necessary when three or more contaminants are
present (1; 2).

In their experiments, they use a screw driven Fourier
transform spectrometer, low temperatures (4°K-10°K), and
high magnetic fields (15 Tesla) to split and analyze the
spectral lines (1; 2).

They have confirmed the identification of sulfur,
silicon, and carbon. Germanium and selenium were identified
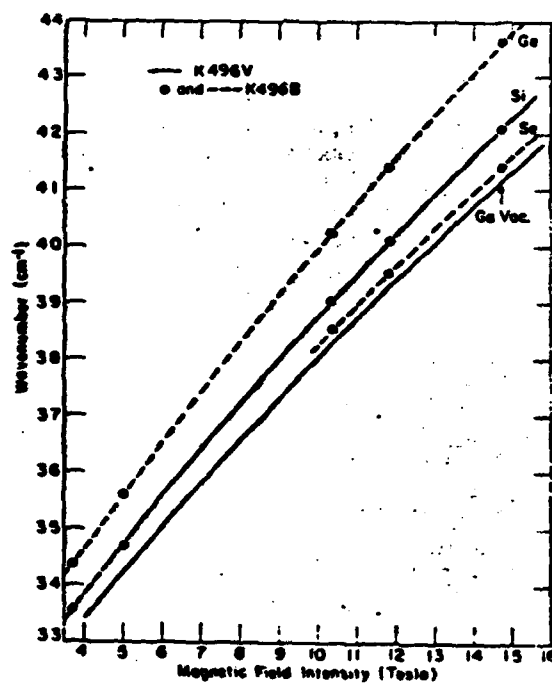
Fig. 3 . Characteristic curves for Se and Ge
at high fields. (1)

in samples where carbon and silicon were reported previously. The carbon that Stillman reported is believed by Afsar to be germanium. Their signature curves have one line which is unidentifiable, a twin silicon, and a twin unidentifiable line. They also could not identify tellurium, oxygen or lead (1; 2).

In the third paper, they claim the ultimate method for identifying donors in epitaxial GaAs (3). It is the same method described above except they use mbe GaAs which is doped with only one impurity. Since they know the impurity doped, they obtain a unique signature curve for that element. They applied this method to tin and plan to do the same for other impurities (3). Their spectrum has a great deal of noise and they failed to identify other impurity peaks.

Article by Ozeki and Others (32)

Ozeki and his associates are doing photoconductivity work in Japan. In their work, they use a screw driven Fourier transform spectrometer and vpe GaAs samples to study the donor's silicon, selenium, sulfur and germanium. Their conclusions are the following:

    1. For the epitaxial layers grown by nitrogen system, the major residual donor impurities are sulfur and germanium, and sulfur is always present.

    2. For the epitaxial layers grown by hydrogen system, the major residual donor impurities are silicon, sulfur and germanium, and the dominant one is sulfur or silicon.

3. Carbon is incorporated into epitaxial layers as an acceptor, but cannot be incorporated as a shallow donor.

4. Silicon, selenium, sulfur, and germanium are readily incorporated into epitaxial layers as a donor and have the ionization energies of 5.795meV, 5.812meV, 5.845meV, and 5.949meV, respectively. (32)

Articles by Stradling and Others

Stradling and his associates conduct their research in Great Britain. Their experimental method is different from the Fourier transform method described previously. They use the technique of Far Infrared Laser Spectroscopy (6). In this method, instead of keeping the magnetic field fixed and varying the wavelength of the light on the sample, a fixed wavelength laser is used and the magnetic field is swept. This method has the advantage of greater resolution and higher signal to noise but has the disadvantage of having to sweep the magnetic field whose values cannot be measured to high precision. A 118.8 micron laser is used for the 1s-2p (m=+1) transition and a 302.8 micron laser for the 1s-2p (m=-1) transition. They discuss peaks in their spectrum attributed to X_1, X_2, X_3, lead and tin. They question whether X_2 is sulfur.

In an earlier work (14), Stradling and several different coworkers used Fourier transform spectroscopy in identifying donors in GaAs.

Article by Dingle and Others (18)

They also work in Great Britain and use the laser method described above. Carbon and silicon are reported in their mbe GaAs samples, but there were two peaks they could not identify.

Conclusion

Far-infrared photoconductivity of GaAs in a high magnetic field can identify low concentrations of impurities without harming the crystal. There are, however, some disagreements as to which elements correspond to which spectral lines and lines that could not be identified. There is some misinformation in earlier works that is slowly being corrected today. It appears that there is good agreement today for the tin, $X_1(Si)$, $X_2(S)$, $X_3(Ge)$ lines and that carbon will incorporate preferentially as an acceptor.

III. <u>Theory</u>

Five areas will be covered in this section covering the major topics of interest in this project. The first area will be the theory of Fourier transform spectroscopy. Next, the hydrogenic model for the impurities in GaAs is discussed. Hall measurements and the electrical character- istics of GaAs are important in understanding the photocon- ductivity of samples. Finally, the theory of the main thrust of the project, photoconductivity in a magnetic field, is discussed.

<u>Fourier Transform Spectroscopy</u> (7; 29)

For infrared spectroscopy, we need to obtain a plot of the irradiance versus frequency. All known far-infrared detectors are broad-band, which gives an irradiance reading averaged over all frequencies. Fourier transform spectros- copy overcomes this handicap by preserving both frequency and irradiance information. This is done by modulating the infrared signal into audio frequencies, where detectors are available to track both frequency and irradiance information. This is done, e.g., by using a Michelson interferometer (Figure 4).

Radiation is emitted from a source and collimated by mirrors. The collimated beam hits a beamsplitter (50% reflected, 50% transmitted ideally) and the two beams are

reflected off a movable mirror and fixed mirror. One beam goes back to the light source and the other goes to the sample and detector.

If our source were monochromatic, the output from the interferometer (interferogram), as the mirror moves, would be a cosine wave corresponding to the constructive and destructive interference points. The delta functions and cosine wave are a Fourier transform pair.

$$\mathcal{L}[g(t)] = G(f) = \int_{-\infty}^{\infty} g(t)e^{-i2\pi ft}dt \qquad (1)$$

$$g(t) = \cos(t) = \frac{e^{it} + e^{-it}}{2} \qquad (2)$$

$$\mathcal{L}(g(t)) = \int_{-\infty}^{\infty} \frac{e^{it} + e^{-it}}{2} e^{-i2\pi ft}dt \qquad (3)$$

$$= \int_{-\infty}^{\infty} \frac{e^{it-2\pi ift} + e^{it-2\pi ift}}{2} dt \qquad (4)$$

$$= \tfrac{1}{2} \int_{-\infty}^{\infty} e^{i2\pi t(\frac{1}{2\pi} - f)} + e^{i2\pi t(-\frac{1}{2\pi} - f)}dt \qquad (5)$$

$$= \tfrac{1}{2}\{\delta(f-\tfrac{1}{2\pi}) + \delta(f+\tfrac{1}{2\pi})\} \qquad (6)$$

As more frequencies are added, a beat pattern develops. When a large amount of frequencies are added in, the interferogram appears as in Figure 5. The large center peak is where the light paths to the fixed mirror and movable mirror are equal. As you move further from the central peak, the signal drops off due to destructive

16
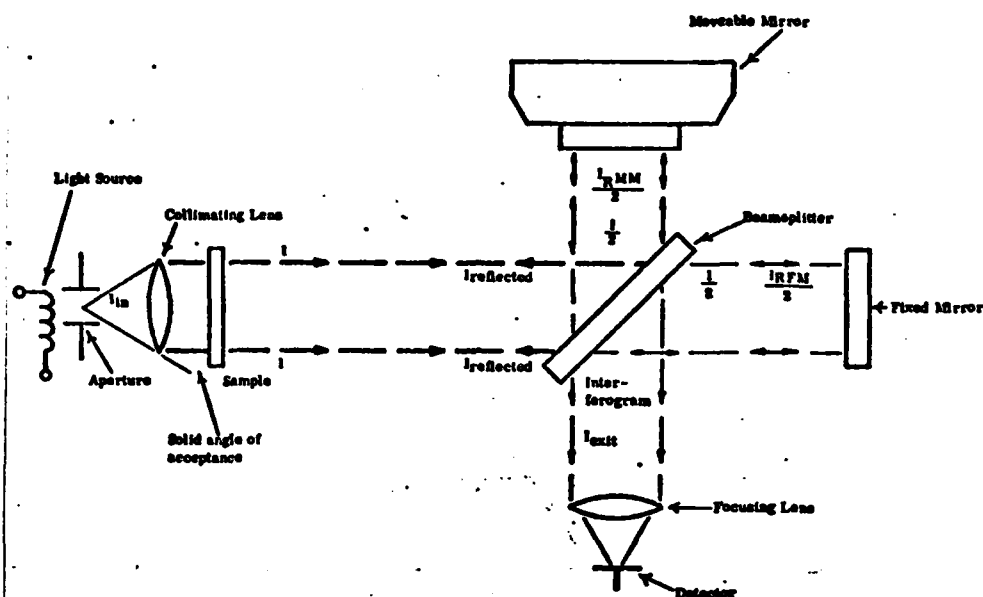
Fig. 4 . Michelson interferometer. (29)
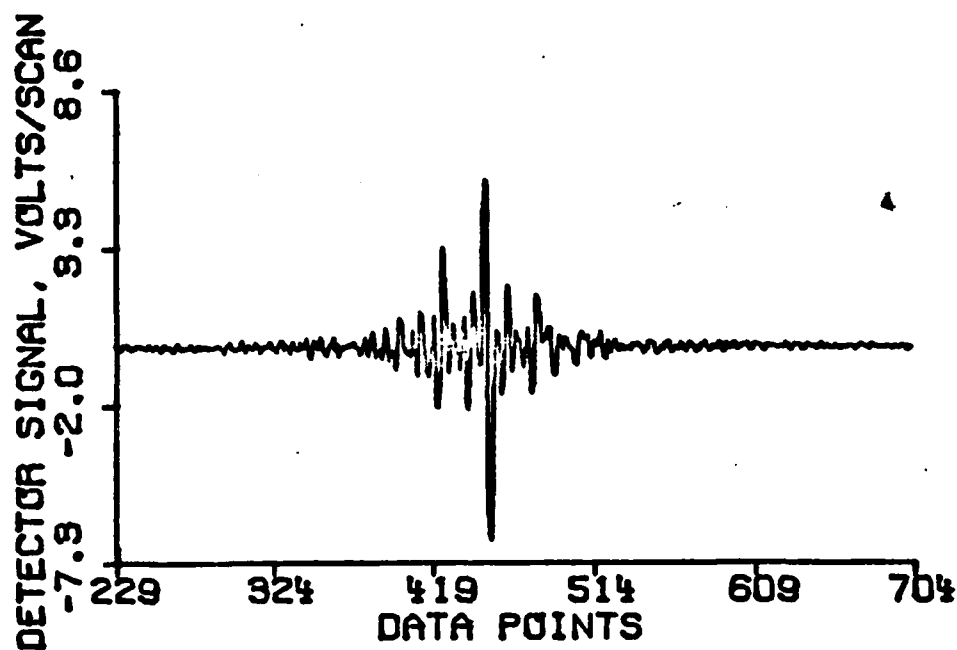
Fig. 5 . Interferogram from Nicolet 8000 Fourier
Transform Spectrometer.

17

interference of the various frequencies. By taking the Fourier transform of the interferogram versus mirror position, the frequency spectrum results.

The mathematics of Fourier transform spectroscopy are as follows (7).

Let the incident radiation on the beamsplitter be represented by

$$\epsilon(z,\sigma_1)d\sigma_1 = \epsilon_o(\sigma_1)e^{i(\omega t - 2\pi z \sigma_1)}d\sigma_1 \qquad (7)$$

where

$$\sigma_1 = \frac{1}{\lambda} \qquad (8)$$

Before the beams recombine, they will have travelled distance z_1 and z_2 and undergone one reflection and transmission through the beamsplitter. The resulting amplitude is

$$\epsilon_R(z_1,z_2,\sigma_1)d\sigma_1 = RT\epsilon_o(\sigma_1)[e^{i(\omega t - 2\pi\sigma_1 z_1)}$$
$$+ e^{i(\omega t - 2\pi\sigma_1 z_2)}]d\sigma_1 \qquad (9)$$

The irradiance for a given spectral range $d\sigma$ is

$$I(z_1,z_2,\sigma_1) = \epsilon_R(z_1,z_2,\sigma_1)\epsilon_R^*(z_1,z_2,\sigma_1)$$
$$= 2\epsilon_o^2(\sigma_1)|RT|^2\{1 + \cos[2\pi(z_1-z_2)\sigma_1]\}d\sigma_\perp \qquad (10)$$

18

The resulting irradiance for any given path difference $\delta = (z_1 - z_2)$ is

$$I_R(\delta) = \int_0^\infty I(\delta, \sigma_1) d\sigma_1 \qquad (11)$$

$$= 2|RT|^2 [\int_0^\infty \epsilon_0^2(\sigma_1) d\sigma_1 + \int_0^\infty \epsilon_0^2(\sigma_1) \cos(2\pi\sigma_1 \delta) d\sigma_1] \qquad (12)$$

When $\delta = 0$, we have

$$I_R(o) = 2|RT|^2 [\int_0^\infty \epsilon_0^2(\sigma_1) d\sigma_1 + \int_0^\infty \epsilon_0^2(\sigma_1) d\sigma_1] \qquad (13)$$

$$= 4|RT|^2 \int_0^\infty \epsilon_0^2 d\sigma_1 \qquad (14)$$

therefore,

$$I_R(o) - \tfrac{1}{2} I_R(o) = 2|RT|^2 \int_0^\infty \epsilon_0^2(\sigma_1) \cos(2\pi\delta\sigma_1) d\sigma_1 \qquad (15)$$

which is an oscillation of the signal $I_R(\delta)$ about the value $\tfrac{1}{2} I_R(o)$ and is called the interferogram. By taking the Fourier cosine transform, the spectrum is:

$$B(\sigma) \propto \epsilon_0^2(\sigma_1) = (\frac{1}{\pi |RT|^2}) \int_0^\infty [I_R(\delta) - \tfrac{1}{2} I_R(o)]$$

$$\cos(2\pi\sigma\delta) d\delta \qquad (16)$$

when evaluated at the wavenumbers of interest.

Most of the Fourier transform spectrometers have the movable mirror connected to a screw drive. The movable mirror is left at one position while the light from the

19

source is mechanically chopped. Signal averaging is done at this fixed path length for a given interval of time. Then the mirror is moved a small distance and the procedure is repeated. The procedure is continued for a given path distance L of the movable mirror to obtain the interferogram.

The rapid-scan Fourier transform spectrometer moves the movable mirror at a fixed velocity and can provide a single scan spectrum in less than a second. The principle behind the rapid-scan system is as follows.

The optical path difference is $\delta=2vt$ when the mirror moves at a constant velocity. Using Eq (12), the signal versus time is

$$I_R(t) = 2|RT|^2 [\int_o^\infty \varepsilon_o^2(\sigma_1)d\sigma_1 + \int^\infty \varepsilon_o^2(\sigma_1)\cos(\omega t)d\sigma_1] \qquad (17)$$

and the interferogram as a function of time is

$$F(t) = I_R(t) - \tfrac{1}{2}I_R(o) = 2|RT|^2 \int_o^\infty \varepsilon_o^2(\sigma_1)\cos(\omega t)d\sigma_1 \qquad (18)$$

where $\omega=2\pi\sigma\upsilon$ and the spectrum comes by taking a Fourier transform.

All the necessary spectral information is contained in the interferogram but the Fourier transform process converts it to usable form. A minicomputer controls the spectrometer and does all the Fourier processing using three letter commands (see p. 80).

The modulation frequency for the detector is determined by the velocity of the movable mirror and to some extent by the frequency of the source radiation. The velocity of the mirror is changed by varying the VEL (velocity) parameter (see p. 130) with the computer. The range of velocities are in Table I. The velocity of the mirror should be varied to determine the optimum audio modulation frequency of the detector.

Sampling (29;30). A HeNe laser is used to give an accurate distance scale for the interferogram. An interferogram from a HeNe laser (sine wave) is used to determine when the computer should take a data point. Sampling takes place as the HeNe interferogram goes through zero points. These points are equally spaced because a zero occurs at every half wavelength of the HeNe laser or .316496μm due to destructive interference from the different path lengths in the interferometer. Taking a data point at every zero crossing would correspond to a bandwidth of $15798.00cm^{-1}$ (Bandwidth = $1/(2 \times .316496 \times 10^{-4})$), according to the Nyquist or Sampling theorem which states that the maximum bandwidth is less than or equal to one divided by twice the path difference between data points. Since the smallest spacing between data points corresponds to a half wavelength of the HeNe laser, the maximum bandwidth is $15798.00cm^{-1}$ and by sampling at larger intervals (i.e., skipping zero crossings of the laser interferogram), the bandwidth decreases.

21

The sample spacing is controlled by the sample spacing parameter (SSP) (see p. 130). It determines how many zero crossings are skipped between sampling points. A SSP=1 means a data point is taken every zero crossing. The bandwidth is equal to 15798 divided by SSP. The allowed SSP values and their associated bandwidths are in Table II.

In order to use the interferogram for signal averaging, the scan must begin at the same point each time. A white light interferogram is used for this since it produces a large spike when the pathlengths to the moving and fixed mirror are identical, since the Fourier transform of a white light source is a delta function. The spike is optically offset so it comes before the central peak of the interferogram.

Resolution (29; 30). The sample spacing determines the bandwidth but the resolution is determined by the number of data points (or how far the mirror travels). This is seen in two different ways.

When viewing an interferogram different beat patterns are set up as the different frequencies interfere. As the frequencies you wish to resolve become closer together, their beat patterns occur farther out in the interferogram. Therefore, a larger number of data points must be taken to resolve these frequencies.

Another way to interpret resolution is through the Nyquist theorem. You need two data points in the frequency

22

Table I
Velocity of moveable mirror as function of VEL setting. (30)

VEL	cm/sec	VEL	cm/sec	VEL	cm/sec
00	0.055	20	0.220	40	0.880
01	0.058	21	0.234	41	0.938
02	0.063	22	0.250	42	1.003
03	0.068	23	0.272	43	1.084
04	0.074	24	0.294	44	1.174
05	0.080	25	0.321	45	1.279
06	0.088	26	0.352	46	1.408
07	0.097	27	0.391	47	1.564
10	0.110	30	0.440	50	1.760
11	0.118	31	0.479	51	1.878
12	0.127	32	0.503	52	2.010
13	0.135	33	0.541	53	2.167
14	0.146	34	0.586	54	2.346
15	0.160	35	0.648	55	2.560
16	0.176	36	0.704	56	2.816
17	0.196	37	0.783	57	3.130

Table II
Bandwidth as a function of SSP setting. (30)

SSP	Sample Spacing Setting	Bandwidth (cm^{-1})
1	1	15798.00
2	2	7899.00
4	3	3949.50
8	4	1974.75
16	5	987.38
32	6	493.69
64	7	246.84

domain for one resolution element. For instance, if your bandwidth was $7899cm^{-1}$, 4096 data points were available after the transform, and the sample spacing (SSP) was one, there would be a data point every $7899/4096 \cong 2cm^{-1}$. Twice $2cm^{-1}$ gives a resolution of $4cm^{-1}$. The resolution formula is Res=(2 x bandwidth)/number of data points.

To obtain 4096 data points after the transform, it is necessary to have NTP (number of transform points)= 2 x NDP (number of data points)=8192 transform points. The computer will take 8192 transform points, (4096 real data points, 4096 imaginary points), phase correct and give 4096 spectral points.

It should be noted that in order to obtain higher resolution, more data points need to be taken. If the mirror has gone full travel and the number of data points taken is still less than the number requested the mirror will go to its starting point and continue to take data points. Therefore, you could get data points from a second interferogram mixed into the first interferogram. The aperture also has an effect on resolution (Figure 25) since "as the source subtends a larger solid angle, peaks will be broadened and shifted slightly in frequency" (29).

Apodization (29; 30). An interferogram theoretically should extend from $-\infty$ to $+\infty$. The spectrum is obtained by taking the Fourier transform of the interferogram where the limits on the Fourier integral are from $-\infty$ to $+\infty$. The

24

mirror travel on the spectrometer is, however, finite. This has the effect of reducing the limits on the Fourier integral to correspond to the finite limits of the interferogram caused by the limited mirror travel. Another way of stating this is that the true interferogram is multiplied by a rect (x) function before the Fourier transform is performed. This causes the Fourier transform of the true interferogram to be convoluted with the Fourier transform of a rect (x) function (sinc(f)=sin(f)/f)). Lines narrower than the instrument resolution will take on the appearance of the sinc (f) function. One way to minimize this effect is to multiply the interferogram by a function other than a rect (x) function before transforming the interferogram. This technique is called apodization (AFN) (see p. 130) and it reduces these effects while also lowering the effective instrument resolution.

The functions available on the Nicolet 8000 are triangle (TI), boxcar (BX), trapezoidal (TP), cosine (CS), and Happ-Genzel (HG).

The HG function is recommended by Nicolet. Each data point is multiplied by

$$0.54 + 0.46\cos\frac{\pi}{2}\frac{|n_i - z_o|}{NDP - z_o} \tag{19}$$

where

n_i = displacement of point i from the start of scan.

z_o = location of the zero path difference.

NDP = number of data points.

before performing the Fourier transform. This will attenuate the sidebands with the smallest loss in resolution.

Phase Correction (29; 30). The interferogram must also be phase corrected to account for two effects. First, the refractive index of the beamsplitter is a function of frequency which distorts the spectrum. Also, a second phase error is introduced since the point of zero path difference does not correspond to the first point in the spectrum. A computer program corrects the phase errors using the three digit computer code PCx (x=B(Background file),D(Destination file),R(Reference file),S(Sample file)) (see p. 130) or it is automatically done when Fourier transforming an inter-ferogram using the FPx computer command (see p. 130).

Signal-to-Noise Ratio (29; 30). There are a number of factors affecting the signal-to-noise ratio (S/N).

The signal to noise improves as the square root of the number of scans. This is a statistical result which results from the noise adding in a random manner and the signal adding coherently.

The S/N is also proportional to the square root of the resolution. A higher resolution spectrum will also take longer to collect and Fourier process.

26

The S/N can be improved by electronic filtering of frequencies using high pass and low pass filter settings controlled by the computer codes HPS and LPS (see p. 129). It is also improved by optically filtering the incident light from the spectrometer onto the sample.

The S/N can also be improved by varying the velocity of the movable mirror. A detector has a different detectivity D* for different audio frequencies. Changing the velocity of the mirror changes the modulation frequency and thus the S/N through the detector's detectivity.

Hydrogenic Model (37; 13)

The shallow donors in high purity GaAs extend the long wavelength cutoff for extrinsic photoconductivity. A hydrogenic model can be used to estimate the donor binding energy.

Gallium Arsenide is a column III-V compound. When a column IV impurity atom is substituted at a Ga site, the impurity will have an extra electron not involved in bounding the crystal. Since it is not shared by the neighboring atoms, the electron will free itself from the core, leaving the core with a net positive charge of one. The same effect is true when a column VI impurity is substituted at an As site. Common column IV impurities in GaAs are carbon, silicon, germanium, tin and lead. Common column VI impurities are sulfur, selenium and tellurium.

Since an extra electron and nuclear charge is analogous to a hydrogen atom, the Bohr model is used to predict energy levels for the electron. The binding energy of the hydrogenic impurity will be smaller than that for a hydrogen atom for two reasons. First, the Coulomb interaction is reduced by the electronic polarization of the medium which is taken into account by a dielectric constant which is greater than one. Second, the model is modified with an effective mass of the electron used to account for the periodic potential of the crystal. The electron's effective mass is much smaller than the electron's mass in a vacuum.

The donor binding energy is approximately

$$E_D = m^*e^4/2\varepsilon_o^2h^2 = 13.6(m^*/m)/\varepsilon_o^2 \text{(ev)} \qquad (20)$$

and the Bohr radius for the electron is

$$a_B = 5.29 \times 10^{-9}\varepsilon_o/(m^*/m) \text{ (cm)} \qquad \text{4} \qquad (21)$$

where

      m^*/m = effective mass ratio for electrons

      ε_o = static dielectric constant for the semi-conductor

For GaAs, the calculated values are:

m^*/m	ε_o	E_D(meV)	a_B(A^o)	a_B/a_o	a_o(A^o)
.0665	12.5	5.77	99	17.6	5.65754

where

      a_o = lattice spacing of the semiconductor.

28

The calculated values show the large Bohr radius for the electron and the small value for the binding energy.

This model predicts that all impurities will have the same binding energy. This is true when $a_B > a_0$. The impurity electrons thus have a large Bohr radius and their binding energies are basically the same.

There are, however, small corrections to this formula, known as chemical shifts or central cell effects, arising from the deviation of the potential from the simple Coulombic relation close to the impurity site. These corrections are most significant for the ground state because of the appreciable amplitude of the 1s wave-function close to the origin (14).

Variations in the impurity potential close to the core (i.e., in the central cell) from one impurity species to another can thus produce shifts in the level of the 1s state (6).

It is this chemical shift that becomes more pronounced with magnetic field along with the narrowing of the spectral lines that allows identification of impurities in high purity GaAs using far-infrared photoconductivity in a magnetic field.

The hydrogenic model also predicts a number of excited states with energies

$$E_n = \frac{E_D}{n^2} = 13.56(\frac{m^*}{m})\frac{1}{\varepsilon_0^2 n^2} \text{ (ev)} \tag{22}$$

The Bohr radii of the excited states are

$$a_n = a_B n^2 = 5.29 \times 10^{-9}(m/m^*)\varepsilon_0 n^2 \text{ (cm)} \tag{23}$$

where n = integer.

29

Hall Measurements and Electrical
Properties of GaAs (37; 35; 36)

Hall analysis is used to determine the resistivity, ohmic character and carrier concentration of GaAs samples.

By fitting a carrier concentration equation to the experimental variation versus temperature, it is possible to determine the acceptor (N_A) and donor concentrations (N_D). The concentration of electrons in the conduction band is given by

$$\frac{n(n+N_A)}{(N_D-N_A-n)} = \frac{N_c}{g_1} \exp(-E_D/kT) \qquad (24)$$

where

$$N_c = 2(2\pi m_D^* kT/h^2)^{3/2}$$

m_D^* = conduction band density-of-states effective mass

g_1 = degeneracy of the ground state of the impurity center

$p \ll n$

The electron concentration is experimentally determined by

$$n = r_H/eR_H \qquad (26)$$

r_H is a function of magnetic field, temperature and degeneracy but, for either high magnetic fields or energy independent scattering mechanisms, $r_H \cong 1$.

Using the values $r_H=1$, $m_D^*=.072m$, $g_1=2$, the experimental and calculated values are given in Figure 6. The

calculated and experimental values only agree well for the
high purity samples at low temperatures.

The Hall analysis shows that high purity GaAs has
very shallow donor levels. The thermal ionization energy
of the highest purity sample is approximately 5.5meV and
decreases as the purity decreases. It is possible to ionize
the donor electrons into the conduction band by impact
ionization of energetic free carriers.

This effect is observed from the current-voltage
characteristics of a sample (Figure 7). The sample shows a
linear relation between voltage and current at low bias
voltages and currents. As the bias voltage is increased, the
sample resistance decreases and the I-V characteristics are
nonlinear. Figure 8 shows similar I-V curves for two samples
while also showing the effect a small magnetic field has on
the sample's electrical characteristics.

Photoconductivity (37)

One of the first photoconductivity spectra was made
by Bosomoworth (Figure 9). The peaks at $37cm^{-1}$ are due to
the absorption and photoconductivity of the shallow donors.
This long wavelength threshold makes GaAs useful as a
detector in the far-infrared region.

There is no fine structure in this spectrum
($n \approx 1 \times 10^{15} cm^{-3}$) due to the continuum caused by the overlap-
ping of the donor wave functions. For a higher purity
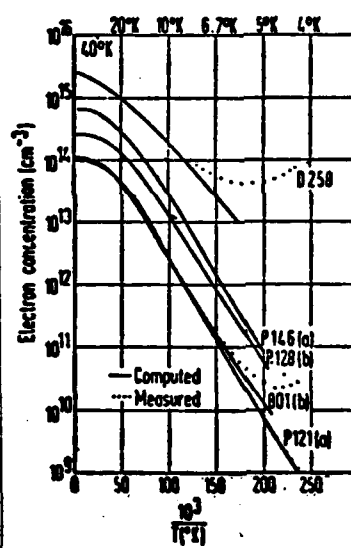
Fig. 6 . Electron concentration as a function of temperature for vpe GaAs. (37)
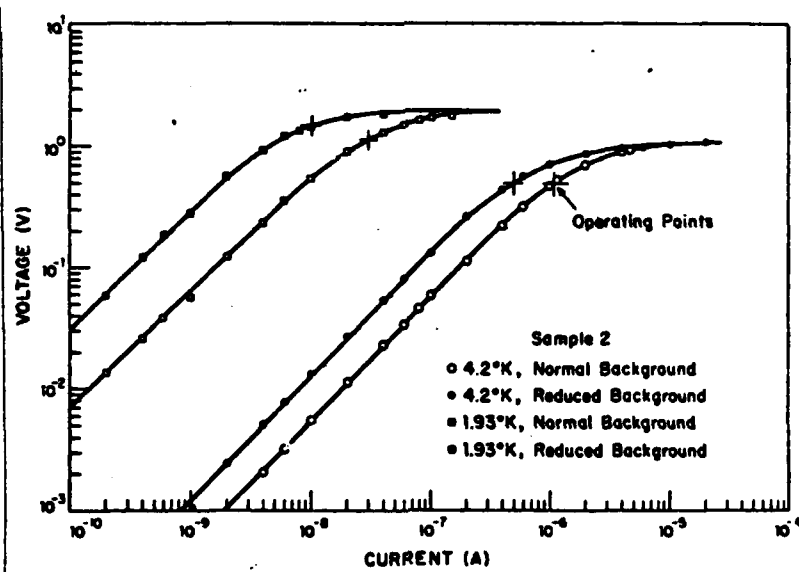
Fig.7. I-V characteristics for a n=1.6 E 14 sample. (36)
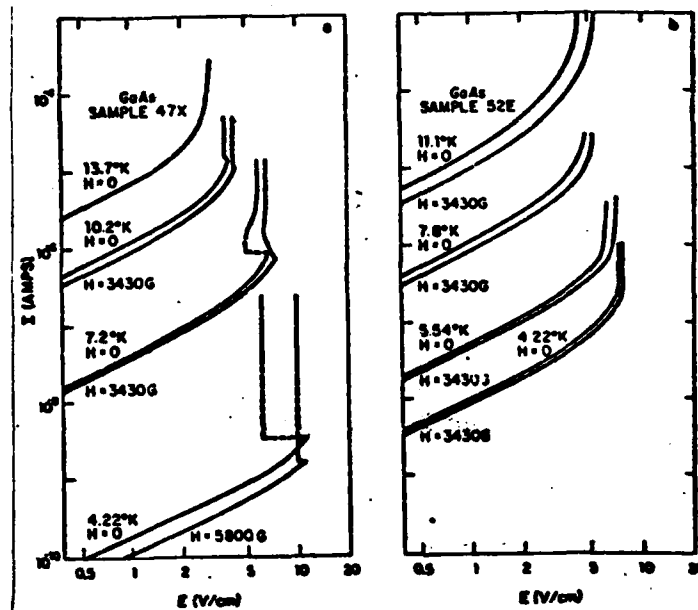
Fig. 8. Current versus electric field curves at several temperatures, with and without a transverse magnetic field. (37)
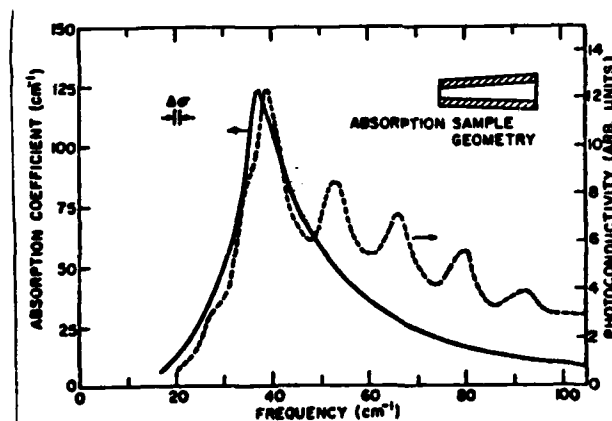
Fig. 9. The solid curve shows the absorption spectrum of a wedge shaped high-resistivity GaAs substrate and two epitaxial layers. The dashed curve shows the photo-conductivity spectrum of a 75 micron slice of epitaxial GaAs. (8)

33

sample ($n=5 \times 10^{13} \text{cm}^{-3}$, Figure 10), the dominant peak occurs approximately at 35.5cm^{-1} and some of the other levels are observed (1s-3p, etc.). The ionization energy is approximately 47.3cm^{-1}. The oscillator strengths for these transitions are the same as for the hydrogen atom

$$f_{1s-2p} = .4162$$

$$f_{1s-3p} = .0791$$

$$f_{1s-4p} = .0290$$

$$f_{1s-5p} = .0139$$

$$f_{1s-cont} = .436$$

Photoconductivity in GaAs results from the absorption of radiation and the subsequent ionization of an electron into the conduction band. Once there, the electron can contribute to the conductivity ($\sigma = ne\mu$). Assuming the mobility μ stays constant, a given wavelength of light will ionize a certain amount of donors Δn, thereby giving a change in conductivity $\Delta\sigma = \Delta ne\mu$. The conductivity is related to resistivity by $\sigma = 1/\rho$ and the sample resistance is

$$R = \frac{\rho x}{yz} \qquad (27)$$

where x,y,z are the crystal dimensions used in the Hall measurements. A change in resistance can be measured by a change in voltage when the sample is biased by a voltage

$$\Delta R = \frac{\Delta v}{I} \qquad (28)$$

34

The radiation, depending on its energy, can cause a donor electron to go from the 1s state to any of the other hydrogenic states or to the conduction band. There are two competing processes here. Once the electron is in one of its hydrogenic states, there must be a process to place them into the conduction band. There is also the recombination processes.

The three main mechanisms of recombination are:

1. Auger recombination--The electron gives up its energy to another electron.

2. Radiative recombination--The energy of recombination is emitted as a photon.

3. Phonon recombination--The recombination energy is released in the form of phonons. This is the dominant recombination process.

The possible mechanisms that propel the electrons from their bound states into the conduction band are according to Stillman (37):

    a) field-induced tunneling from the excited state into the conduction band.
    b) impact ionization of the electrons in the excited states by energetic free electrons.
    c) thermal ionization by the absorption of one or more phonons.
    d) photoionization by the absorption of a second photon.

The photoconductive response of GaAs has a strong dependence on temperature, impurity concentration, and electric field across the sample.

The variation of the photoconductive response versus temperature for a high purity sample is shown in Figure 11. Lowering the temperature below $4.2^{O}K$ reduces the photoconductive response. At the other end, the photoconductive response decreases slightly as the temperature is increased from $4.2^{O}K$ to $5.5^{O}K$ and decreases rapidly up to $6.5^{O}K$ where there is no usable response (36). The low temperature effect is due to the thermal ionization probability of the bound states lowering for the lower temperatures. The high temperature effect is caused by the increasing number of electrons thermally ionized into the conduction band masking the small amount of donors ionized by radiation (Figure 12).

The impurity concentration also has an effect on the photoconductive response. Figure 13 shows the zero field spectrum of four samples with different donor concentrations. For the $N_D=4.8 \times 10^{13}cm^{-3}$ sample, two peaks are observed at $35.5cm^{-1}$ (1s-2p) and $42.2cm^{-1}$ (1s-3p). As the donor concentration is increased, the spectrum broadens and the 1s-3p peak disappears. This effect is caused by the donor impurity wave functions overlapping as their concentration is increased. Using photoconductivity in GaAs to identify donors is only useful at impurity concentrations of $10^{15}cm^{-3}$ or less. Also, the line widths of the spectra narrow as the concentration is lowered.

The normal way to use GaAs as a detector or to measure its photoconductive response is to set up the
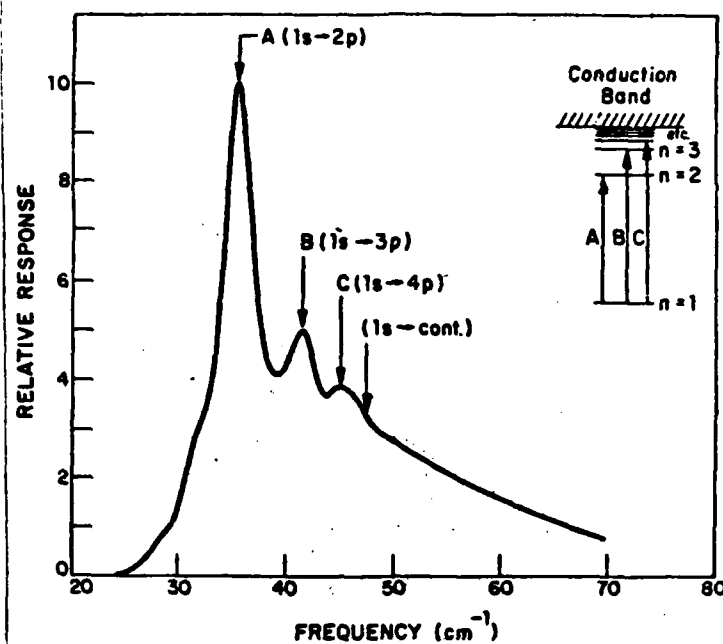
Fig. 10. Extrinsic photoconductivity spectrum for high
purity GaAs at 4.2°K. (36)
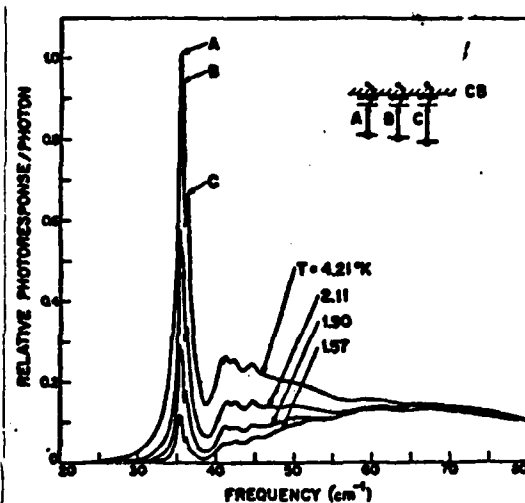
Fig. 11. Variation with temperature of the excited state
photoconductivity in high purity GaAs. (37)

37
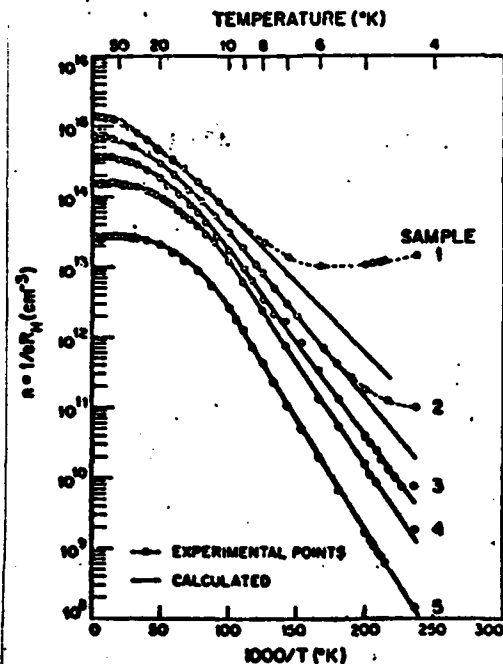
Fig.12. Experimental and calculated variation in the electron concentration with temperature for five GaAs samples. n= 1) 3.11E15, 2) 1.38E15, 3) 7.33E14, 4) 3.66E14, 5) 1.6E14. (35)
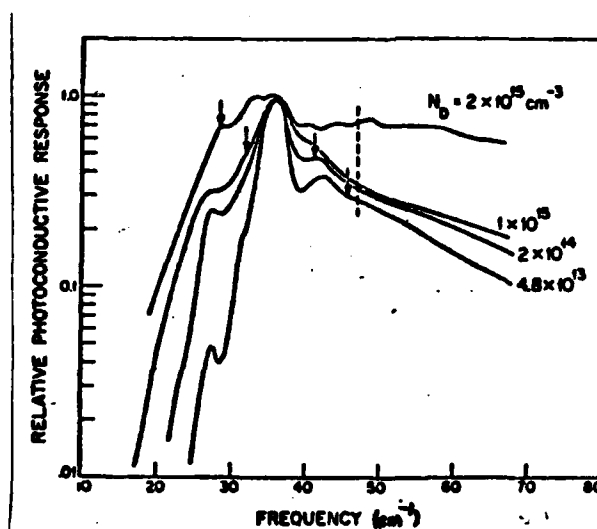
Fig.13. Spectra showing the change in photoconductivity with increasing donor concentration. The vertical arrows indicate the thermal ionization energies for the samples and the photoionization energy is indicated by the dashed line. (37)

following circuit
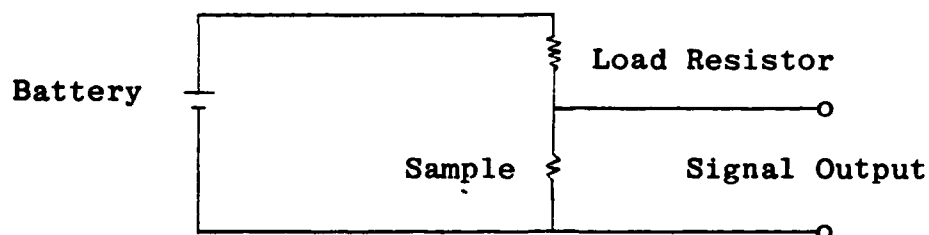
and measure the voltage changes of the sample. The signal
will depend on the bias current through the sample.
Figure 14 shows how the S/N varies with the bias current.
There is an optimum range for this sample of 10^{-6} to 10^{-7}
amps where the S/N is flat and at a maximum.

The resistance of the sample changes as its tempera-
ture changes since the carrier concentration changes as the
temperature is lowered (Figure 12) and the mobility changes
according to Figure 15. Using the formula

$$R = \frac{x\rho}{yz} = \frac{x}{yzne\mu} \tag{29}$$

and the mobility and carrier concentration graphs the
resistance of the sample will decrease from its room tempera-
ture resistance to a minimum at approximately $60^{\circ}K$ and then
become very high as $4.2^{\circ}K$ is approached.

Figure 7 shows the resistance at $1.93^{\circ}K$ higher than
at $4.2^{\circ}K$. It also shows how background radiation will change
the resistance by ionizing carriers.
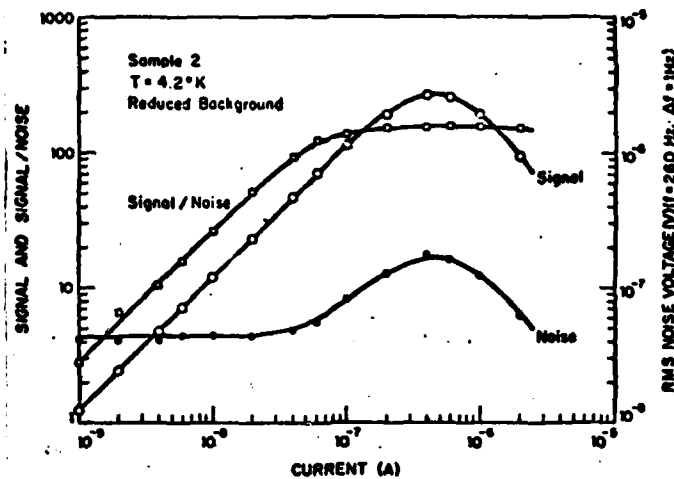
Fig.14. Signal, noise, and signal/noise dependence on bias
current for n=1.6E14 sample at 4.2°K with reduced background
conditions. (36)
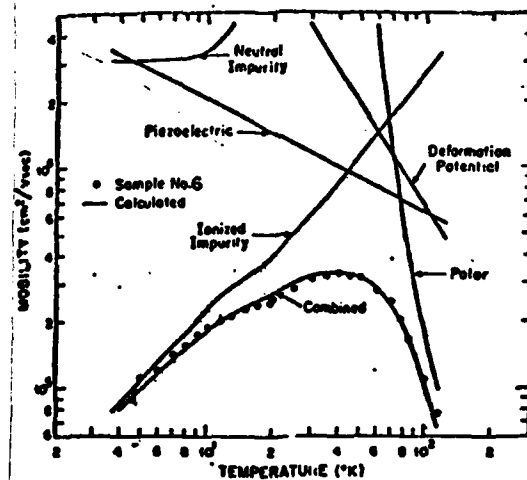
Fig.15. Experimental temperature variation of the mobility
of sample where n=2.7E13, and the calculated mobility
curves for each scattering process acting separately and for
all scattering processes combined. (35)

40

Photoconductive Response in A
Magnetic Field (37)

The zero field photoconductive spectrum and the hydrogenic model of donor impurity states in GaAs were already discussed. The hydrogenic model is further proved by the Zeeman splitting of the spectral lines under the influence of a magnetic field. The splitting of the lines will allow identification of the donor impurities present in a sample.

As a magnetic field is applied to the sample, the dominant 1s-2p peak in the zero field spectrum will split into three distinct peaks (1s-2p,m=0,±1) (Figure 16). The 1s-3p also splits into three peaks (1s-3p,m=0,±1) and a great deal of structure exists at higher wavenumbers due to higher order transitions.

At high magnetic fields, the 1s-2p m=±1 transition will dominate since they are the only transitions with finite oscillator strength at high fields (28).

The energy of the 1s-2p,1s-3p Zeeman transitions versus magnetic field are shown in Figure 17. The straight lines are theoretical calculations of Larsen and the experimental points are those of Stillman. The 1s-2p m=-1 decreases in energy while the other transitions increase in energy with magnetic field.
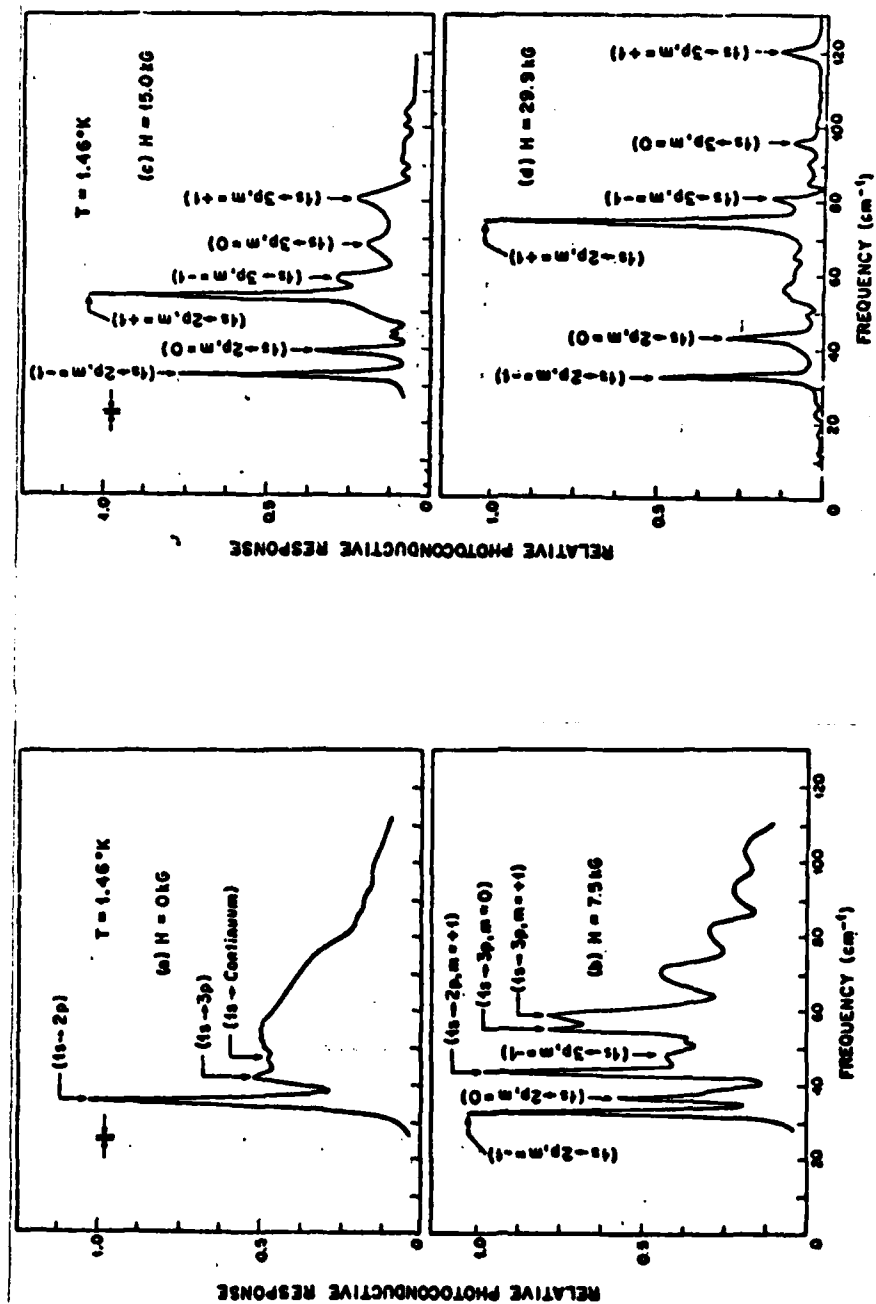
Fig. 16. Magnetic field dependence of the photoconductivity spectra of a n=2.67E13 sample at 1.46°K and a)H=0, b)H=7.5kG, c)H=15kG,d)H=29.9kG. (37)

42

The Zeeman splitting of the m=±1 states of a hydrogenic donor is given by

$$\Delta E_{+1,-1} = E(2p_+) - E(2p_-) = \frac{e\hbar H}{m_o^* C} \tag{30}$$

where m_o^* is the electron effective mass at the bottom of the conduction band. The magnetic field experimentally measured by magneto-resistive coils or a Hall prove can be compared with the field calculated using formula 30 and the experimental spectral peaks $2p_+$ and $2p_-$.

A number of authors have done variational calculations to theoretically predict the energies of the various donor levels (28; 23; 33). In describing the energy levels in a magnetic field, some of the authors use notation other than (n,l,m). The high field limit is $\gamma \gg 1$ and the low field limit is $\gamma \ll 1$ where

$$\gamma = h\omega_c/2R_y^* \tag{31}$$

ω_c = cyclotron frequency

R_y^* = effective Rydberg for hydrogenic donors.

There is no general agreement on how the low field numbers correspond to the high field numbers except for

$$2p(m=+1) = (110)$$
$$2p(m=0) = (001)$$
$$2p(m=-1) = (0\bar{1}0)$$

A listing of these and others from different authors are in Table III.

43
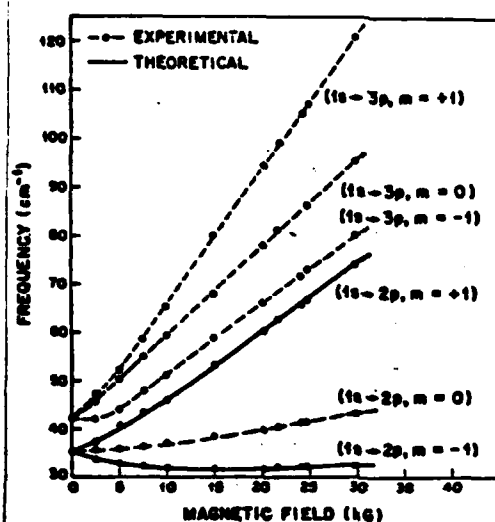
Fig.17. Energies of the (1s-2p) and (1s-3p) transitions as a function of magnetic field. The solid curves are from the variational calculation and the circles are experimental points. (38)

Table III

Correspondence between the low-field hydrogen-atomic levels (nlm) and the high-field levels (NMλ) (28)

(n l m)	Kleiner and Elliott–Loudon (NMλ)	Boyle–Howard (NMλ)
3p (m = +1)	210	112
3p (m = 0)	101	003
3p (m = −1)	1Ī0	0Ī2
2p (m = +1)	110	110
2p (m = 0)	001	001
2p (m = −1)	0Ī0	0Ī0
1s	000	000

Figure 18 shows the theoretical calculations of
Narita and Miyao where the high field quantum numbers are
used. The experimental points are those of Narita and
Miyao O , Kaplan ☐ , and Stillman ● .

According to Stillman, the previous identification
of the 1s-3p,m=0 and 1s-3p,m=±1 transitions was incorrect
(Figure 16). The 3p,m=-1,0 transitions occur at energies
between the 2p,m=0 and 2p,m=+1 transitions (Figure 19).
Also, the 1s-3p,m=0 is actually the 1s-3p,m=+1 transition.

Identification of Donors Using High
Resolution Measurements (37)

Looking at the spectra in Figure 19 shows a fine
structure for the $1s-2p_{-1}$, $1s-2p_{0}$, and $1s-2p_{+1}$ transitions.
Under lower resolution measurements this fine structure
was not observable. This fine structure shows some devia-
tion from the hydrogenic model for the donors. In fact, it
is associated with the different donors in GaAs.

The amplitude of these transitions vary depending
on the relative concentration of the various donors. The
separation between the donor peaks increases with increasing
magnetic field.

The observation of these individual donor peaks and
their dependence on the magnetic field was due to the central
cell corrections of the various donors. An electron bound
to a donor experiences the donor's Coulomb potential plus
the sum of the potential from all the other charged impurity
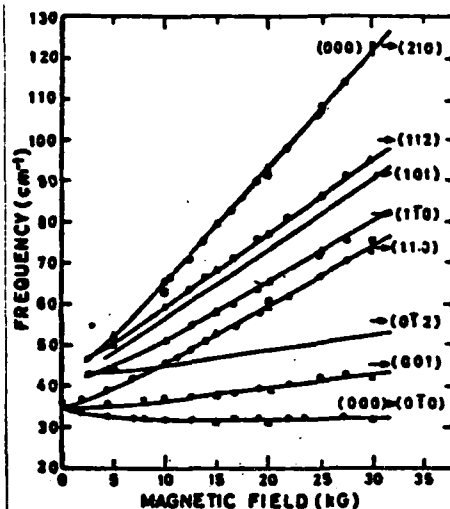
Fig. 18. Experimental and theoretical transition energies as functions of magnetic field. Solid curves are from variational calculations and circles are from experiment. Part of the experimental results obtained by Kaplan et al. (squares) and by Stillman et al. (triangles) are shown. (28)
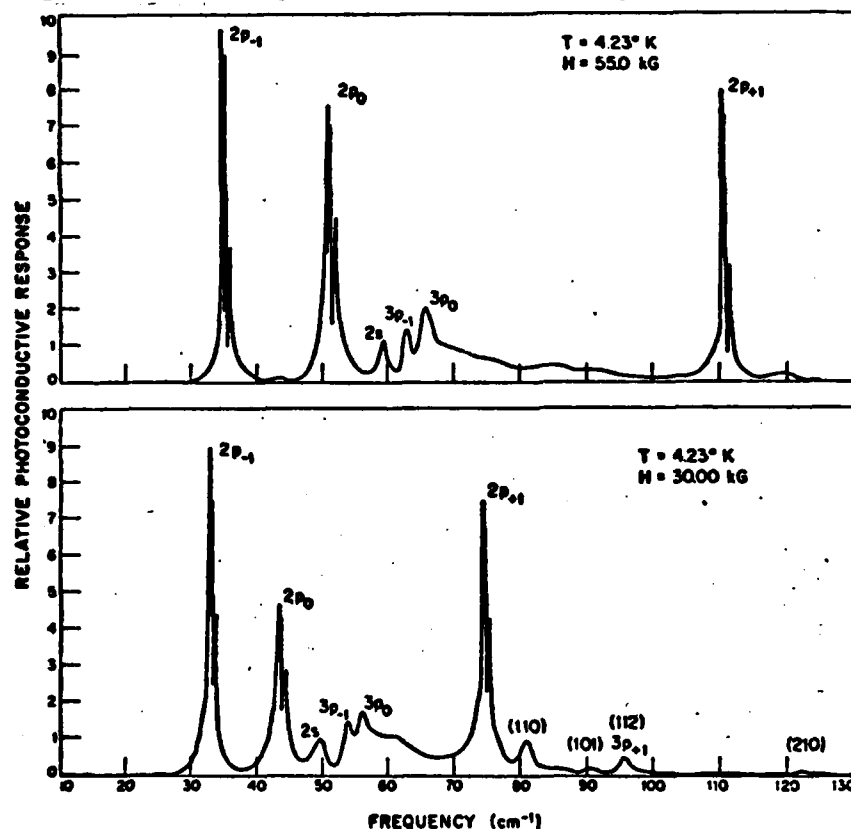
Fig. 19. High resolution (approx .16 cm⁻¹) photoconductivity spectra of a high purity GaAs sample at 30.0 and 55.0 kG showing the identification of some of the peaks resulting from transitions from the ground state to some of the higher energy levels. (37)

46

ions (23). Ions that are far away from the neutral donor contribute part of the potential, to the donor electron, that varies very little over the region of space occupied by the donor electron wave function. Therefore, only spatial variation of the Coulomb potential of ions near the neutral donor and the neutral donor's Coulomb potential affect the donor electron. If the impurity concentrations are low enough, the neutral donor Coulomb potential will have the greatest effect on the binding energy of the electron. This binding energy, therefore, will be slightly different for different donors. This effect is most pronounced for the 1s state when the electron's wave function is nonvanishing at the nucleus. The energy for the 1s state will therefore be different for each donor and the 1s-2p m=0,±1 transitions will also be different for each donor. These differences should occur at zero field but they are so small as to be unobservable. When a B field is applied, the electron's wave function is compressed around the donor's center and gets smaller as the field is increased. Thus, the 1s-2p, m=0,±1 transition for each donor species spread apart with increasing field. Also, the spectral lines are inhomogeneously broadened and become narrower with increasing field (23).

The donors in GaAs come from the column IV and VI of the periodic table. When a column IV element is substituted at a Gallium site, a donor results. The same is true when

a column VI impurity is substituted on an Arsenic site. The common donors in GaAs are silicon, germanium, tin, lead, sulfur, selenium, tellurium. Carbon will incorporate preferentially as an acceptor (32). Oxygen is believed to be difficult to incorporate in GaAs and has not been identified using photoconductivity.

To identify the donors using photoconductivity in a magnetic field, the 1s-2p, $m=\pm1$ transitions are used since they become dominant in a magnetic field. Figure 20 shows the 1s-2p $m=-1$ transitions of three donors. These are the dominant donors in vpe GaAs (32). X_1 is associated with silicon, X_2 with sulfur and X_3 with germanium.

It is with this method that impurities are identified in high purity GaAs. Research is continuing to identify positively other donors in GaAs.
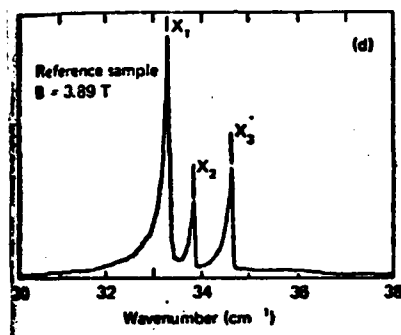
Fig.20. High resolution spectra of the 1s-2p (m=-1)
transition in a n=4.1E13 sample. (25)

IV. Experimental Apparatus

The experimental setup is shown in Figure 21. The modulated radiation is directed from the spectrometer into an optical transfer box. The transfer box directs the light vertically into the gold coated lightguide. Two superconducting magnet systems were used for the experiment. The light irradiates the GaAs sample whose signal is directed into a preamplifier. The signal from the preamplifier goes to the spectrometer electronics where it is digitized and then to the minicomputer system where the signal is processed and displayed.

A detailed discussion of the Fourier transform spectrometer, lightguide system, two superconducting magnet systems, spatial extent of the magnetic field, preamplifier and photoconductive circuit, sample holders and filters, and the computer system follows in this section.

Fourier Transform Spectrometer - Nicolet 8000 FTIR (29; 30; 31)

The spectrometer is enclosed in a rectangular box and elevated with metal legs (Figure 21). Underneath the box is all the electronics and associated equipment used to operate the spectrometer. The spectrometer is connected by cables to a minicomputer. Access to the optics, beamsplitter and sources is accomplished by lifting the top off the box
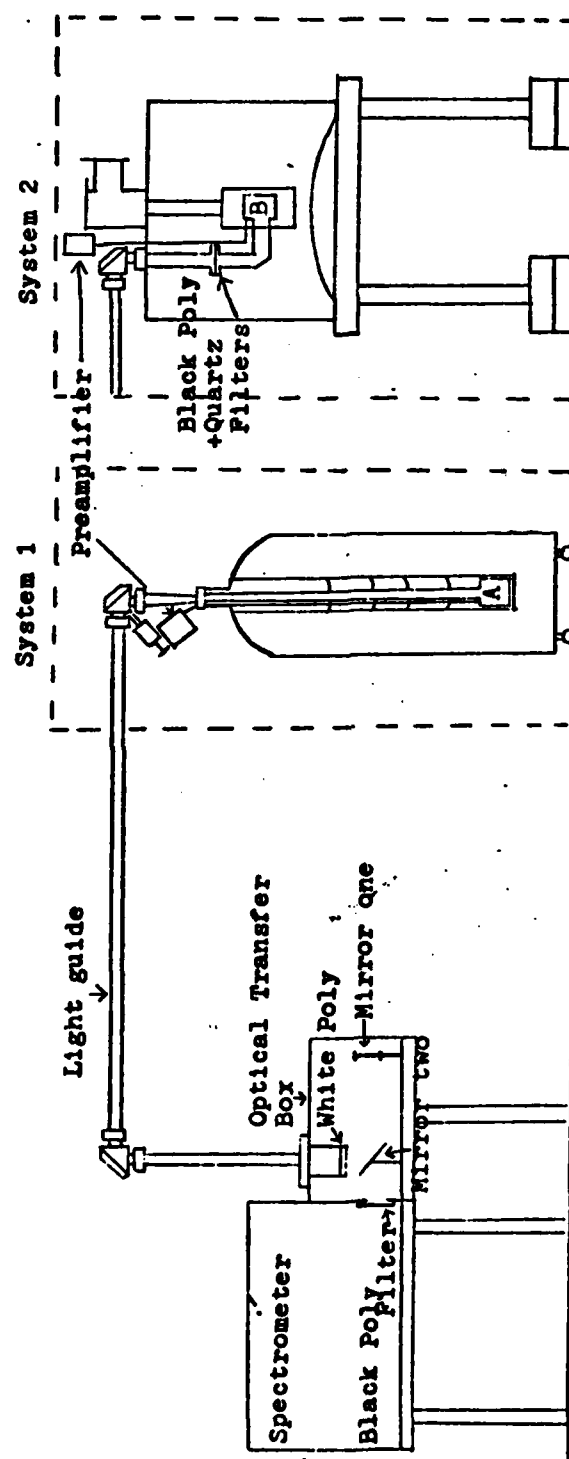
Fig.21. Experimental Setup

51

by a hoist. A view inside the spectrometer is shown in Figure 22.

The two sources in place for this experiment are a mercury arc (S2) and a carbon globar source (S1) (Figures 22, 23, 24). Access to either source is accomplished by typing the three letter code SRC (see p. 130) and using 1 for S1 or 2 for S2. The computer will position mirror MF1 to direct the radiation, from the source chosen, through the aperture A1.

The aperture is selected using the command APE (see p. 129). The computer will ask for a beta. Beta is defined as:

β = aperture diameter/focal length of collimation mirror

β = diameter in mm/208mm for 8000 FTIR

The effect of the aperture on the system resolution is shown in Figure 25. When working at $35cm^{-1}$, the aperture degrades the resolution very little when it is fully open. By opening it up, more radiation is collected at the detector. The optimum aperture setting for the GaAs photoconductivity is β=.04.

After passing through the aperture, the light strikes mirror M1 then M2 and enters the Michelson interferometer. The fixed mirror is M4 and the moving mirror is M3. The white light source (WLS) and detector (WLD) determine when the path lengths to M3 and M4 are equal. The

52
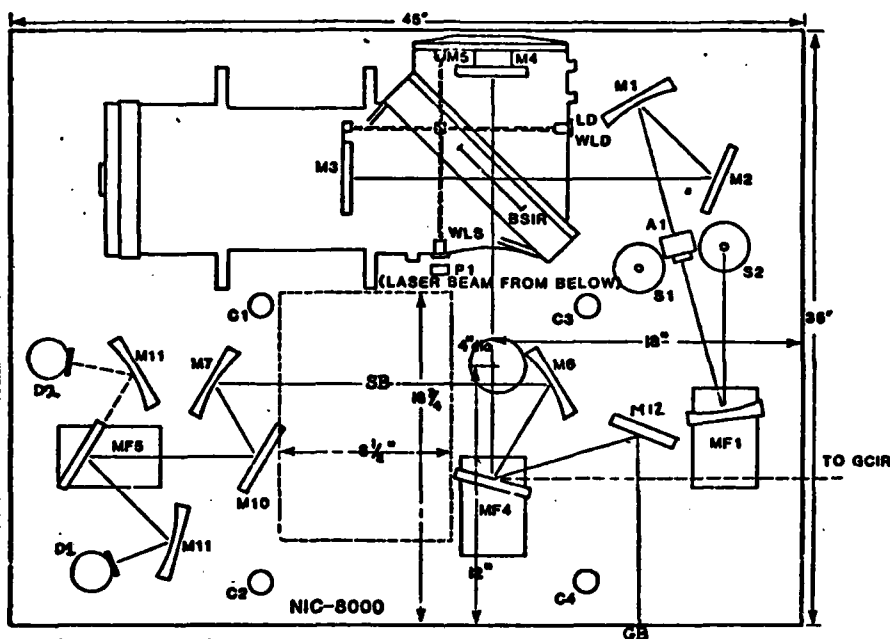
S1,S2	Standard source positions.
MF1	Computer controlled source selection mirror, spherical, 4.5" E.F.L.
A1	Computer controlled aperture.
M1	Collimating off-axis parabolic mirror, 8.2" E.F.L.
M2	Flat mirror.
M3	Moving mirror assembly.
M4	Fixed mirror (I.R. beam).
M5	Fixed mirrors (white light and reference laser).
BSIR	Infrared beamsplitter.
LD	Reference laser detector.
WLD	White light detector.
P1	Laser prism (laser mounted below optical chamber)
MF4	2-position, computer controlled flat mirror
M6	Sample focusing mirror, off-axis parabola, 9.3" E.F.L.
M7	Sample collection mirror, off-axis parabola, 9.3" E.F.L.
M10	Flat mirror.
MF5	2-position, computer controlled, detector selection mirror, flat.
M11	Detector focusing mirror, off axis parabola 3.5" E.F.L.
D1,D2	Standard detector positions.
C1,C1,C3,C4	Support columns.

Fig. 22. Optical system inside Nicolet 8000 spectrometer. (31)

53
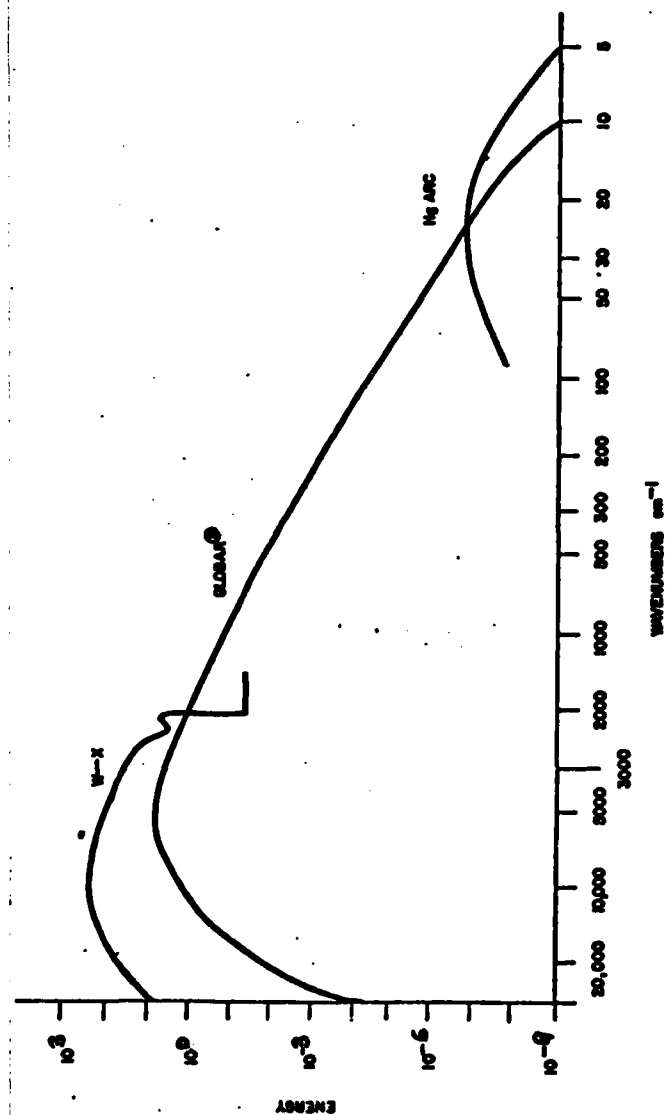
Fig.23. Light Sources (31)

54
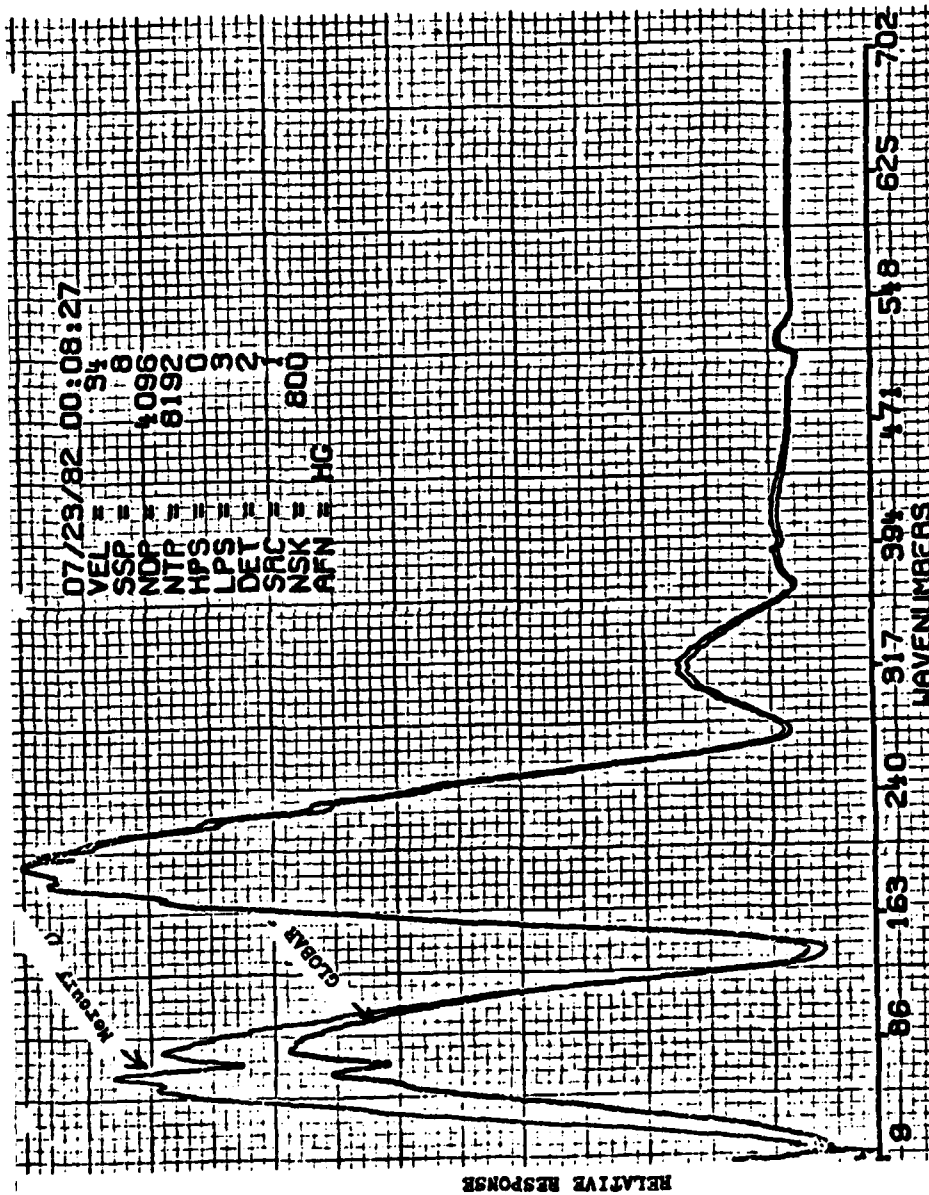
Fig. 24 Comparison of output of mercury arc and globar sources.

55

Resolution (FWHM), cm^{-1}

6.35 mm (FL)

2.31 mm (MD)

1.14 mm (SM)

1

.1

.01

.001

10,000   1000   100   10

Wavenumbers cm^{-1}
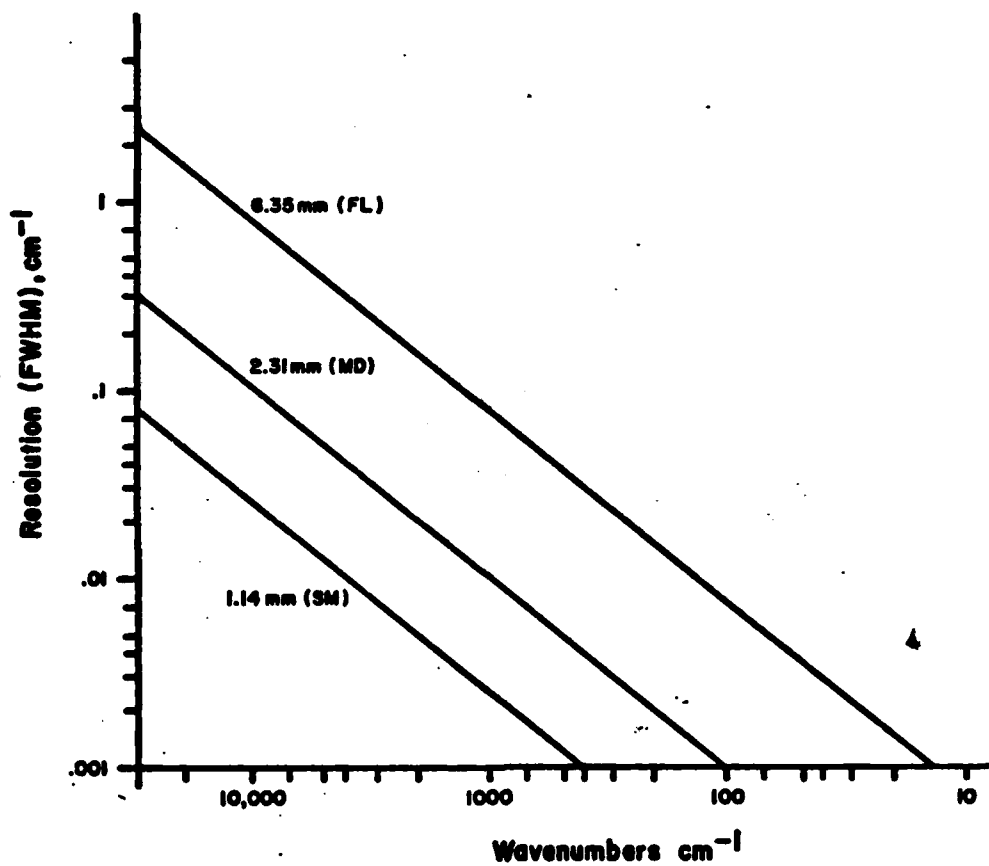
Fig. 25. Effect of aperture on resolution. (29)

56

laser beam (P1) and detector (LD) are used to determine when to take a data point.

The moving mirror M3 rides on a cushion of air. The velocity of the mirror can be varied to change the modulation frequency in order to maximize the response of the detector. The three digit code is VEL (see p. 130) and the numbers go from 0 to 57. The mirror speeds associated with the numbers are in Table I.

The beamsplitters (BSIR) used in the far-infrared region are made of Mylar. Their spectral range and efficiency depends on the thickness of the material (Figure 26). Figures 27, 28, and 29 show how the efficiency is affected by constructive and destructive interference caused by different path differences in a given thickness of material. The higher wavenumber cutoff is due to a 700cm filter at the detector. The spectrum resembles a cosine squared pattern with the beamsplitter efficiency being periodically repeated. The constructive interference peaks and destructive interference peaks obey the following equation:

$$m\lambda = 2\ell\left(n^2 - \tfrac{1}{2}\right)^{\tfrac{1}{2}}$$

m=0,1,2,3... for destructive interference
m=$\tfrac{1}{2}$,3/2,5/2.. for constructive interference
ℓ=thickness of Mylar   (32)

where $n \cong 1.85$ for Mylar. The best beamsplitter for the region of 20cm^{-1} to 100cm^{-1} is the 25 micron beamsplitter

Fig. 26 Beamsplitter efficiencies.(31)

58
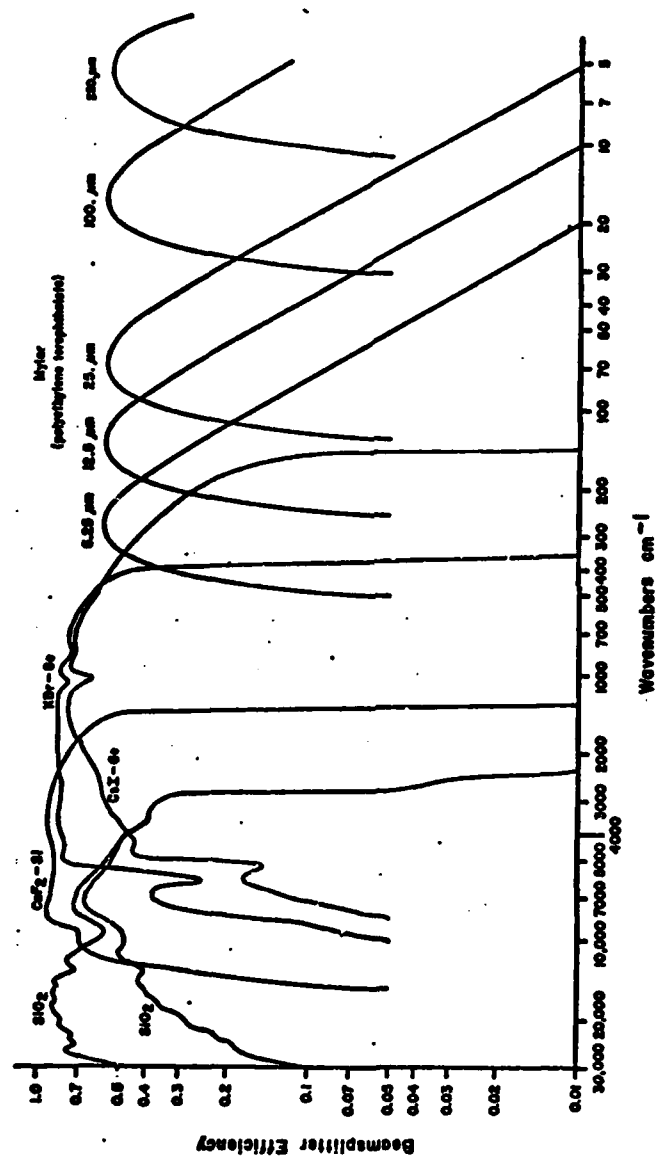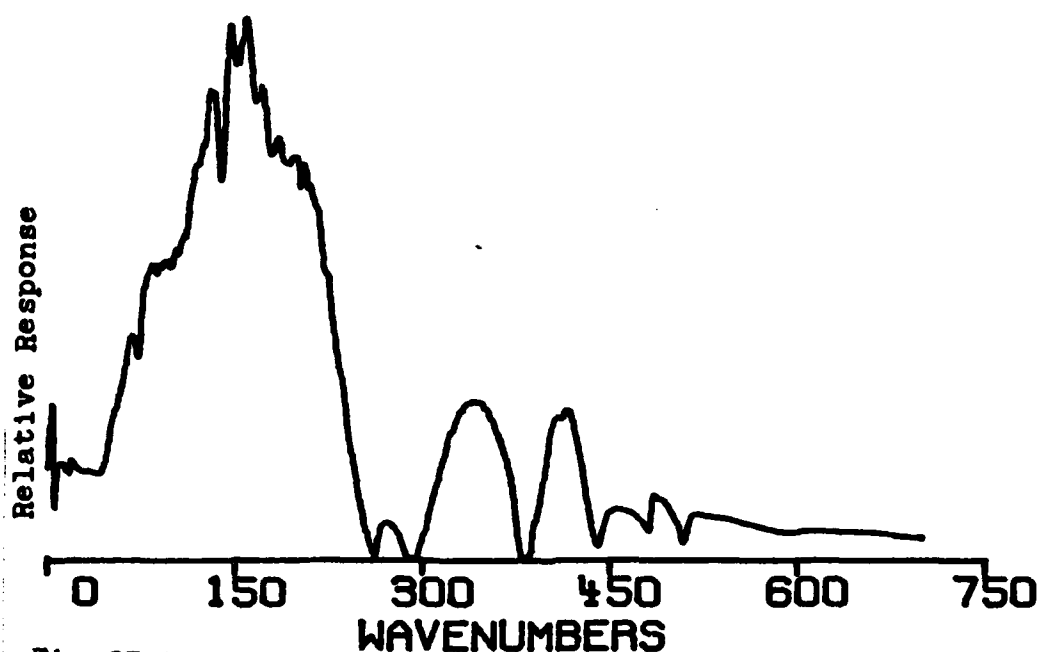
Fig. 27. Mercury arc spectrum using 12.5 micron beamsplitter. High wavenumber cutoff is due to a 700 cm^{-1} filter in the detector.
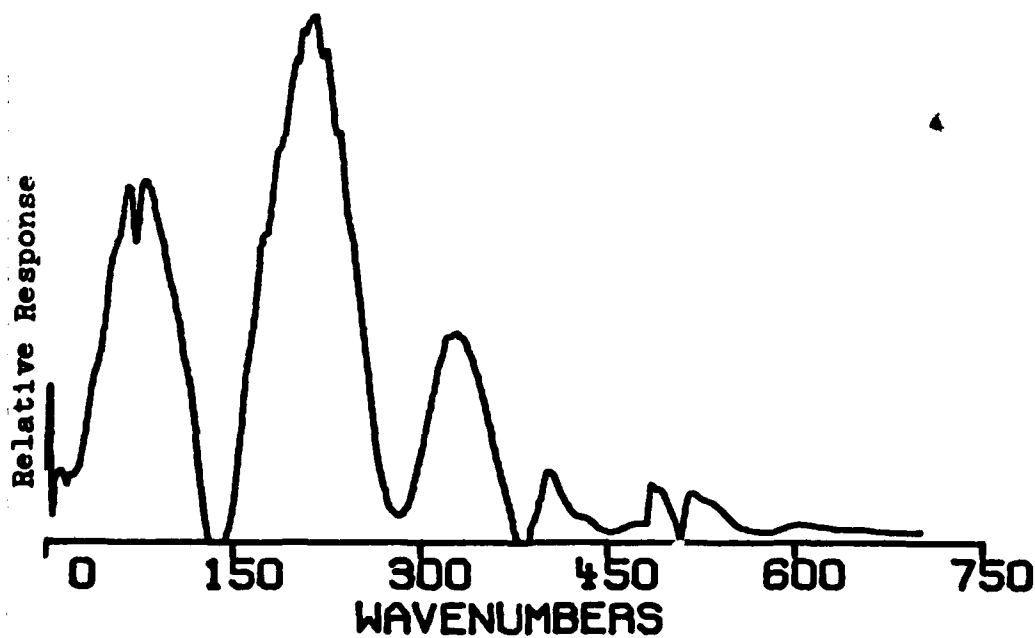
Fig. 28. Mercury arc spectrum using 25 micron beamsplitter. High wavenumber cutoff is due to a 700 cm^{-1} filter in the detector.
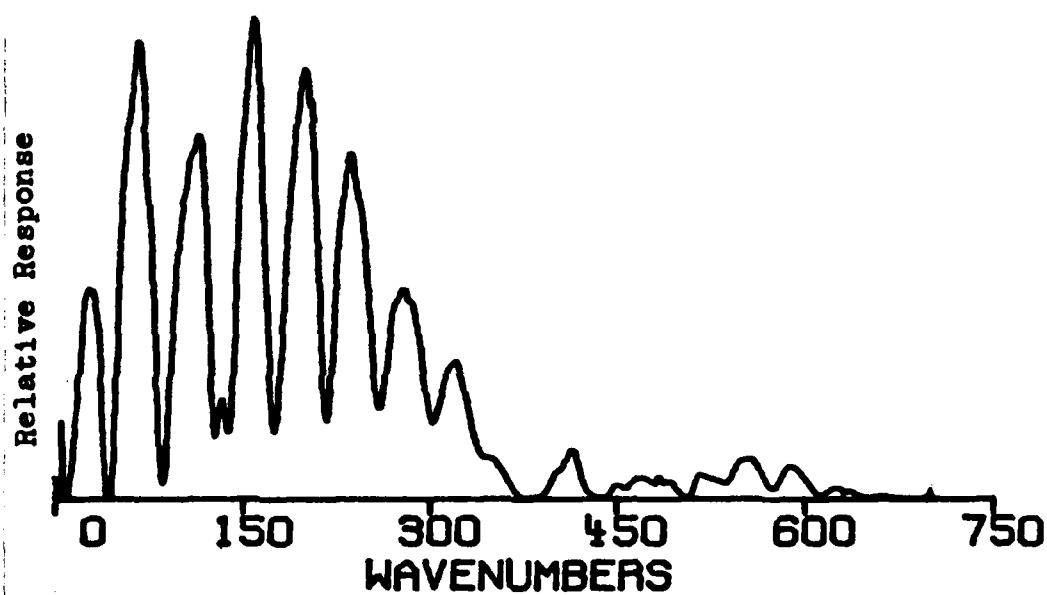
Fig. 29. Mercury arc spectrum using 100 micron beamsplitter. High wavenumber cutoff is due to a 700 cm^{-1} filter in the detector.

since it allows the most energy through and has no zero points in this region. It was what was used in the experiment.

The modulated infrared signal exits the Michelson interferometer and reflects off mirror MF4. MF4 is also computer controlled. The code for MF4 is MIR. When GB is input, the mirror swings to direct the signal to mirror M12 and out on opening (GB) where the optical box is located. The code SB will direct the beam to mirror M6 and through position SB where a sample for transmission studies is normally placed. The beam then hits mirror M7, M10 and MF5. The code for MF5 is SRC (see p. 130). When one is input, the beam goes to detector one (D1) which is a TGS room temperature detector. Code 2 will direct the beam to detector two which is a helium cooled bolometer. The detectivity of the TGS detector and the helium cooled bolometer is shown in Figure 30. The bolometer unit is attached to the outside of the rectangular spectrometer box. The bolometer has essentially a flat response in the wavelength region of interest for this experiment. It is used to take a background spectrum to compare the GaAs photoconductivity spectrum against to eliminate source and beamsplitter characteristics from the photoconductivity spectrum. The entire spectrometer box is mechanically pumped to a pressure of approximately 16 Torr.
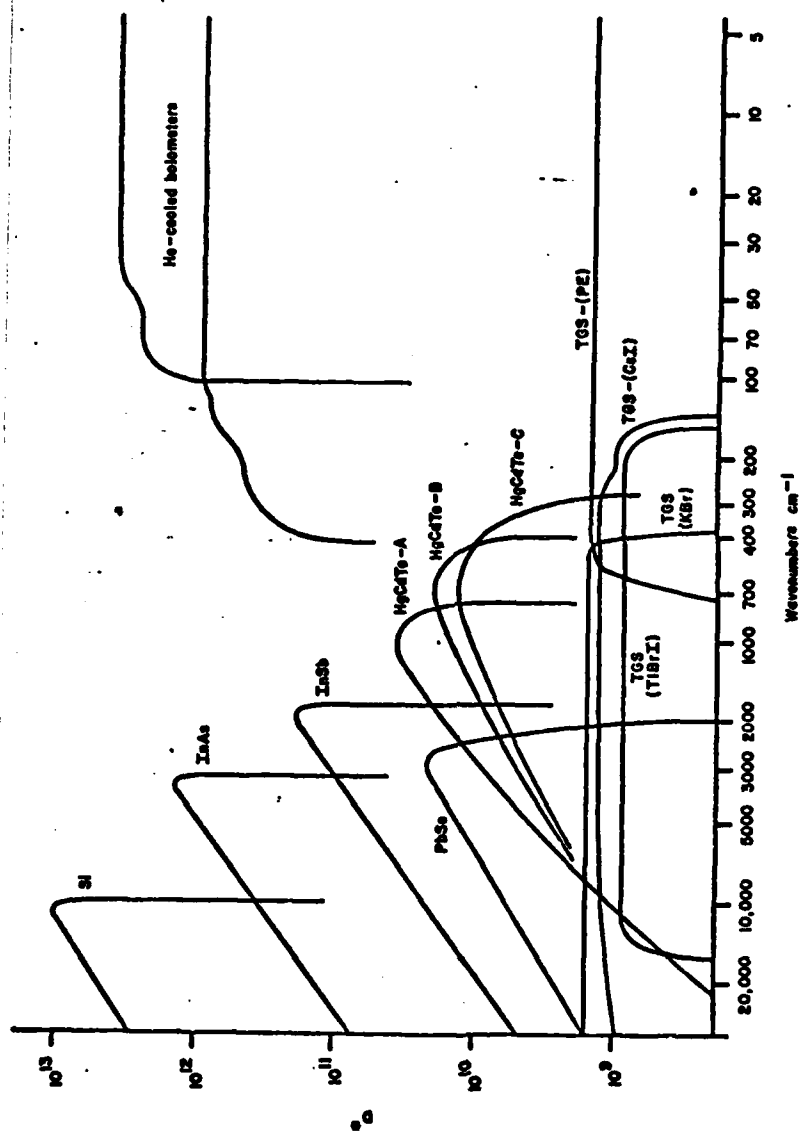
Fig.30. Sensitivity ranges of detectors. (31)

Lightguide System (4; 5)

The lightguide system to transfer the light from the spectrometer unit to the sample consists of eight main pieces: optical transfer box; five gold-coated Advanced Kinetics lightguide pieces; and two stainless steel pieces with a sample chamber attached at one end (Figure 21). One of the Advanced Kinetics pieces and the sample chamber pieces are used depending on which superconducting magnet is used. The optical transfer box and four of the Advanced Kinetics lightguide pieces are common to both systems.

The optical transfer box is made of aluminum and contains two parabolic mirrors (focal lengths of 2.5 inches and 8.3 inches). They are arranged as shown at a distance of $f_1 + f_2$. A collimated four-inch beam parallel to the floor comes from the spectrometer and hits mirror one. After reflecting off mirror two, the beam is now 1.2 inches in diameter and perpendicular to the floor. The beam now enters an Advanced Kinetics lightguide system.

The first element is a type F/O which has a 100mm opening at the entry end where a white polyethylene filter is mounted to separate the lightguide vacuum from the optical box and spectrometer vacuum area, and still allow far-infrared radiation to pass through. The white polyethylene filter is flexible to allow for differential pressure between the optical box and lightguide. The exit end of this piece is

25mm in diameter and it is 46cm long. The F/O piece is connected into a 90 degree angle bend piece.

The two 90 degree angle bend pieces are Advanced Kinetics Model G. One of them had a Veeco valve welded in so that there was a port to evacuate the lightguide. The two are interchangeable, but when using the RCA magnet, the one with the Veeco valve must be connected to the type F/O piece since the top of the RCA magnet dewar interferes with its placement on top of the dewar.

The long straight piece is a type A which is 25mm in diameter and 60cm long.

When using system one, a tapered piece is connected to the 90 angle bend piece. It is tapered from 25mm to 12mm to condense the light to match the diameter of the final stainless-steel guide. The final piece is placed inside the center bore of the dewar so the sample compartment is located at the center of the magnetic field.

System 2 does not use the tapered piece. The 90 degree angle bend piece is connected directly to the final stainless-steel guide and sample holder. The steel guide has a 90 bend so the sample compartment can fit into the bore of the magnet.

The lightguides are gold coated and are evacuated to 10^{-6} Torr to prevent absorption of infrared radiation and to prevent any condensation on the filters or sample when the system is cooled to liquid helium temperatures. The

transmission as a function of wavelength per meter of pipe is shown in Figure 31. The radiation can be bent around the 90 degree corners with 90-95% transmission.

Intermagnetics Superconducting Magnet and Janis Dewar (21)

An Intermagnetics superconducting magnet (SO-9123) is mounted inside a metal Janis dewar (Figure 32). The dewar is approximately 54 inches tall and 16 inches in diameter. The dewar is mounted in a metal stand that has wheels to make the dewar portable. The dewar can also be raised and lowered about one foot in order to allow mating of the lightguide pieces. The outer chamber contains a vacuum (10^{-7} torr) to shield the inner nitrogen and helium liquid chambers. The helium and nitrogen reservoirs are made of stainless-steel and are filled through ports on top of the dewar. The reservoirs are also protected from radiation heating by a radiation shield made of a thin metal foil which is wrapped around the reservoirs. The superconducting magnet is housed in the helium reservoir. The helium level is read from an Intermagnetics helium level indicator. The center bore is separate from all reservoirs and the outer vacuum chamber. It contains the final lightguide piece and sample chamber.

The magnet is a split coil type composed of Nb_3Sn ribbon. The magnet can produce 128.6 kiloGauss at a maximum current of 135 amps. The rated homogeneity is 100 gauss in

65
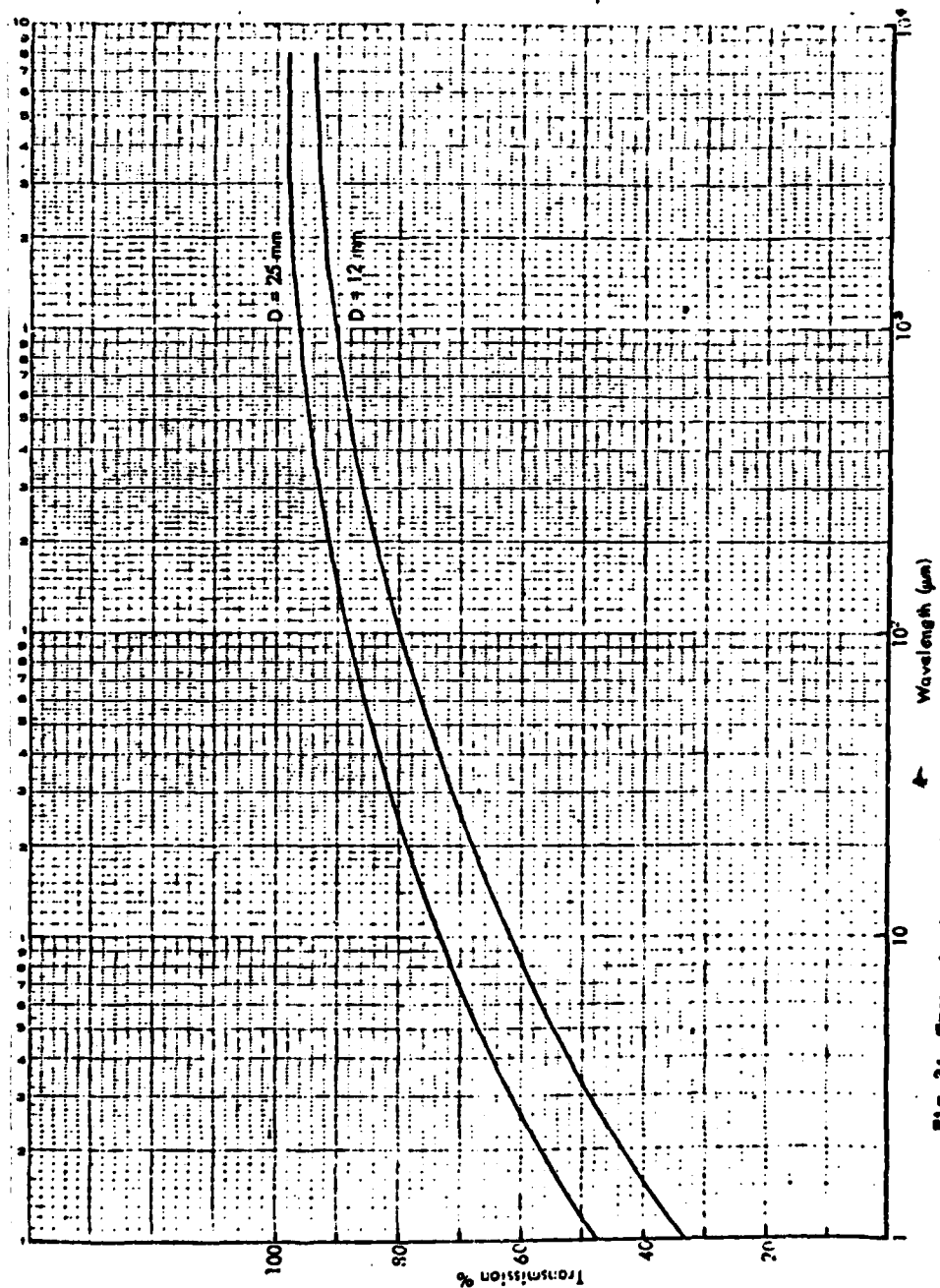
Fig. 31. Transmission of lightguides versus wavelength (5)
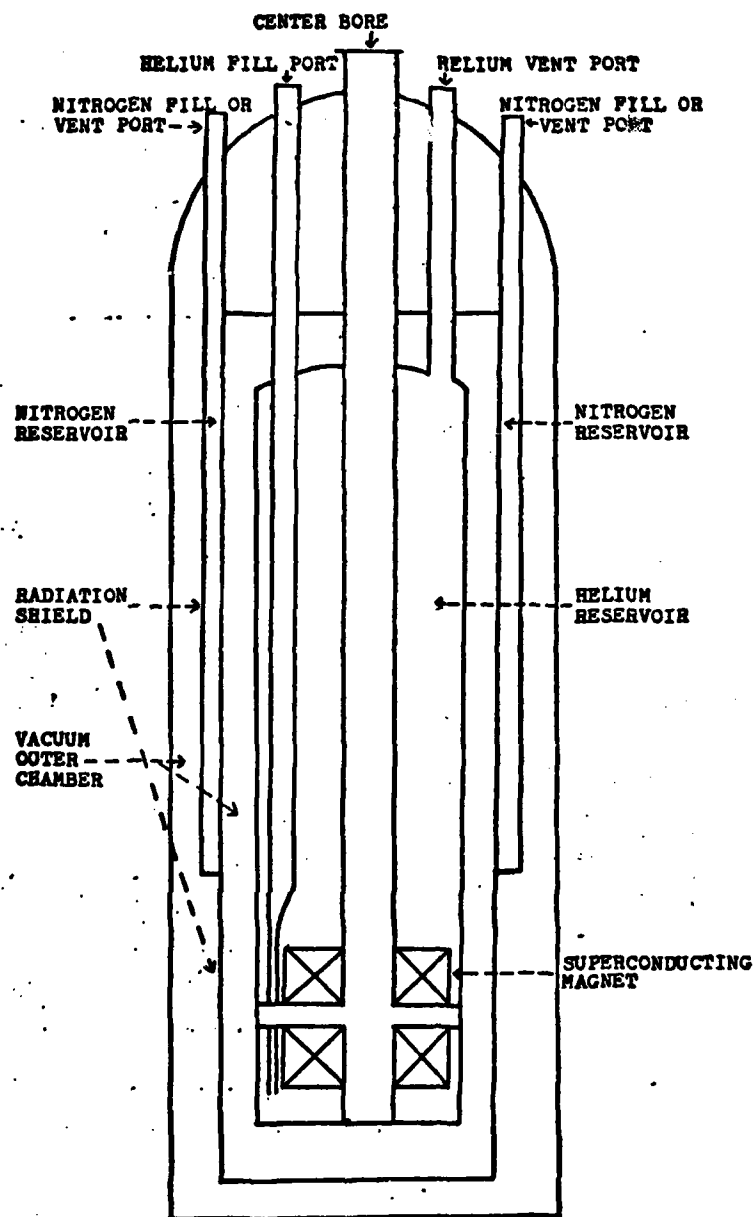
Fig.32. System one:Intermagnetics superconducting magnet and Janis dewar.

a one cm spherical volume at the center of the bore (DSV).
The bore diameter is 1.25 inches. A plot of the magnet field
versus current is in Appendix A. The power supply for the
magnet allows the current to be slowly swept until the
desired field is reached. The desired charge rate is in
Appendix A.

Two magneto-resistive coils are mounted in the bore
at the center of the magnet. By measuring the resistance
of the coil, comparing it with the zero field resistance R_o
and using the chart in Appendix A, the magnetic field is
determined.

RCA Superconducting Magnet and Cryofab Dewar (34)

An RCA superconducting magnet, type SM2829 split
coil type made with Nb_3Sn superconducting ribbon, is mounted
inside a Cryofab dewar. The dewar is made of stainless
steel and is 93cm high and 68cm in diameter. The dewar
structure is shown in Figure 33.

The outer chamber contains a vacuum (10^{-6}torr) to
shield the next chamber, which is filled with liquid nitro-
gen, from outside heat. The next chamber is made of glass
and is also pumped to 10^{-6}torr. It shields the large inner
chamber which houses the magnet and is filled with liquid
helium.

To prevent the magnet from going normal, it is
necessary to keep the liquid helium level above the top of
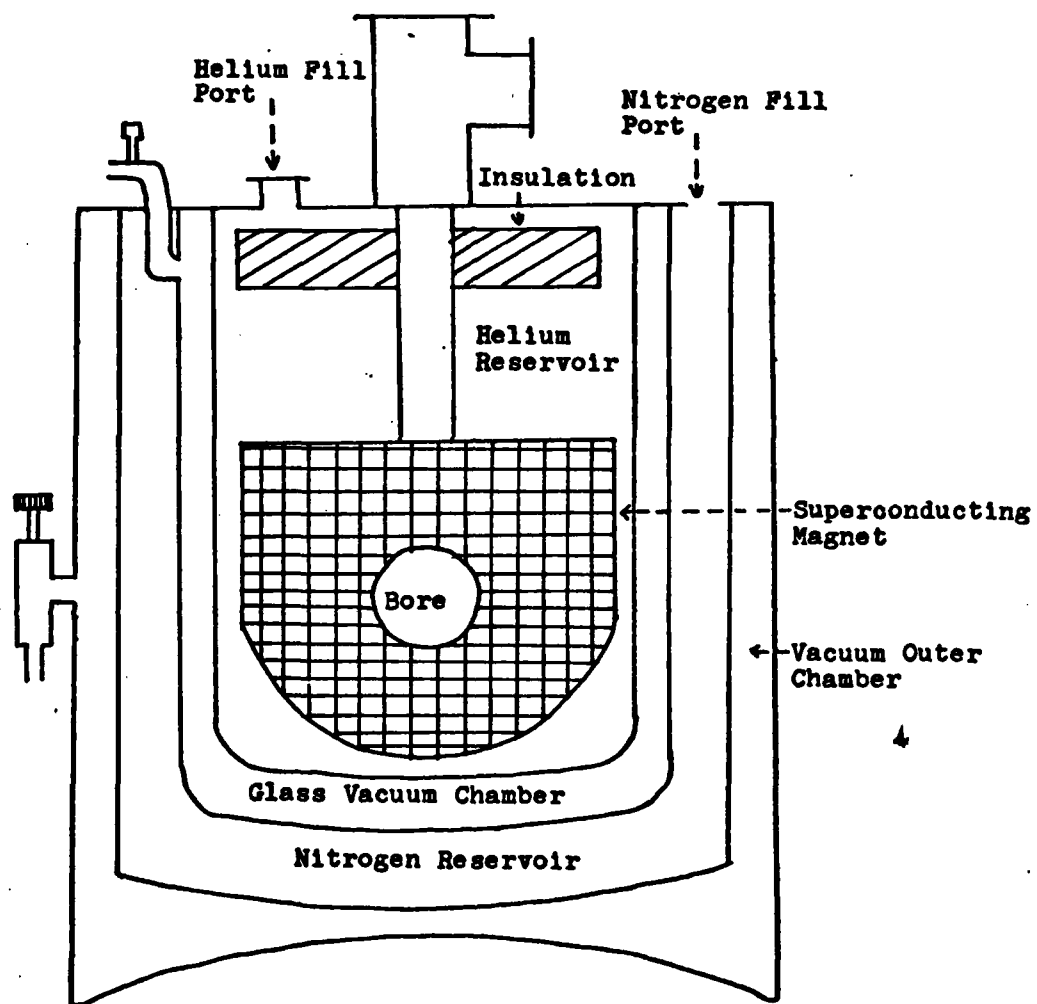
Fig. 33. System two: RCA superconducting magnet
and Cryofab dewar.

the magnet. The liquid level was determined by the carbon resistors (Figure 34). The resistors have a room temperature resistance of 100 ohms, liquid nitrogen temperature resistance of 150 ohms, and liquid helium temperature resistance of 1400 ohms. . When the helium level drops below one of the resistors, its resistance will drop noticeably. The resistance was monitored using a Simpson ohm meter.

The magnet is suspended in the dewar by a metal shaft which is threaded to the top of the dewar (Figure 33). The magnet has the following dimensions and weight:

$$Length = 12 \text{ inches}$$

$$Width = 5.9 \text{ inches}$$

$$Height = 12.1 \text{ inches}$$

$$Bore \text{ } diameter = 2.5 \text{ inches}$$

$$Weight = 165 \text{ pounds}$$

The maximum rated field is 100kG at 91 amps. The homogeneity is 1 percent in one inch DSV. A plot of the magnetic field versus current is shown in Appendix A. The current is supplied by a Ventron CFC-100 power supply which is rated to a maximum current of 100 amps and three volts. The power supply has a heater to operate a persistent current switch on the magnetic. The current to the magnet can be slowly swept from .1 amp/min to 20 amp/min. The recommended sweep rates are:
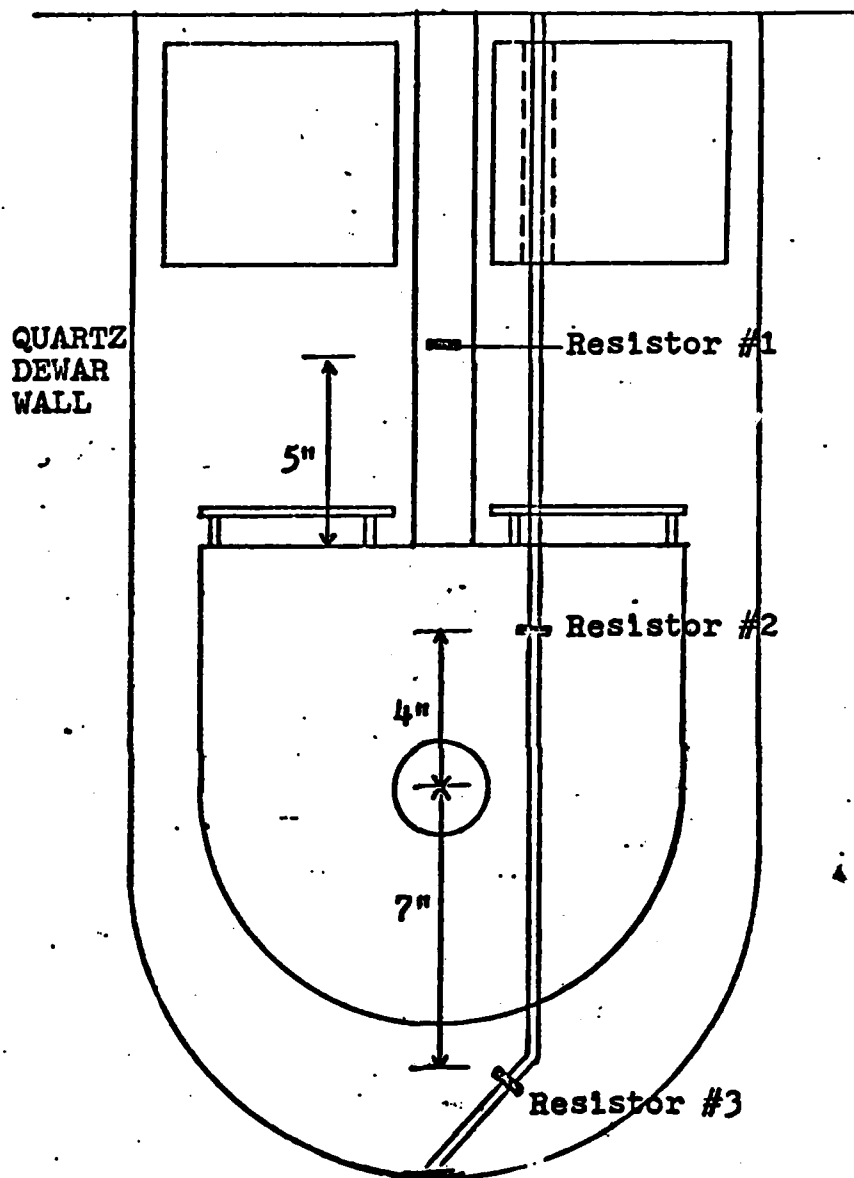
Fig. 34. Placement of Resistors Inside Dewar for Liquid Level Measurement. (17)

71

2 amp/min to 60 amps

hold for 5 min

1 amp/min to 91 amps

Two magneto-resistive coils are mounted in the bore at the center of the magnet. By applying a 50 milliamp bias current and reading the voltage on a digital multimeter, the magnetic field is determined using the curves in Appendix A.

Spatial Extent of Magnetic Field

When the superconducting magnet is operated at high fields, electronic equipment near the magnet could be adversely affected. The magnetic field in the horizontal plane for system two has been measured (Figures 35 and 36). Where possible, electronic equipment was kept as far away as possible. However, to keep the RF noise down, the preamplifier was located on top of the magnet dewar. Also, the length of the lightguide optics limited how far the magnet could be located from the spectrometer electronics. The minicomputer location was changed but it still was approximately nine feet from the magnet. It did not show any adverse effects from the magnetic field.

Preamplifier and Photoconductive Circuit

The circuit used to detect the photoconductivity in GaAs is one used in a number of detectors. A battery is used as a low noise bias for the circuit. The available
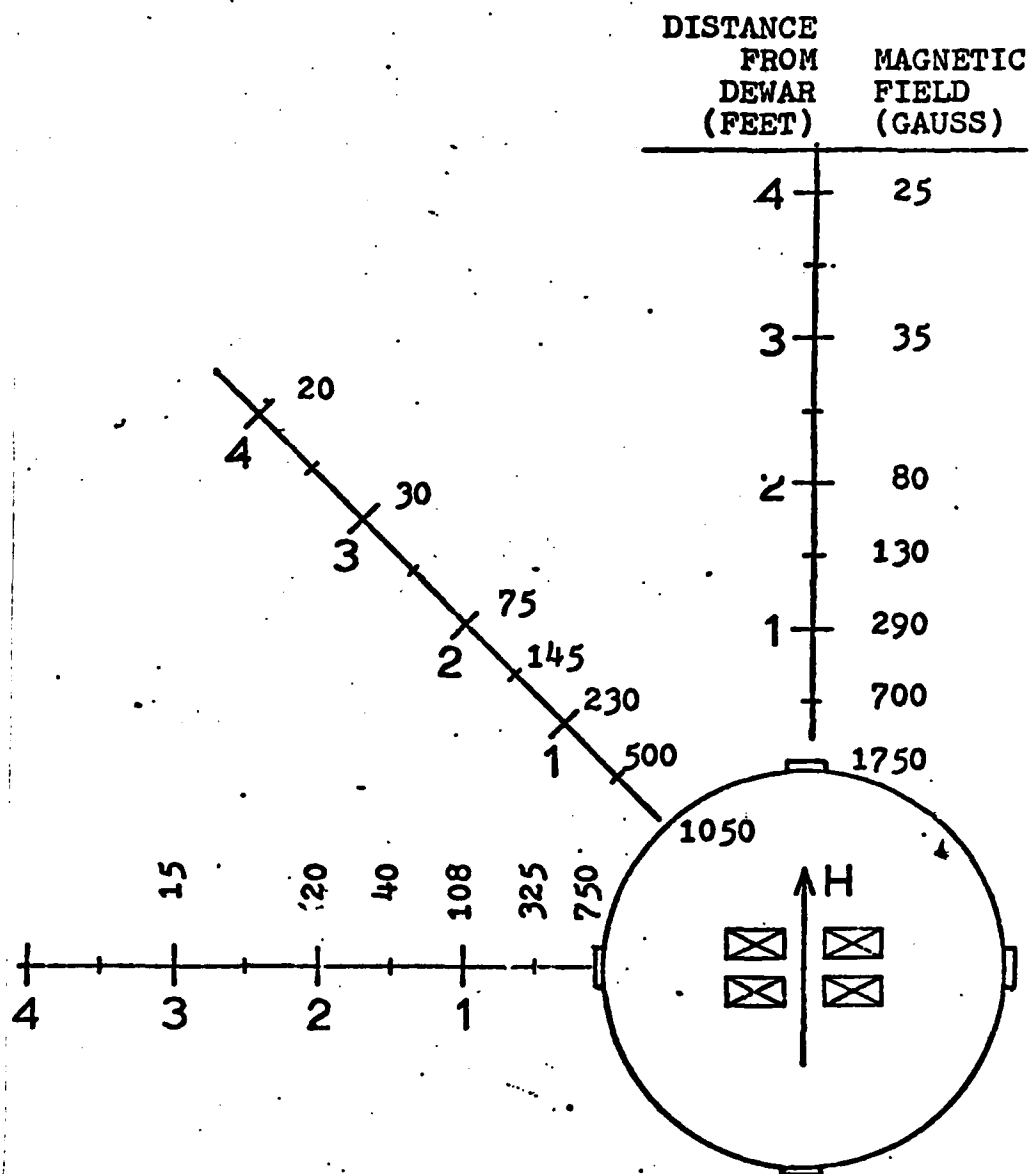
Fig. 35. Magnetic Field Strengths in Area Surrounding the Dewar. All measurements were made in the horizontal plane of the magnet bore with a full strength of 55 kGauss at the magnet's center. (17)

73
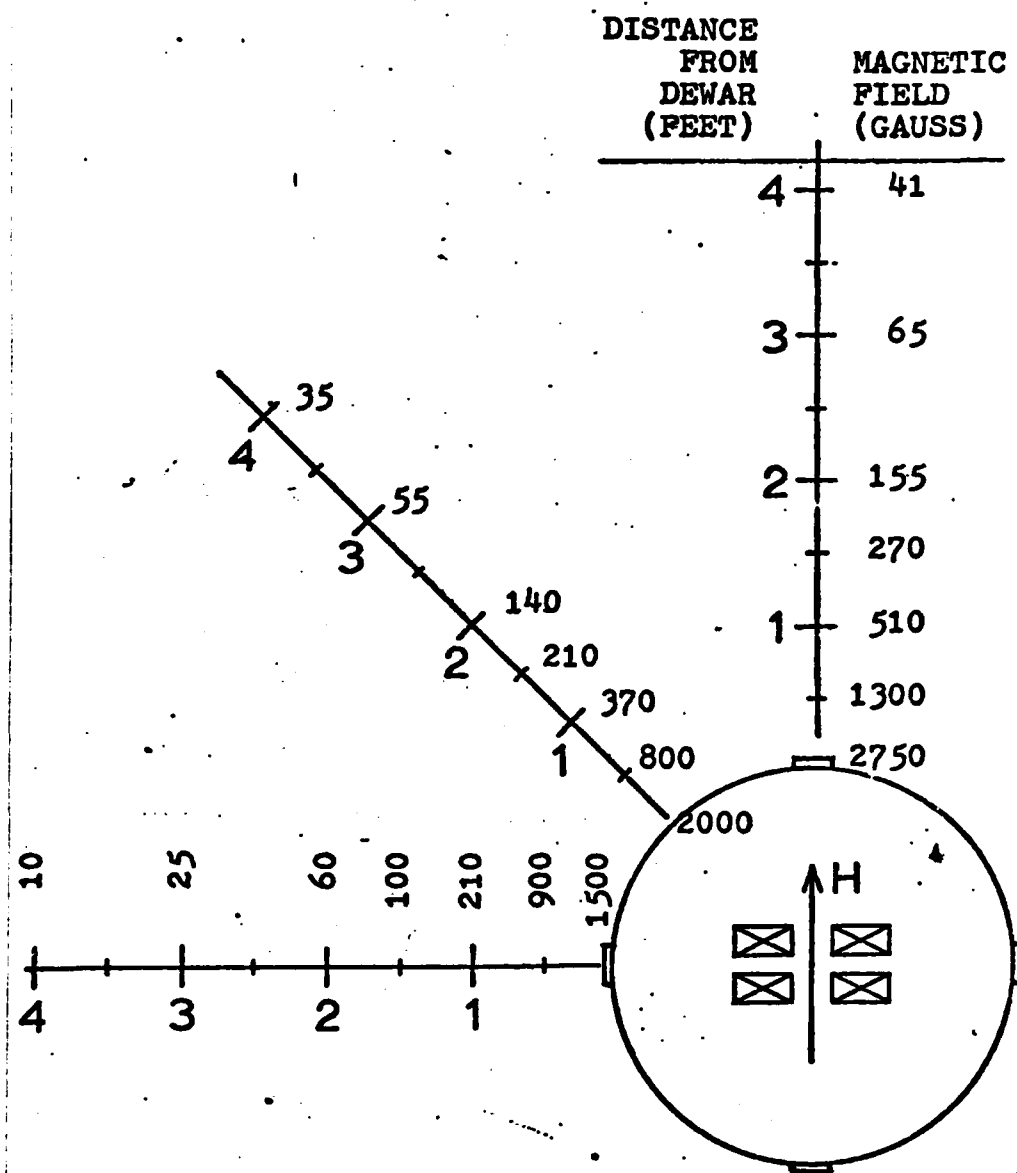
Fig. 36. Magnetic Field Strengths in Area Surrounding the Dewar. All measurements were made in the horizontal plane of the magnet bore with a full strength of 94.6 kGauss at the magnet's center. (17).

```
                    ┌──────────────────┐  R
                    │  Load Resistor   │⌇  ᴸ
Battery    ─┤├──────┤                  │   R
                    │                  │    ˢ ─────┌──────────────┐
                    │                  │⌇          │              │
                    └──────────────────┘   Gˢ      │ Preamplifier │
                                                   │              │
                                                   └──────────────┘
```
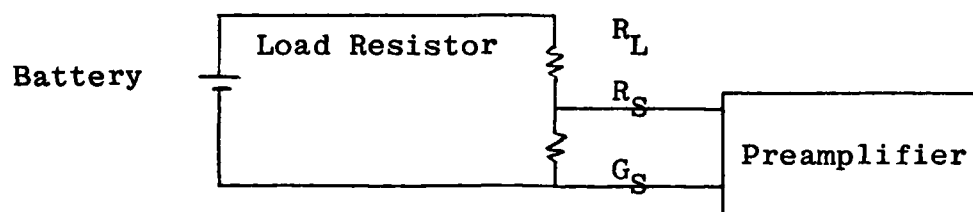
battery voltages are 1½, 9, 15, 22.5 volts and any combina-
tion of them. The battery is connected in series with the

sample and a load resistor. The load resistors used are

small carbon resistors with the insulation scraped off. The

insulation was scraped off to get better heat conduction.

The load resistor is placed in the sample chamber to keep it

cool (4.2°K), thereby reducing its noise. Since carbon

resistor's resistance changes with temperature, a number of

resistors were placed in liquid nitrogen and liquid helium.

The resistances are tabulated in Table V. The wires marked

R_s, G_s and R_L are run from the sample chamber·through a

stainless steel pipe and directly into a Infrared Labora-

tories LN-6 preamplifier (Appendix B) which is located on

top of the magnet dewar in both systems (Figure 21). This

arrangement eliminates as much RF noise as possible. The

preamplifier is a low noise unit with a gain of 100 or 1000.

The signal then goes to the Analog-to-Digital converter in

the spectrometer. The spectrometer electronics allows a

further gain of up to 128 resulting in a maximum gain of

128,000 for the system.

Sample Holders and Filters

In this experiment, the sample is the detector and located in a special compartment at the end of the lightguide (A,B in Figure 21). The sample holders are posi-tioned at the center of the magnet's bore. The final lightguide piece and sample holder are different for the two systems. Also, the type and location of the filters are different.

The sample compartments (Figures 37 and 38) are made of stainless steel. The light enters as shown (perpendicular to the samples surface) while the magnet field is also perpendicular to the sample (Faraday configuration). The Voight configuration (B field parallel to sample surface) is more difficult to achieve optically but it would reduce magneto-resistive effects at high magnet fields.

System One. The system one sample chamber is shown in Figure 37. The sample is mounted in a rectangular cavity carved from a cylindrical piece of oxygen free high conduc-tivity (OFHC) copper (D). This sample mount is screwed into another piece of OFHC copper (C) which is bolted onto the stainless steel cavity. An indium O-ring forms a seal which will hold a vacuum at liquid helium temperatures.

The sample is mounted to the copper using G. E. varn-ish which is mixed with a 50/50 solution of acetone and toulwene until the mixture has the consistency of water. This solution secures the sample to the copper while also
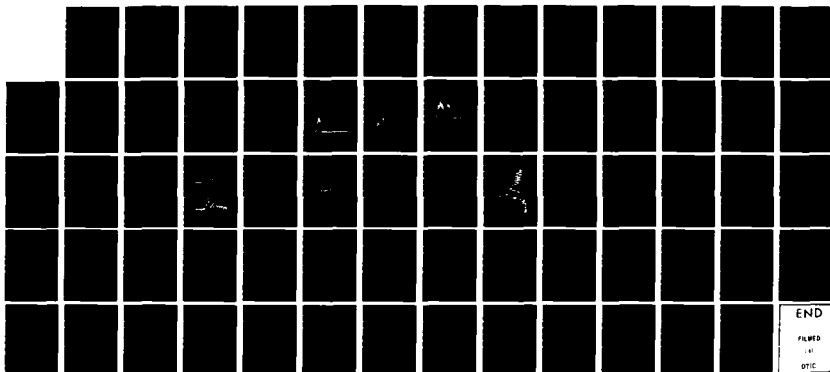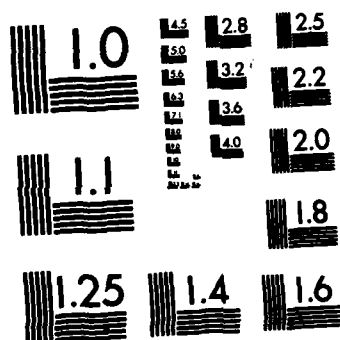
MICROCOPY RESOLUTION TEST CHART

NATIONAL BUREAU OF STANDARDS-1963-A
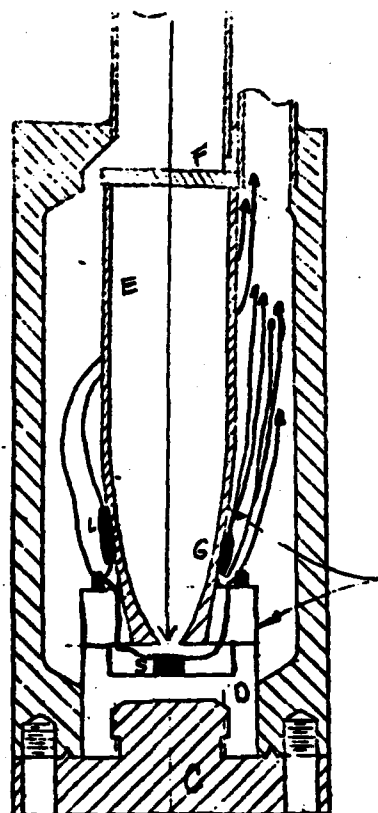
Fig.37. System One Sample Chamber
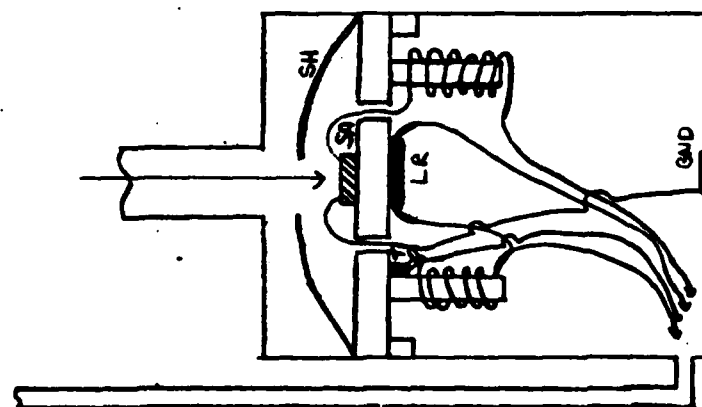
Fig.38. System Two Sample Chamber

77

allowing the best possible heat conduction. The G. E. varnish solution and the semi-insulating GaAs substrate provides suitable electrical insulation for the epitaxial GaAs layer.

The most common way of mounting GaAs samples is to glue an insulator such as ruby, sapphire or beryilla to the copper and then glue the sample to the insulator. This arrangement did not provide good heat conduction compared to the G. E. varnish.

On top of the sample mount is a gold plated Winston cone (E). The wires from the sample (teflon coated) come up through two small holes in the Winston cone base and are soldered to two standoffs on the Winston cone base. One end of a load resistor (L) is soldered to one standoff. The load resistor is attached to the Winston cone with G. E. varnish. On the other side of the cone, a germanium thermometer (G) is attached to the Winston cone with G. E. varnish. The four wires from the germanium resistor, one from the load resistor, and one from each of the two standoffs go up to the preamplifier through a steel tube.

On top of the Winston cone a cold filter is placed (F in Figure 37 and 39). The two available are a 300cm^{-1} LiF_2 with diamond scatter and a 100cm^{-1} quartz with garnet filter. A balck polyethylene filter is located in the spectrometer where the light exits to the optical transfer box (Figure 21). Common to both systems is a flexible piece of
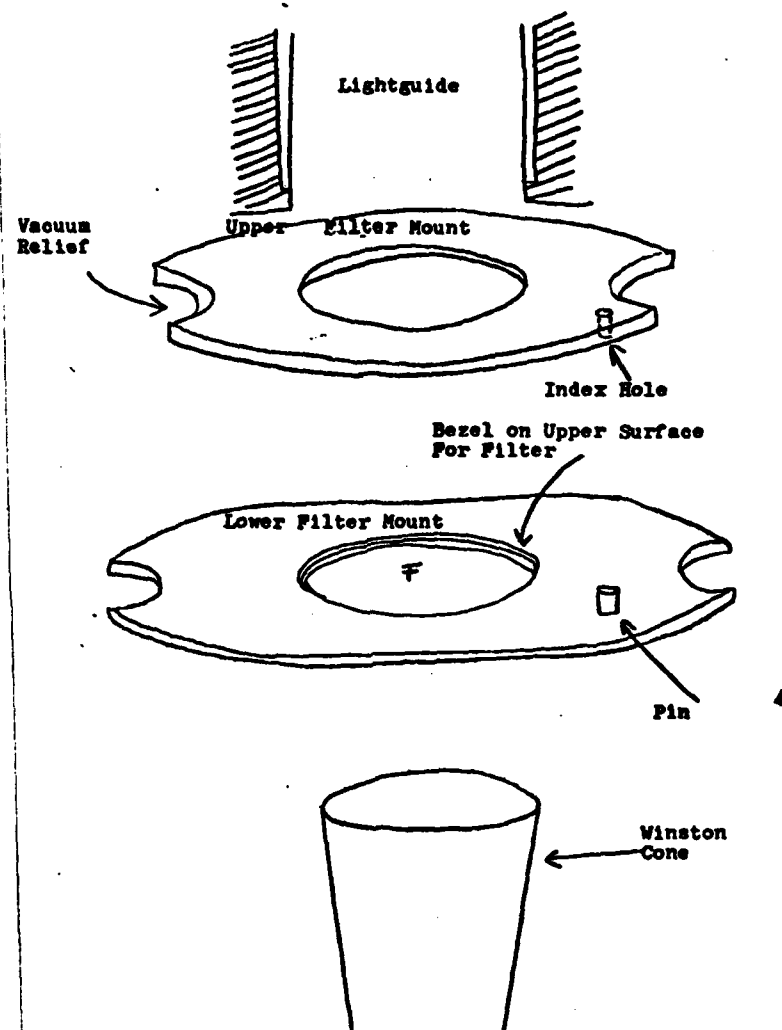
Fig. 39. 300 cm^{-1} or 100 cm^{-1} Filter Holder

79

white poly (Figure 21) which allows the vacuum in the light-guide to be separate from the optical box and spectrometer.

System Two. The system two sample chamber is shown in Figure 38. The sample is mounted on a flat cylindrical piece of OFHC copper with diluted G. E. varnish. The wires come off the sample and are wound around two copper posts used as thermal anchors. On the left post a thermister (T) is mounted with G. E. varnish. One of its wires is grounded to the bottom of the chamber (GND). Underneath the sample (SA) the load resistor (LR) is mounted with G. E. varnish. A black piece of cardboard (SH) shields the wire leads of the sample from the light to prevent heating. Four wires are then routed up a steel pipe to the preamplifier. The chamber is sealed with screws and an indium O-ring.

The two filters for this system are placed together and located as shown in Figure 21. One is quartz and the other is black polyethylene.

Computer System (29; 30)

The operation of the Nicolet 8000 Fourier Transform Spectrometer is controlled by a minicomputer. The minicomputer will run the spectrometer when it is in its RUN FTIR mode. In the RUN FTIR mode, all controlling of the spectrometer hardware, interferogram collecting and processing is done using three letter commands.

The basic commands are:

1. Data collection parameters
2. Data collection commands
3. Data manipulation commands and parameters
4. Display instructions
5. Plot instructions
6. Macro instructions

Some of the more commonly used software commands are listed in Appendix C.

Data Collection Parameters. These parameters are set before data collection is started. Doing a LST will place a list of data collection parameters on the screen. Some of the parameters will not be listed (e.g., MIR, NSS, APE) but must be set to what you want. A macro (see p. 82), SET, can also be used to set up collection parameters.

Data Collection Commands. After the data collection parameters have been set, the data collection commands are used to collect an interferogram (e.g., CLS) and do some processing of the data (e.g., FPS). Data collection is also accomplished by using the macro's BK1, BK2, COL.

Data Manipulation Parameters and Commands. These commands allow manipulation of the data and files containing the data.

Display Instructions. The screen display is manipulated by the display instructions.

Plot Instructions. Data from the screen can be plotted on graph paper. Plot instructions control how the

plot will be done.   The simplest way to plot is to use a single spectrum plot macro (PLT) or a two spectrum plot macro (OLR).

Macro Instructions.   A macro is a program where a number of three letter commands are strung together.   The macro instructions along with other three letter commands are used to create macros.

V. Experimental Procedure

This section explains the procedures for setting up the photoconductivity experiment and collecting the spectrum.

Sample Preparation and Mounting

After the samples were selected, most already had indium contacts annealed on at $450^{\circ}C$. Hall measurements had been performed and the results are listed in Table IV.

The sample is cleaned using solutions of water and soap, trichloroethylene, methanol, acetone and then nitrogen gas to dry the sample. The sample is then mounted onto a OHFC copper mount with diluted G. E. varnish.

For system two, after the initial wiring beneath the sample of the load resistor, thermister and sample wires, the sample wires are indium soldered to opposite ends of the crystal using a microscope and small soldering iron. It is important that indium not flow over the sides of the crystal and make electrical contact with the copper. The gold sample wires are insulated from the copper, when passing through the holes in the copper mounting plate, using heat shrink in the holes. The sample can later be removed using acetone to dissolve the G. E. varnish. The black cardboard is put in position (SH in Figure 38). The sample chamber is then sealed with an indium O-ring which is crushed when the sample chamber is bolted to the rest of the lightguide. The

Table IV
Hall Measurements

Sample	Number	Temp($^\circ$K)	Thickness(μ)	Rho(ohm-cm)	Mu(cm^2/v-sec)	Conc(cm^3)
1	HPC10-5-4	77 296	47	.34 5.7	1.5E5 6.5E3	1.25E14 1.6E14
2	HPC18-1-10	77 296	90	.28 4.7	1.4E5 7.7E3	1.6E14 1.7E14
3	HPC19-1-12	77 296	80	.059 .45	6.5E4 7.3E3	1.7E15 1.9E15
4	HPC19A-2-9	77 296	21	.15 2.6	1.3E5 6.2E3	3.3E14 3.8E14
5	Motorola 1	296	20	.17	6.5E3	5.5E13

84

filters (black poly and quartz) are left in position but the bolts are rechecked to make sure they are tight after being temperature cycled.

After the sample was mounted and the sample chamber sealed, all resistances (R_L-G_S, R_L-R_S, R_S-G_S, thermister) are checked and recorded. It is important that electrical connections be checked now, after the sample chamber and lightguide are placed in the magnet chamber and sealed off, after the liquid nitrogen is used to precool the system, before the liquid helium transfer and during helium transfer, for possible shorts.

The lightguide is placed in position so the sample chamber is in the center of the magnet. A seven prong male plug at the top of the steep pipe containing the sample chamber's wires is connected to the female plug which is wired to the preamplifier. The magnet is then lowered into its dewar and the top bolted shut.

For system one, after the teflon coated wires have been soldered to the mounted sample, they are routed through two holes in the Winston cone base. The Winston cone is then screwed onto the copper sample mount. The sample wires are soldered to the standoffs.

A $300 cm^{-1}$ filter is put in its mount (Figure 39) and placed in position in the sample chamber. The sample mount and Winston cone are screwed onto the bottom copper piece.

The bottom piece is then bolted on and the chamber sealed with a crushed indium O-ring.

Electrical measurements are made the same as for system two. The lightguide and sample compartment are placed in the center bore of the magnet dewar and sealed with a rubber O-ring and clamp.

The rest of the lightguide used in both systems is reassembled.

Magnet Preparation and Cooling

This operation is similar for both systems. After the lightguide is reassembled, it is leak checked using a helium gas leak detector.

The two vacuum chambers, in both dewars, are pumped using portable mechanical/diffusion pumps. The lightguide is also pumped using the portable vacuum pumps. The spectrometer and optical box are pumped with a mechanical pump to a pressure of 16 torr. The vacuum pumping is done the day prior to the photoconductivity run.

After the pumping is complete, the magnet is precooled with liquid nitrogen. During the precool and also during liquid helium transfer, the temperature is monitored by measuring the resistance of a thermister or germanium thermometer (depending on the system) and the sample resistance by a multimeter. Prior to filling the nitrogen chamber with liquid nitrogen, the inner helium chamber containing the magnet, is flushed with nitrogen gas and helium gas to

86

remove water vapor that would freeze when cooled and possibly prevent liquid helium collection or damage the magnet. The outer nitrogen chamber is now filled with liquid nitrogen and then the helium chamber is also filled with liquid nitrogen.

The system is left filled with liquid nitrogen overnight. In the morning, the outer nitrogen chamber is topped off. Nitrogen gas is then used to pressure the nitrogen liquid from the inner helium chamber. After all the liquid nitrogen is removed, helium gas is used to pressure out the remaining nitrogen gas. If all the nitrogen is not removed, it will freeze and may prevent liquid helium from collecting. When that happens, the temperature of the system will not drop below $40^{\circ}K$.

Next, the helium transfer begins. System one requires approximately 150 liters of liquid helium while system two requires approximately 300 liters to run the experiment. Transfer was accomplished using a cylinder of helium gas pressuring liquid helium from a 36 or 100 liter dewar. For system two, the helium dewar was left in place next to the magnet for a continuous transfer to keep the liquid level above the magnet.

Current-Voltage Curves

After the helium level is above the magnet and the sample temperature has stabilized below $5^{\circ}K$, the I-V characteristics of the sample are measured.

87

The I-V of the sample is measured by putting the sample in series with a 18.97 MΩ resistor and biasing them with two D.C. power supplies connected in series. The current and voltage is determined by

$$I = (V_b - V_s)/RL \qquad (33)$$

$$RS = V_s RL/(V_b - V_s) \qquad (34)$$

$$V_s = I \, RS \qquad (35)$$

where

V_b = bias voltage

V_s = sample voltage

RL = load resistor resistance

RS = sample resistance

Spectrum Collection

The mercury arc is now fired with the spectrometer filled with nitrogen gas to prevent air discharges and the arc not lighting. The spectrometer's electronics and the computer are turned off while lighting the arc since the high voltage surge may damage these systems.

The preamplifier switches for the input, DC bias, and amplifier power are turned on while the output is connected to the spectrometer. The spectrometer parameters are set using the SET command (Appendix C). The optimum parameters for a high resolution scan are in Table VII. The

88

spectrum is collected using a ISO macro (Appendix C). The time of collection will depend on how much signal averaging is necessary. The s..ctrum is taken at zero field and was attempted with a magnetic field. The magnetic field is ramped to the desired value using recommended currents and times (Appendix C, equipment chapter). The magnetic field is measured using magneto-resistive coils (equipment chapter).

After collecting the spectrum, it is placed on the directory disk using the PDS command (Appendix C). The sample file is then Fourier processed and displayed on the monitor. A plot of the spectrum is made using the PLT command (Appendix C).

VI. Results and Discussion

From research and discussion with other knowledgeable individuals, this may be the first attempt to run this experiment using a rapid-scan Fourier transform spectrometer. It was also the first time the magnet systems and lightguide were used for photoconductivity. The spectrometer had not been used in the far-infrared region of $0\text{-}120\text{cm}^{-1}$. For these reasons, new equipment had to be built, systems redesigned and modified, and basic information had to be obtained about filters, samples, load resistors, computer parameters, noise, etc. The results of this basic information is presented along with two zero field spectra. A discussion is presented of why a spectrum with a magnetic field was not obtained.

Hall Measurements

The vpe samples used are from the Avionics Laboratory and one (Motorola 1) was obtained from Dr. Stillman at the University of Illinois. Hall measurements, done by Dr. David Look, are listed in Table IV.

The samples were chosen for their high mobility at liquid nitrogen temperature so the sample will have sufficient mobility at $4.2^{\circ}K$ to obtain a signal. Their impurity concentrations had to be 10^{15}cm^{-3} or less or their wave functions would overlap and mask the donor peaks in a magnetic

field. Sample one and five are good to use as references.
Sample one is from the same crystal as a sample whose
spectrum was published by Button and Afsar. Sample five has
a very low donor concentration and high mobility and is used
as a reference by Stillman (25; 26).

Load Resistors

Carbon and ceramic resistors change resistance with
temperature and a carbon load resistor was placed near the
sample. This location precludes easily changing the
resistor. Since the optimum bias current for the system is
approximately 1μ amp (Figures 7 and 47) and there is a
limited range of battery voltages (batteries being used for
their low noise compared to a DC power supply) it is neces-
sary to know the resistance of the load resistor to bias the
sample with the correct current. A liquid helium resistance
of approximately $20M\Omega$ will give a suitable bias current with
a 22 volt battery.

A small glass dewar with an outer liquid nitrogen
jacket and a center liquid helium chamber was used to test
the resistors at $4.2^{O}K$. The resistor was attached to the
end of a metal probe and the resistance was measured using
a digital multimeter. A list of the resistors tested are in
Table V. The results show that knowing the room temperature
resistance does not guarantee knowledge of the resistance
at lower temperatures. All the resistances increase from

91

Table V
Temperature Dependence of Resistors

Resistor	Type	296 °K Resis.	77 °K Resis.	4.2 °K Resis.
1	Ceramic	9.15E6 Ω	>15E6 Ω	
2	Ceramic	1.02E6	1.23E6	2.29E6 Ω
3	Carbon	4.79E6	10.78E6	
4	Carbon	4.84E6	10.85E6	>20E6
5	Carbon	109.3E3	.22E6	862E6
6	Carbon	98.6E3	114.6E3	
7	Carbon	4.81E6	10.84E6	
8	Carbon	1.02E3	1.41E3	.036E6
9	Carbon	19.4E3	32E3	7.83E6
10	Carbon	34.1E3	49.8E3	3.71E6
11	Carbon	75E3	118.4E3	18E6
12	Carbon	103.5E3	150.6E3	10E6
13	Carbon	171.1E3	356E3	45E6
14	Carbon	125.2E3	217E3	5.5E6
15	Carbon	174E3	357E3	41E6

Table VI
Multimeter Bias Currents

Keithley 191		Systron 7205	
Scale (Ω)	Max. Current	Scale (Ω)	Max. Current
20M	.4 μa	10M	1 μa
2000K	4 μa	1000	1 μa
200K	40 μa	100	10 μa
20K	400 μa	10	99.6 μa
2K	4 ma	1	.999 ma
200	4 ma	.1	.999 ma

their room temperature value and the greatest increase is when $4.2^{O}K$ is approached. Resistor 11 was used to bias the sample for the photoconductivity experiment.

Filter Responses

In order to prevent higher energy radiation from exciting deep centers, donor electrons, and band to band, which would contribute to the conductivity and overwhelm the signal, a number of low pass optical filters were used in both systems. To determine the transmission of the filters, they were placed at the SB position of the spectrometer (Figure 22) and the spectrum was measured using a TGS or bolometer detector. The filter responses in the Figures 40 through 44 are relative and not normalized to a common number.

The $300cm^{-1}$, $100cm^{-1}$, and blackpoly filters are used in system one. The blackpoly filter (Figure 42) filters out most of the higher energy radiation. A choice can be made between the $300cm^{-1}$ and $100cm^{-1}$ filter (Figures 40 and 41). The $100cm^{-1}$ filter will limit radiation only to the region of interest ($20-100cm^{-1}$) but it also cuts out a great amount of radiation in the region of interest compared to the $300cm^{-1}$ filter. It is, therefore, desirable to use the $300cm^{-1}$ filter rather than the $100cm^{-1}$ filter.

System two uses a blackpoly filter (Figure 42) and quartz filter (Figure 43). The response of the combination

93
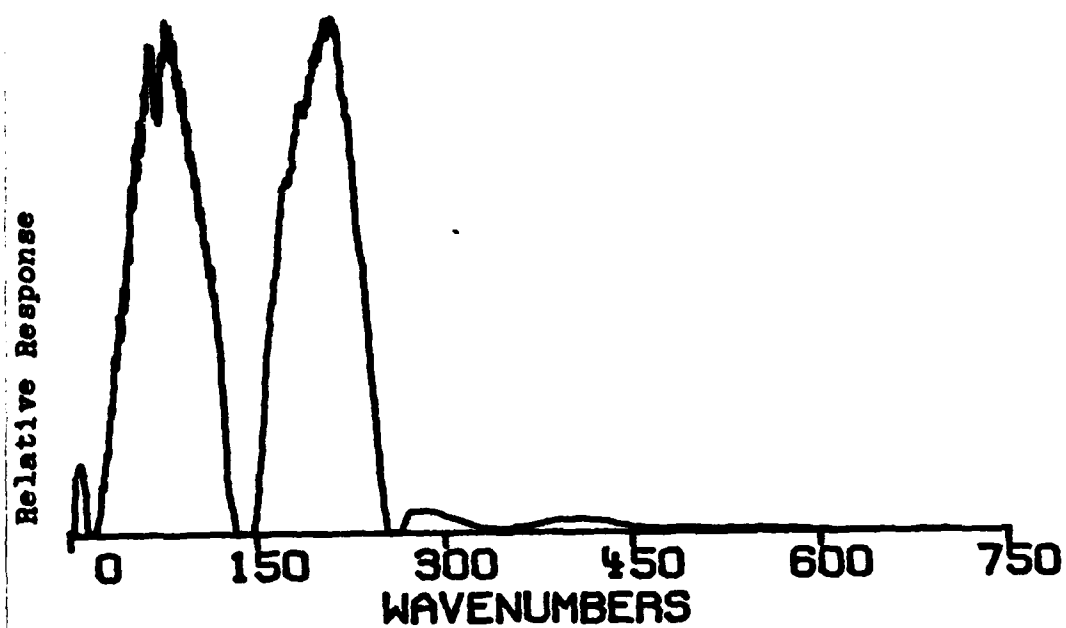
Fig. 40. 300 cm^{-1} Filter
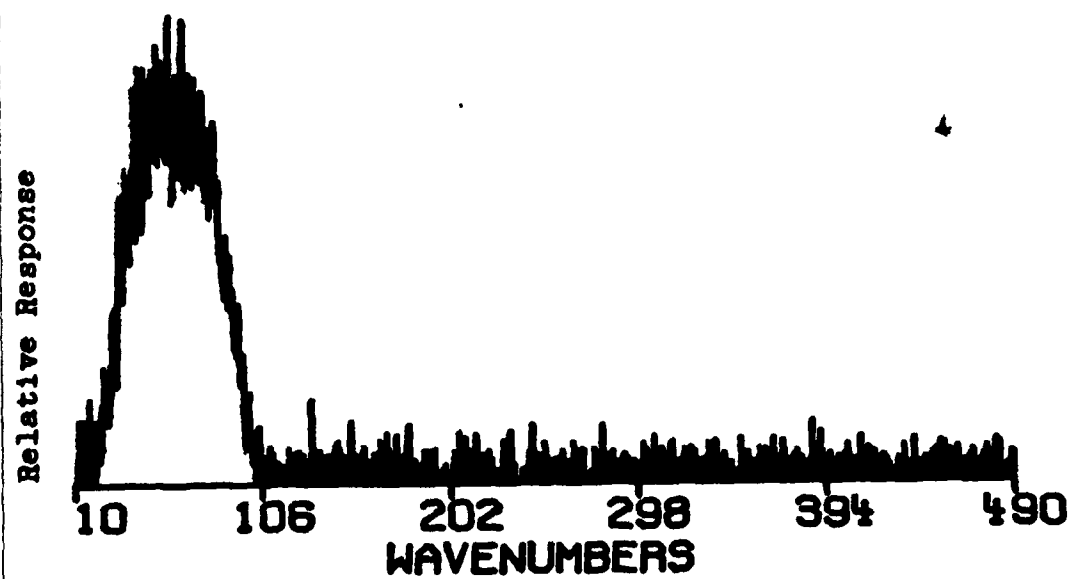
Fig. 41. 100 cm^{-1} Filter

94
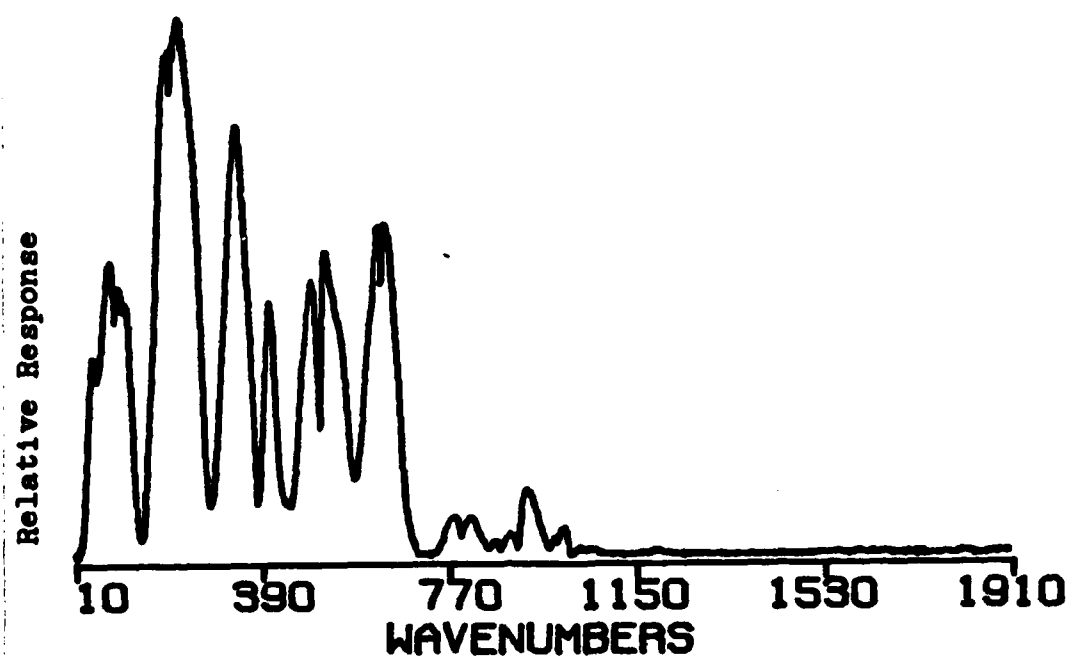
Fig.42. Black Polyethylene Filter
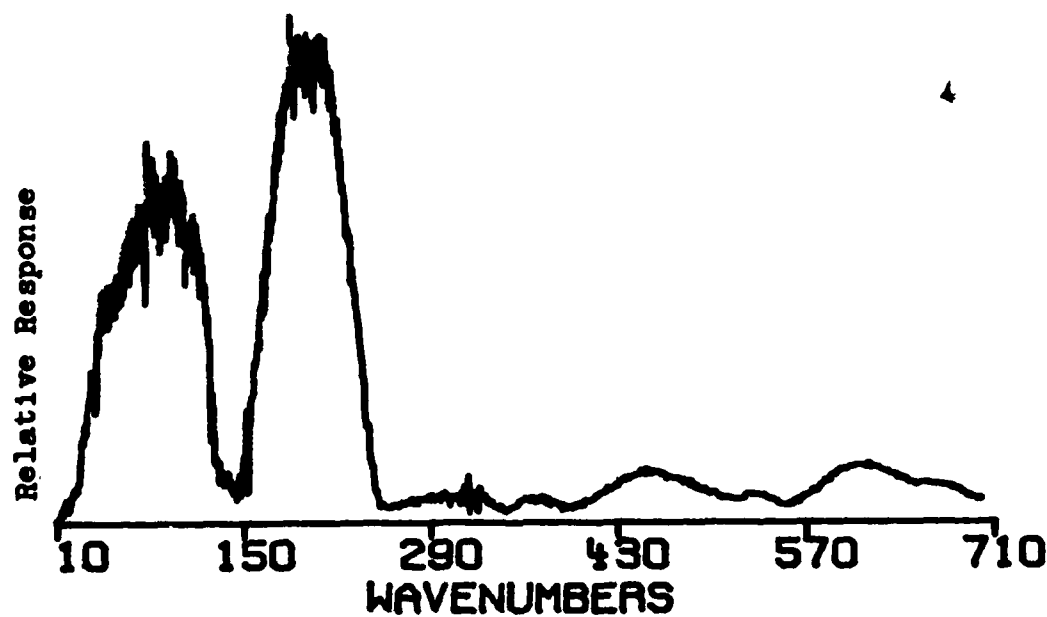
Fig.43. Quartz Filter
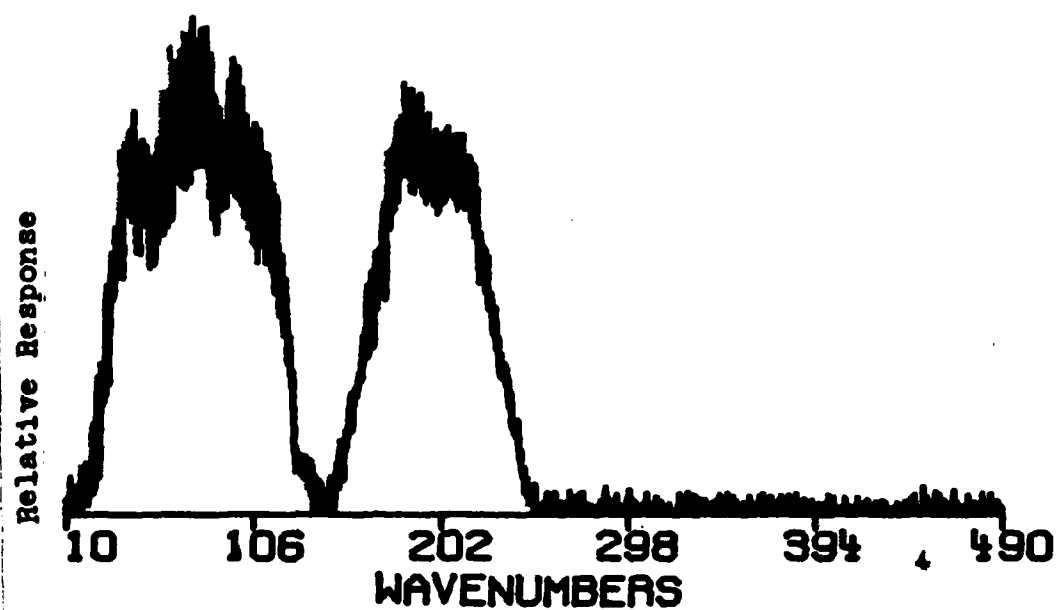
Fig.44. Black Polyethylene and Quartz Filters

of the two filters (Figure 44) is similar to the 300cm^{-1} filter and blackpoly.

Resistance Versus Temperature

The resistance versus temperature of sample HPC10-5-4 was measured while cooling the system (Figure 45). The reasons for the resistance change is explained in the theory. The resistance was read off a multimeter except the highest resistance value which was determined from an I-V curve. The temperature was measured by a thermister ($\pm 2^{\circ}$K). The resistances are ± 10 ohms except when the temperature is low (approximately 10°K or less). In this region, demonstrated by the sample's I-V characteristics, the resistance of the sample has a strong dependence on the bias current. Using different multimeters and scales on the meter will give different values of resistance at low temperature. The bias current versus resistance scale of two multimeters is listed in Table VI. When a sample is at 4.2°K, changing scales will change the resistance reading of the sample on the multimeter.

Collection Parameters

The parameters used for a high resolution scan ($.05 \text{cm}^{-1}$) are listed in Table VII.

The HPS and LPS filter settings were determined by measuring the mercury arc or globar spectrum with a helium cooled bolometer while the HPS and LPS settings were varied.

97

Resistance (Ω)

10^7

10^6

10^5

10^4

10^3

10^2

10^0 $\quad\quad$ 10^1 $\quad\quad$ 10^2 $\quad\quad$ 10^3

Temperature ($^\circ$K)

4
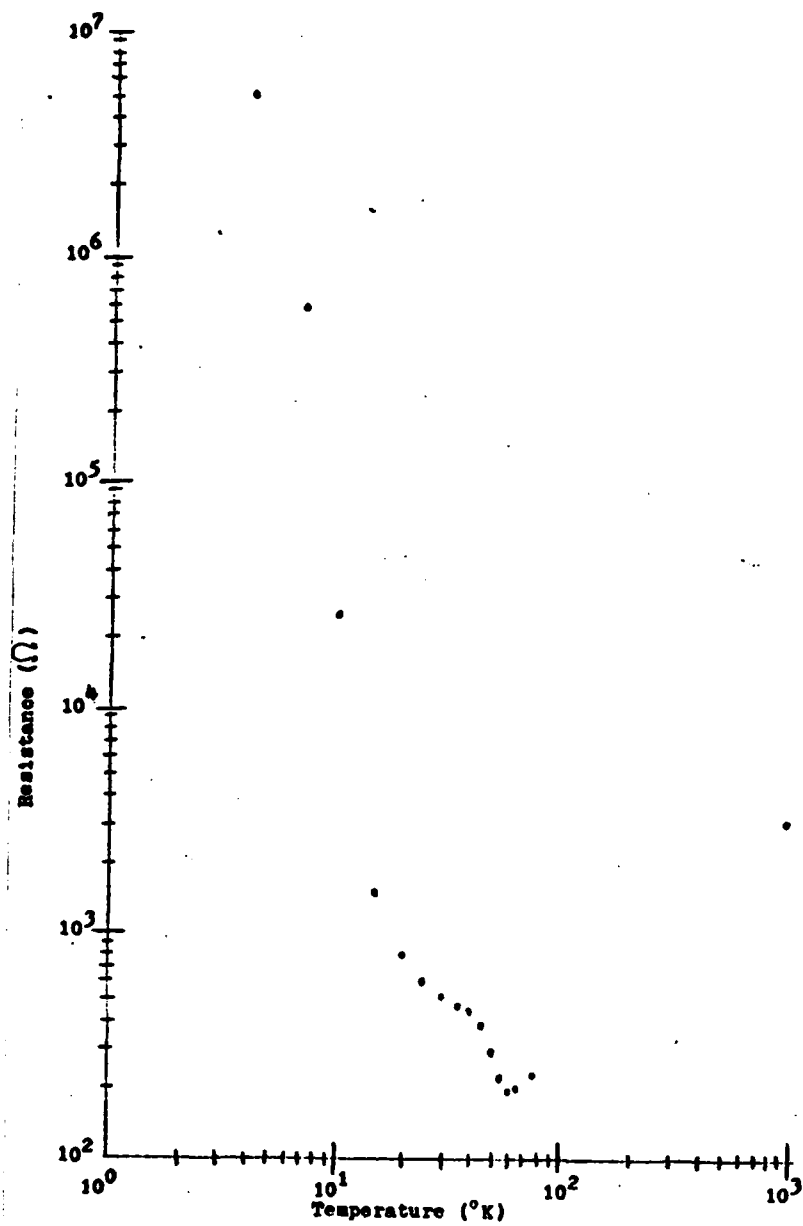
Fig. 45. Resistance versus Temp
for HPC10-5-4

Table VII
Optimum Parameters For High Resolution Scan

VEL =	35
SSP =	32
NDP =	17408
NTP =	32768
HPS =	0
LPS =	3
DET =	2
SRC =	2
NSK =	0
APN =	HG
APE =	.04

A HPS setting other than zero will cut out radiation in the desired wavelength region. The best LPS setting was 3. The best source was the mercury arc.

The VEL and APE settings were also varied to find the best response. It was first done with a TGS detector and then with the GaAs sample as the detector. The optimum values were 35 and .04 respectively. NDP=17408 were the most data points that could be taken, with a SSP of 32, in one scan. This gave a resolution of .05cm^{-1} (see Theory).

Current-Voltage Curves

While trying to run photoconductivity spectra, it was found that the temperature of the sample was critical. If the sample temperature was greater than 5.5^{O}K (Theory), the signal will be lost. It was determined that, although a temperature sensor was near the sample, the sample temperature could be very different than the sensor reading because of differences in heat conduction of the semi-insulating layer and sample wires. The difference was even greater when a joint separated the sample and sensor. Therefore, it was necessary to determine the I-V characteristics of the sample at liquid helium temperature as a means to determine if the sample was reaching a temperature of 4.2^{O}K in the sample chamber.

The same experimental arrangement used with the carbon resistor resistance measurements was used. The I-V

curves of three samples (Figures 46 through 48) are shown.
Two of the samples (Figures 46 and 47) have I-V curves
similar to Stillman's measurements (Figure 7). The other
sample (Figure 48) never reaches the impact ionization level
for the bias currents used. Where the curves bend over
(approximately 10^{-6} amps) is where the sample should be
biased for optimum photoconductive signal according to the
experimental work of Stillman (Figures 7 and 14). The two
curves for each sample (dark, background light) demonstrate
how radiation will ionize donors reducing the resistance of
the sample.

Zero Field Spectra

A zero field spectrum was never obtained using
system one before it broke. The dewar originally had five
openings to the center bore for optical studies. Five
stainless steel plugs were silver soldered to plug the five
holes in order to separate the center bore from the outer
vacuum chamber. This would allow the sample chamber to be
removed and another one put in without spoiling the outer
vacuum. This would also allow helium exchange gas to be put
in the center bore. The plugs continued to leak at different
locations after liquid helium was put in the dewar. It was
probably the heat of soldering and tilting the dewar on its
side that caused the joints which held the magnet in place
to break.
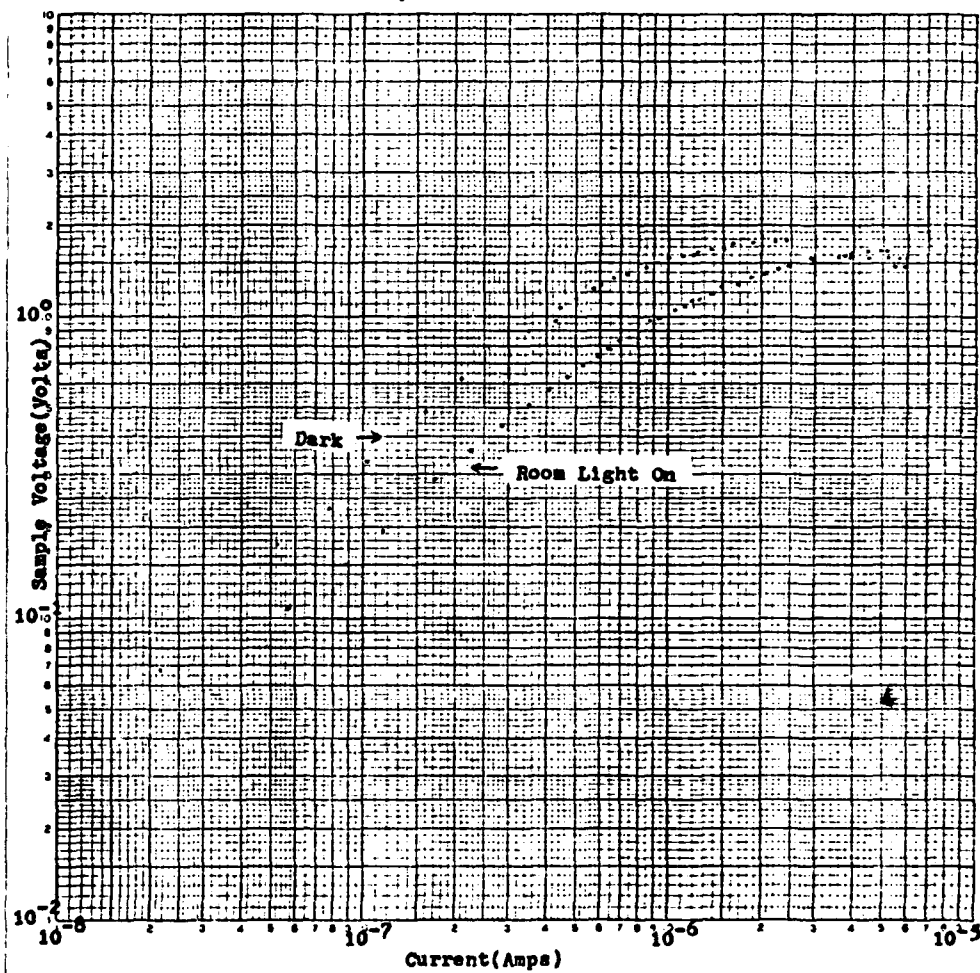
Fig. 46. Sample HPC18-1-10 at 4.2°K
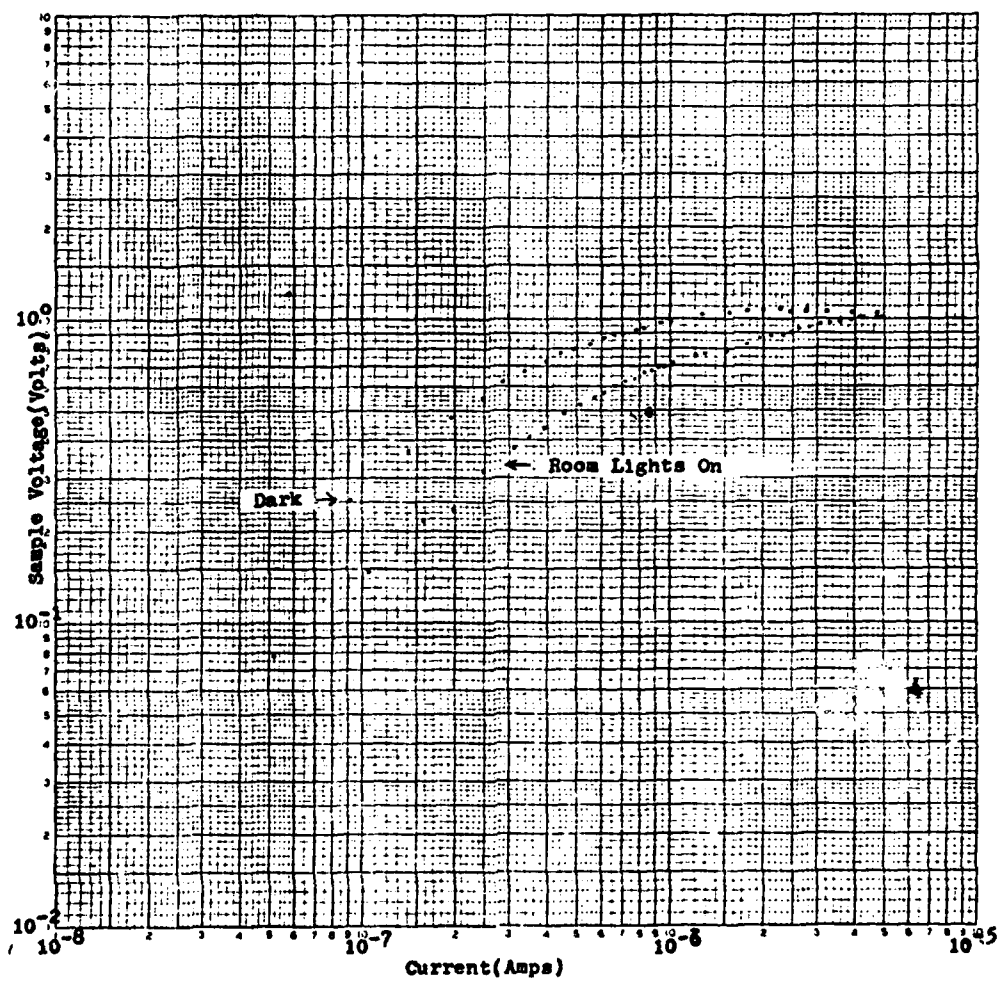
Fig. 47. Sample HPC10-5-4 at 4.2°K

103
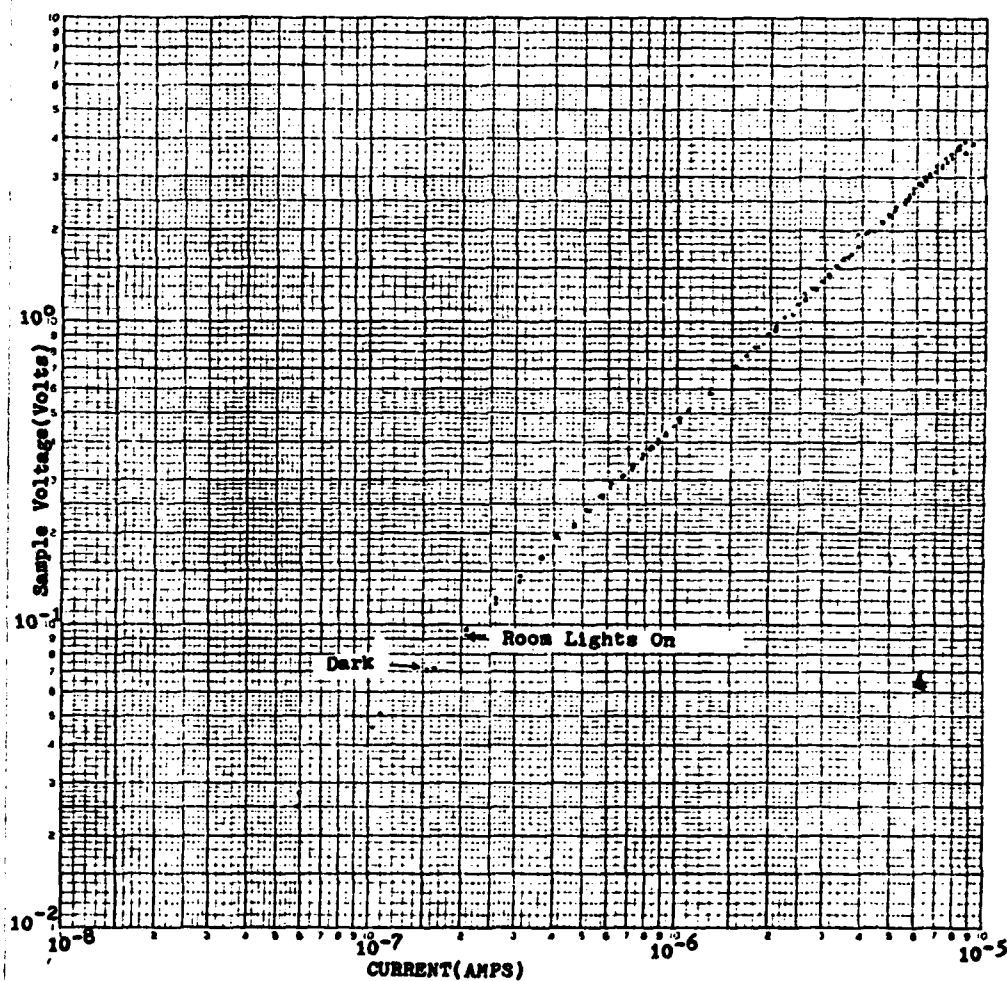
Fig.48. Sample HPC19-1-12 at 4.2°K

104

The main experimental problem with this system was temperature control. The sample chamber is not in direct contact with liquid helium. The sample chamber makes contact with the stainless steel of the center bore which is in contact with the stainless steel of the center bore which is in contact with liquid helium. This arrangement made for erratic temperature control of the sample and the sample never reached 4.2^OK. Some copper flanges were placed on the bottom of the sample chamber, copper sheets were placed at locations along the lightguide leading to the sample chamber, and copper mesh was placed above the sample chamber, to get better thermal contact. This arrangement was never tried since the joints holding the magnet broke.

System two was set up to run the experiment. Since the sample chamber was in direct contact with liquid helium the sample reached 4.2^OK. This system, however, is very inefficient in its liquid helium usage and must be warmed and the magnet lifted out to change samples. The more efficient system is number one but system two was used to demonstrate the feasibility of the experiment.

The first zero field spectrum is shown in Figure 49. The spectrum shows good S/N but to have obtained any signal at all, the preamplifier had to be directly grounded to the spectrometer with a metal strap. There are two features worth noting in the spectrum.
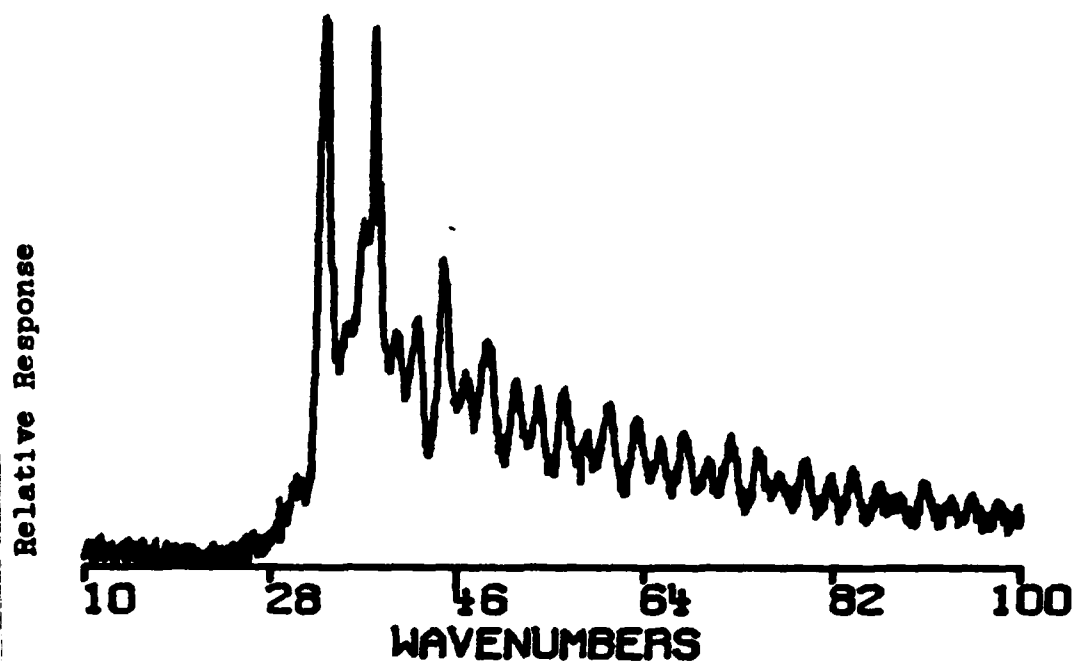
Fig. 49. HPC10-5-4 in Zero Field (First Try)
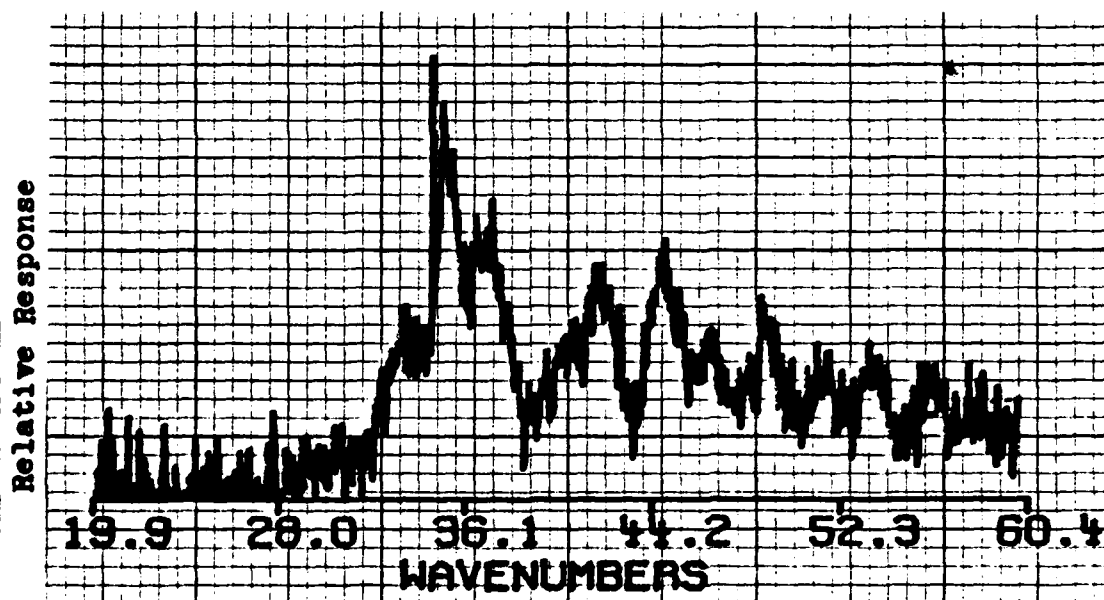
Fig. 50. HPC10-5-4 in Zero Field (Second Try)

106

There are two distinct peaks at 33.3cm^{-1} and 37.2cm^{-1}. The zero field spectrum should have a large peak at 35.5cm^{-1} and another smaller one at 42cm^{-1} (Figure 10). To have a peak at 33.3cm^{-1} and 37.2cm^{-1} would require a magnetic field (Figure 16). The field was on earlier but was off when the spectrum was taken. If there was a significant residual field, it was not measured since the magneto-resistive coils had a short on this run.

The second distinct feature are the peaks every 2cm^{-1} which decrease in magnitude as the signal decreases. They could be caused by multiple reflections from the quartz filter or the GaAs crystal. A comparison of the interference pattern of the incident radiation caused by the quartz crystal is shown in Figure 51 along with the photoconductivity spectrum. The 2cm^{-1} peaks of both spectra match very well. These same peaks occur in the second zero field spectrum (Figure 50). Background subtracting (BKS) and ratioing (RAS) of the quartz crystal spectrum with the photoconductivity spectrum was tried with unsuitable results. Straight line generating (SLG) of some possible interference interferograms produced little significant results. A calculation of where the interference interferogram of the 1mm quartz filter would occur, using the formula (29)

$$N = 2\text{nd} \ (15798)/SSP \qquad (36)$$
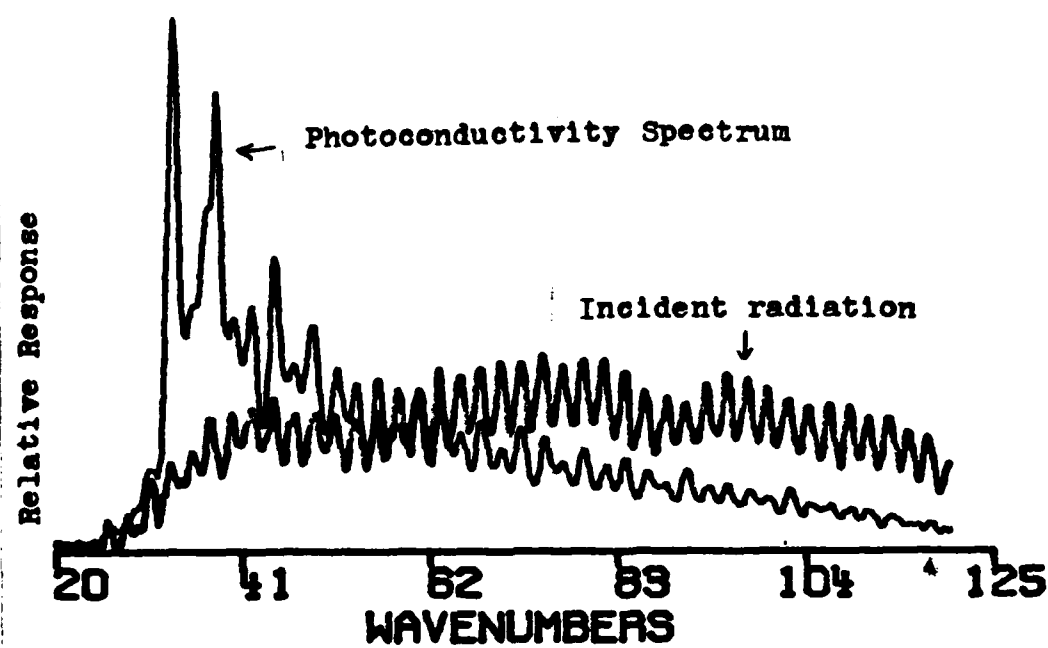
Fig. 51. HPC10-5-4 in Zero Field and the incident
radiation on the sample

where

$$15798 \text{cm}^{-1} = \text{laser frequency}$$

n = index of refraction

d = thickness

N = number of data points away from center burst of interferogram

gives 148 data points from the center burst. This is too close to the real interferogram to SLG without affecting the photoconductivity spectrum.

When the magnetic field was turned on the photoconductivity spectrum disappeared while the noise level increased. When the field was ramped down, the spectrum abruptly appeared after the charging current was zero for a short period of time. There are a number of suggested possibilities for this occurrence.

1. Some magnetic material in the sample chamber shorting the circuit when the field was on.

2. The current carrying wires shifting and shorting.

3. Magneto-resistive effects in the sample.

4. Magneto-resistive effects in the contacts or poor contacts.

5. The magnetic field affecting the resistor.

6. The changing magnetic field caused by fluctuations in the power supply producing noise especially in the coiled wires on the thermal anchor posts (Figure 38).

The following was done to eliminate some of these possibilities:

1. The sample chamber was checked for magnetic material and none was found.

2. The sample wiring and wiring in the chamber was redone and checked to be sure none would short. The thermister was placed in the bottom of the sample chamber to keep it and its wires away from the sample circuit's wires.

3. Magneto-resistive effects in the sample occur only at higher fields although Figure 8 shows some change in the sample's I-V curve for smaller fields. A low noise DC power supply was to be used to change the sample bias when the field was on to see if the signal would return. .

4. The indium contacts were resoldered and gold wires were soldered to the sample.

5. The resistor was placed in a two kG magnetic field at room temperature and it showed no shorting or change in resistance. It was put back in the sample chamber.

6. The coiled copper wires on the thermal anchor posts were removed. The gold sample wires were run along the thermal anchor posts but not coiled. G. E. varnish was placed on the posts to prevent the gold wires from contacting the copper.

7. The magnet was to be run in the persistent mode to see if this decreased the noise and allowed the signal to return.

8. The voltage across the sample and resistor was to be monitored to see how they changed with field.

The second zero field spectrum is shown in Figure 50 and a comparison of the two spectra is in Figure 52. The second spectrum shows a central peak at 35.4cm^{-1} which compares well with the 35.5cm^{-1} of Stillman's spectrum (Figure 10). Two suggested reasons why the peak is at 35.4cm^{-1} rather than two peaks at 33.3cm^{-1} and 37.2cm^{-1} are that the electrical circuit was affected by poor contacts or by the coiled copper wires on the thermal anchor posts. The spectrum had more noise than the first. The noise level was reduced slightly by grounding the preamplifier to the dewar.

Fig. 52. Comparison of Photoconductive Response of two spectra

HPC10-5-4,Zero Field (2nd try) GAN=32000

HPC10-5-4,Zero Field (1st try) GAN=3200

Relative Response

18.8 24.4 28.8 33.4 37.8 42.4 46.8 51.4 55.0 60.4

WAVENUMBERS
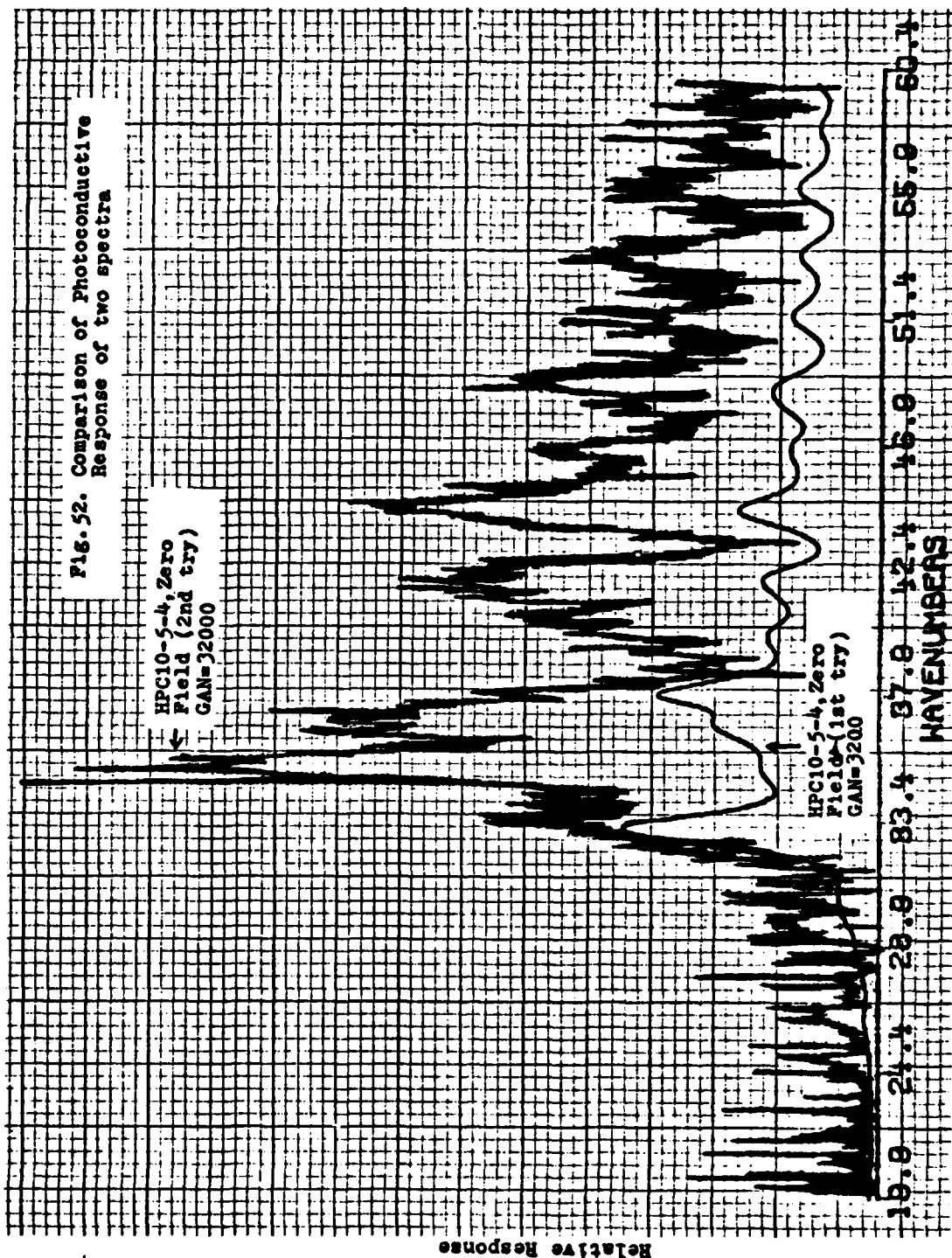
The output from the spectrometer was checked earlier for noise. It had more noise than when the first spectrum was taken for unknown reasons.

Before an experimental determination of why the noise level was so high or a long signal-averaged spectrum could be taken, the glass chamber holding the liquid helium cracked. The liquid helium and then the liquid nitrogen vaporized destroying the dewar and some other equipment.

Three of the samples (HPC10-5-4, HPC19-1-12, HPC18-1-10) were sent to Afsar and Button at MIT for analysis. They obtained no spectra on samples -12 and -10. They did obtain spectra on -4 up to 50kG. They found all the samples to have noisy contacts. They are re-annealing the contacts and will try the samples again.

4

VII. Suggestions and Recommendations

Obtaining the zero field spectrum demonstrates the feasibility of using the experimental arrangement with the rapid-scan Fourier transform spectrometer for obtaining photoconductivity spectra. The difference between the two spectra shows how sensitive the system is to changes in the experimental arrangement and how difficult it is to analyze what is happening to cause these changes.

The experiment has shown three areas that must be precisely controlled to get results: temperature, noise, optical alignment. The temperature of the sample must get below $5.5^{\circ}K$ to get a photoconductive signal. The optics must be aligned as precisely as possible to allow maximum radiation to reach the sample. This is important since the wavenumber region of interest ($0-120cm^{-1}$) is at the lower end of the mercury arc spectrum. It is easy for the noise to overwhelm the signal. The sample must be biased properly for the best signal to noise. The experimental arrangement having the load resistor at $4.2^{\circ}K$, and the circuit wiring being shielded and directly soldered into the preamplifier at the top of the magnet dewar eliminates as much noise as possible. It is also very important to have the preamplifier grounded properly to obtain a signal.

Why the signal disappeared when a magnetic field was applied, some changes and ways of troubleshooting the problem were discussed. System two can no longer be used and system one will be sent to the manufacturer to be fixed.

The following modifications to the system should be made:

1. The plugs to separate the inner bore from the outer bore should be taken out and properly installed by the manufacturer.

2. The inner bore should be flooded with liquid helium by drilling holes in the wall. This will allow the sample to reach $4.2^{O}K$.

3. A $300cm^{-1}$ filter which is wedged should be used to eliminate the interference spectra.

4. To reduce magneto-resistive effects at high fields the temperature of the sample is raised from $4.2^{O}K$ to a maximum of approximately $10^{O}K$. The sample holder already has a groove cut in the side for winding wire to use as a heater. To measure the temperature and control it at high fields a Lake Shore Cryotronics CS-400 capacitance temperature sensor and its associated electronics should be used.

5. If a more accurate measurement of the field is desired, a Hall probe can be installed near the sample.

6. The photoconductive circuit requires three wires and presently there are seven wires going to the sample chamber. Thus, there are only four wires to place a heater, temperature sensor, or Hall probe. Either more wires should be run to the sample chamber or a choice must be made as to what is placed in the sample chamber. There is also a limit to what is placed in the sample chamber since there is limited space there.

7. Another method of annealing contacts or a material for contacts other than indium may be needed if the contacts are noisy as the MIT researchers claim.

With these suggestions and recommendations, the experimental arrangement will provide a very useful means for

observing photoconductivity in a magnetic field. After the necessary modifications have been made, work should continue on locally grown vpe and mbe samples at the Avionics Laboratory. Back-doping experiments for donor identification should also be tried.

Bibliography

1. Afsar, M. N. and K. J. Button. "Reliable Far-Infrared Photoconductivity Method to Identify a Variety of Residual Donors in Epitaxial GaAs," International Journal of Infrared and Millimeter Waves, 1: 145-158 (1980).

2. -----. "High Intensity Magnetic Fields for the Identification and Study of Donors in Epitaxial GaAs," International Journal of Infrared and Millimeter Waves, 1: 513-524 (1980).

3. -----. "Ultimate Method for Unambiguous Identification of All Donors in Epitaxial GaAs and Related Compounds," International Journal of Infrared and Millimeter Waves, 2: 1113-1121 (1981).

4. Advanced Kinetics Inc. Instruction Manual, Infrared Lightguides Model MLG. Costa Mesa: Advanced Kinetics, Inc.

5. -----. Instruction Manual, Infrared Lightguides Model IRLG. Costa Mesa: Advanced Kinetics, Inc.

6. Armistead, C. J., R. A. Stradling, et al. "Identification of Contaminating Donors in III-V Compounds by Far-Infrared Laser Magneto-Optical Studies." To be published.

7. Bell, R. J. Introductory Fourier Transform Spectroscopy. New York: Academic Press, 1972.

8. Bosomworth, D. R., R. S. Crandall, and R. E. Enstrom. "Donor Spectroscopy in GaAs," Physics Letters, 28A: 320-321 (1968).

9. British Institute of Physics and the USAF Avionics Laboratory. Gallium Arsenide and Related Compounds: 1970. London: The Institute of Physics, 1971.

10. -----. Gallium Arsenide and Related Compounds: 1972. London: The Institute of Physics, 1973.

11. Brown F., A. Anderson, and P. A. Wolff. "High Power FIR Photoconductivity in n-GaAs," International Journal of Infrared and Millimeter Waves, 1: 277-284 (1980).

12. Bube, Richard C. *Photoconductivity of Solids*. New York: John Wiley and Sons, 1960.

13. Cohn, Daniel R. "Magneto-Optical Properties of Polarons," *MIT Ph.D. Thesis*, 1971.

14. Cooke, R. A., R. A. Hoult, R. F. Kirkman, and R. A. Stradling. "The Characterization of the Donors in GaAs Epitaxial Films by Far-Infrared Photoconductive Techniques," *Journal of Applied Physics*, 11: 945-953 (1978).

15. Covey, J. P., D. G. Mead and D. R. Mattson. *A High Resolution Fourier Transform Spectrometer*. Madison: Nicolet Instrument Corporation.

16. Davenport, Jr., Wilbur B. and William L. Root. *An Introduction to the Theory of Random Signals and Noise*. New York: McGraw-Hill, 1958.

17. Deaton, Terrence F. "Spin-Flip Raman Scattering in Cadmium Sulfide," *AFIT Masters Thesis*, 1973.

18. Dingle, R., C. Weisbuch, H. L. Stormer, H. Morkoc, and A. Y. Cho. "Characterization of High Purity GaAs Grown by Molecular Beam Epitaxy," *Applied Physics Letters*, 40: 507-510 (15 March 1982).

19. Foskett, C. T. "Noise and Finite Register Effects in Infrared Fourier Transform Spectroscopy," *Applied Spectroscopy*, 30: 531-539 (1976).

20. Institute of Physics and The Physical Society. *Gallium Arsenide; 1968 Symposium Proceedings*. London: Institute of Physics and the Physical Society, 1969.

21. Intermagnetics General Corporation. *Instruction Manual for Intermagnetics General Corporation Superconductive Magnets and Systems, SO-9123*. Guilderland: Intermagnetics General Corporation.

22. Kaplan, R., M. A. Kinch, and W. C. Scott. "Magnetic Field Effects on Hydrogenic Donor States in GaAs," *Solid State Communications*, 7: 883-886 (1969).

23. Larsen, D. M. "Inhomogeneous Line Broadening in Donor Magneto-Optical Spectra," *Physical Review B*, 8: 535-552 (15 July 1973).

24. Low, T. S., G. E. Stillman, A. Y. Cho, H. Morkoc, and A. R. Calawa. "Spectroscopy of Donors in High Purity GaAs Grown by Molecular Beam Epitaxy," *Applied Physics Letters*, 40: 611-613 (1 April 1982).

25. Low, T. S., G. E. Stillman, et al. "Photothermal Ionization Identification of Sulfur Donors in GaAs," *Applied Physics Letters*, 41: 183-185 (1982).

26. -----. "Spectroscopic Identification of Si Donors in GaAs," *Applied Physics Letters*, 40: 1034-1036 (1982).

27. Mattson, D. R. "Sensitivity of a Fourier Transform Infrared Spectrometer," *Applied Spectroscopy*, 32: 335-338 (1978).

28. Narita, S. and M. Miyao. "Shallow Donor States in High Purity GaAs in Magnetic Field," *Solid State Communications*, 9: 2161-2165 (1971).

29. Nicolet Instrument Corporation. *7199 FT-IR*. Madison: Nicolet Instrument Corporation, 1980.

30. Nicolet Analytical Instruments. *FT-IR Software Manual*. Madison: Nicolet Instrument Corporation, April 1981.

31. -----. *8000 High Vacuum Spectrometer System*. Madison: Nicolet Instrument Corporation, 1980.

32. Ozeki, M., et al. "Residual Donors in High Purity Gallium Arsenide Epitaxially Grown From Vapor Phase," *Japanese Journal of Applied Physics*, 16: 1617-1622 (1977).

33. Praddaude, H. C. "Energy levels of Hydrogenlike Atoms in a Magnetic Field," *Physical Review A*, 6: 1321-1324 (October 1972).

34. RCA. *Superconductive Magnet Type SM2829*. Harrison: RCA Superconductive Products, 1969.

35. Stillman, G. E., and C. M. Wolfe. "Electrical Characterization of Epitaxial Layers," *Thin Solid Films*, 31: 69-88 (1976).

36. -----, and J. O. Dimmock. "Detection and Generation of Far Infrared Radiation in High Purity Epitaxial GaAs," in *Submillimeter Waves*, edited by Jerome Fox, Brooklyn: Polytechnic Press, 1971.

37. -----. "Far-Infrared Photoconductivity in High Purity GaAs," in *Semiconductors and Semimetals*, Volume 12, edited by R. K. Willardson and A. C. Beer, New York: Academic Press, 1977.

118

38. -----. "Donor Magnetospectroscopy in High Purity Epitaxial GaAs," in Proceedings of the Third International Conference on Photoconductivity, edited by E. M. Pell, Oxford: Pergamon Press, 1971.

39. Stillman, G. E., D. M. Larson, and G. M. Wolfe. "Mass Anomaly in the Zeeman Effect of GaAs Donor 2p Levels," Physical Review Letters, 27: 989-992 (11 October 1971).

40. Smith, R. A. Semiconductors. Cambridge: Cambridge University Press, 1979.

41. Tannenwald, P. E., H. R. Fetterman, D. M. Larson, and G. E. Stillman. "Field-Dependent Central-Cell Corrections in GaAs by Laser Spectroscopy," Physical Review Letters, 26: 975-992 (19 April 1971).

42. The Institute of Physics. Gallium Arsenide and Related Compounds, 1974. London: The Institute of Physics, 1975.

43. Theis, William Dr.

44. Willardson and Beer, eds. Semiconductors and Semimetals, Volumn 1. New York: Academic Press, 1966.

45. -----. Semiconductors and Semimetals, Volumn 2. New York: Academic Press, 1966.

46. Wilson, A. H. The Theory of Metals. Cambridge: Cambridge University Press, 1953.

47. Wolfe, C. M., G. E. Stillman, and J. O. Dimmock. "Ionized Impurity Density in n-Type GaAs," Journal of Applied Physics, 41: 504-507 (1970).

48. Wolfe, C. M., G. E. Stillman, and D. M. Korn. "Residual Donors in High-Purity GaAs," in Gallium Arsenide and Related Compounds (St Louis), 1976, edited by L. F. Eastman, Bristol: The Institute of Physics, 1977.

49. Yafet, Y., R. W. Keyes and E. N. Adams. "Hydrogen Atom in a Strong Magnetic Field," J. Phys. Chem. Solids, 1: 137-142 (1956).

Appendix A

Superconducting Magnet Data

Figure 53 shows the recommended charging rate for the Intermagnetics magnet. The rate is controlled by settings on the power supply. Figure 54 shows the approximate field that is obtained when a certain current is flowed through the magnet. Figure 55 is the magnetic field versus resistance ratio (R_o=zero field resistance) of the magneto-resistive coils.

Figures 56 through 58 are for the RCA magnet. The first is similar to Figure 54 for the other magnet. Figures 57 and 58 show the magnetic field versus voltage of the magneto-resistive coils when a 50mA bias is applied from a constant current supply.
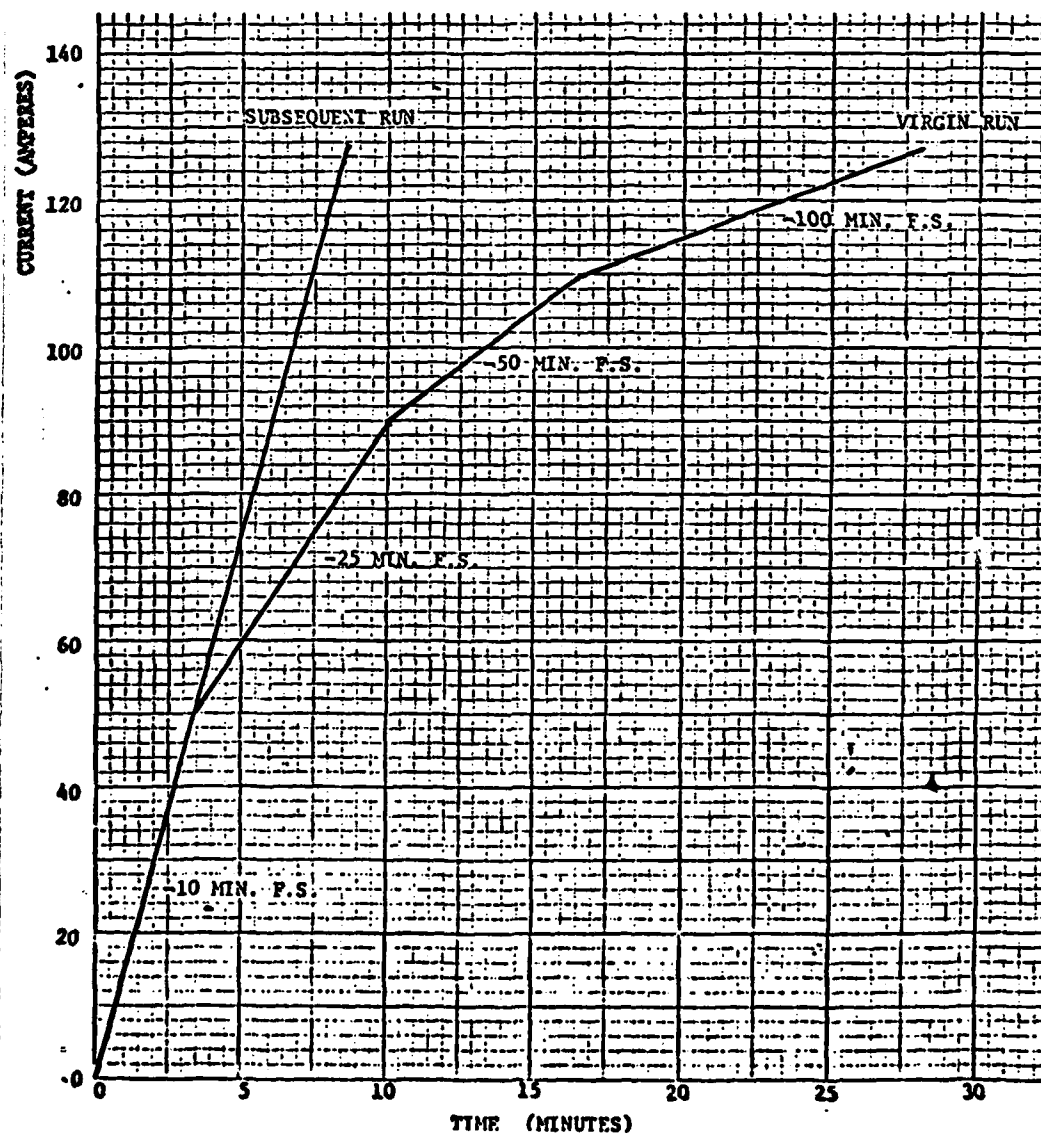
Fig.53.Recommended charge rate for Intermagnetics magnet (21)

121
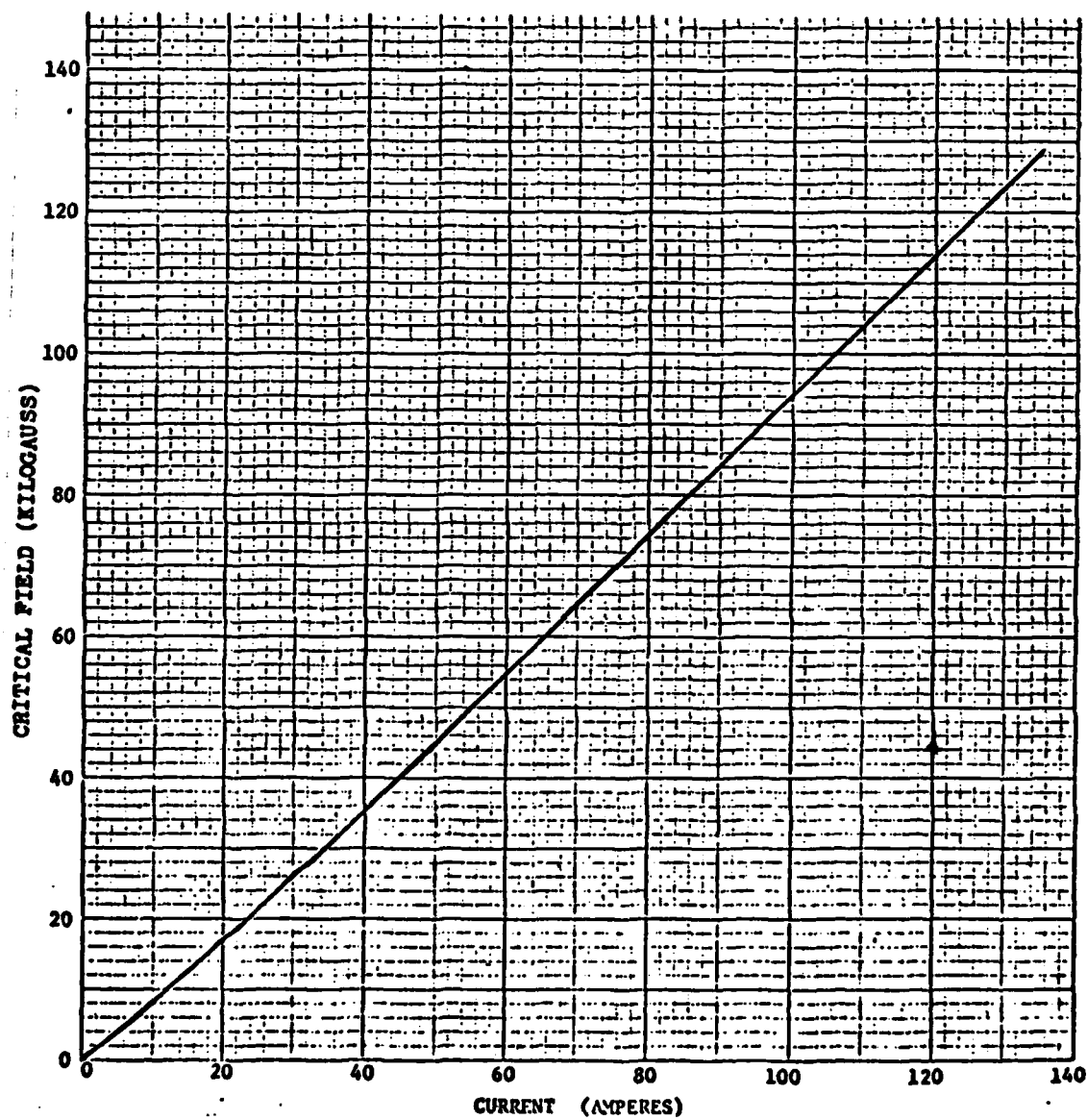
Fig. 54. Magnetic field versus current for Intermagnetics Magnet (21)

122
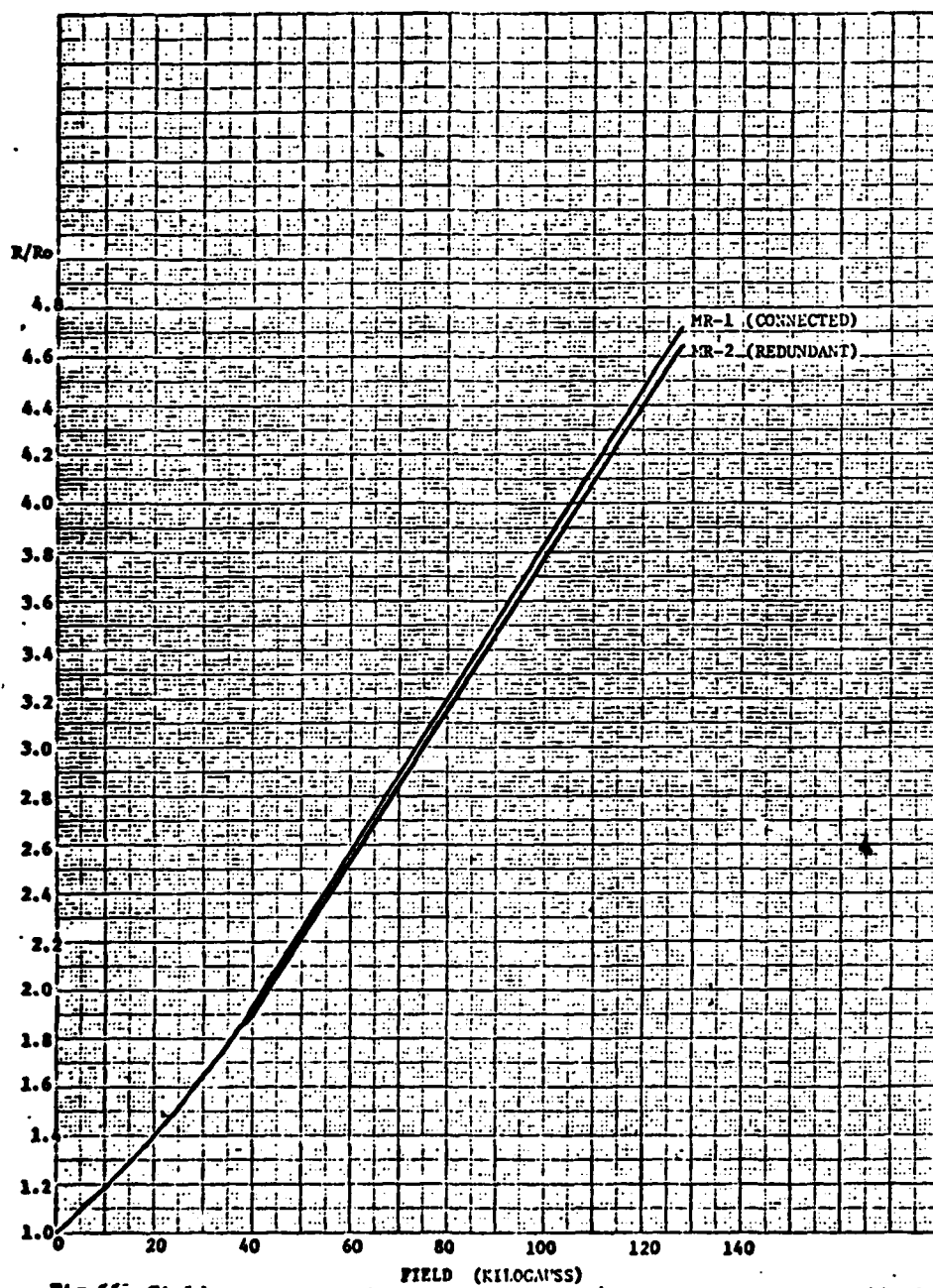
Fig.55. Field versus magneto-resistive ratio (Intermagnetics magnet)(21)
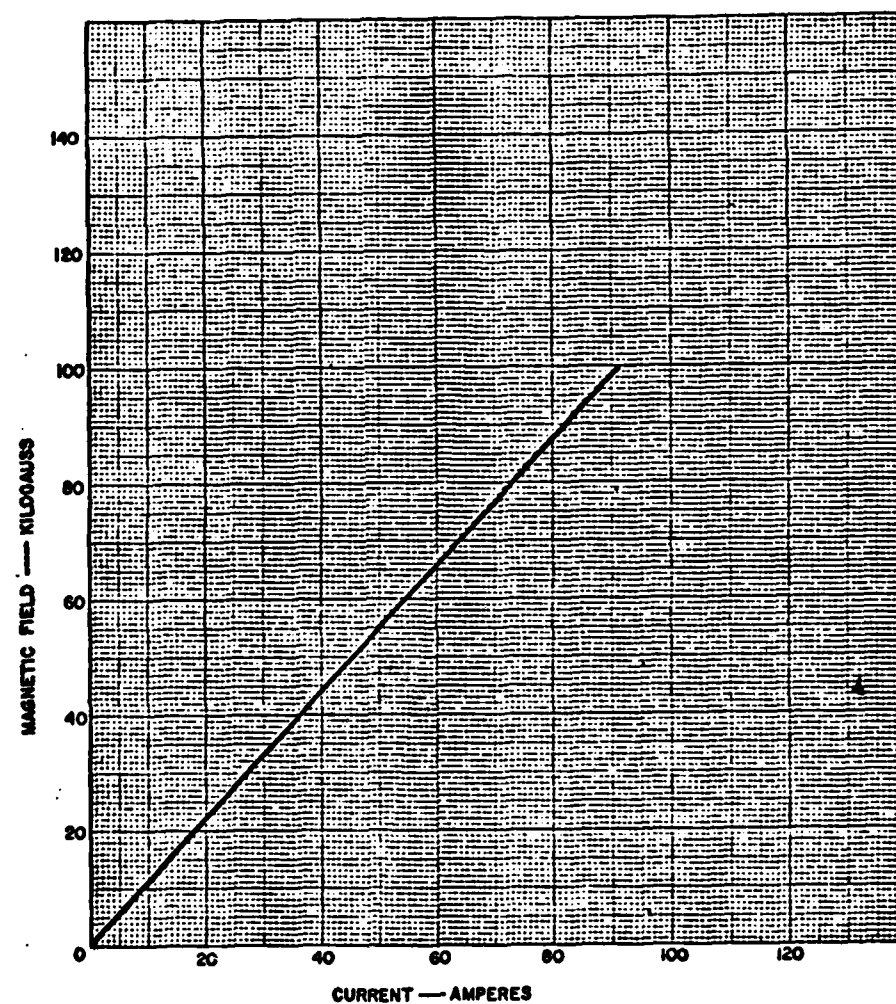
Fig. 56. Magnetic field density as a function of superconductive coil current for RCA magnet. (34)
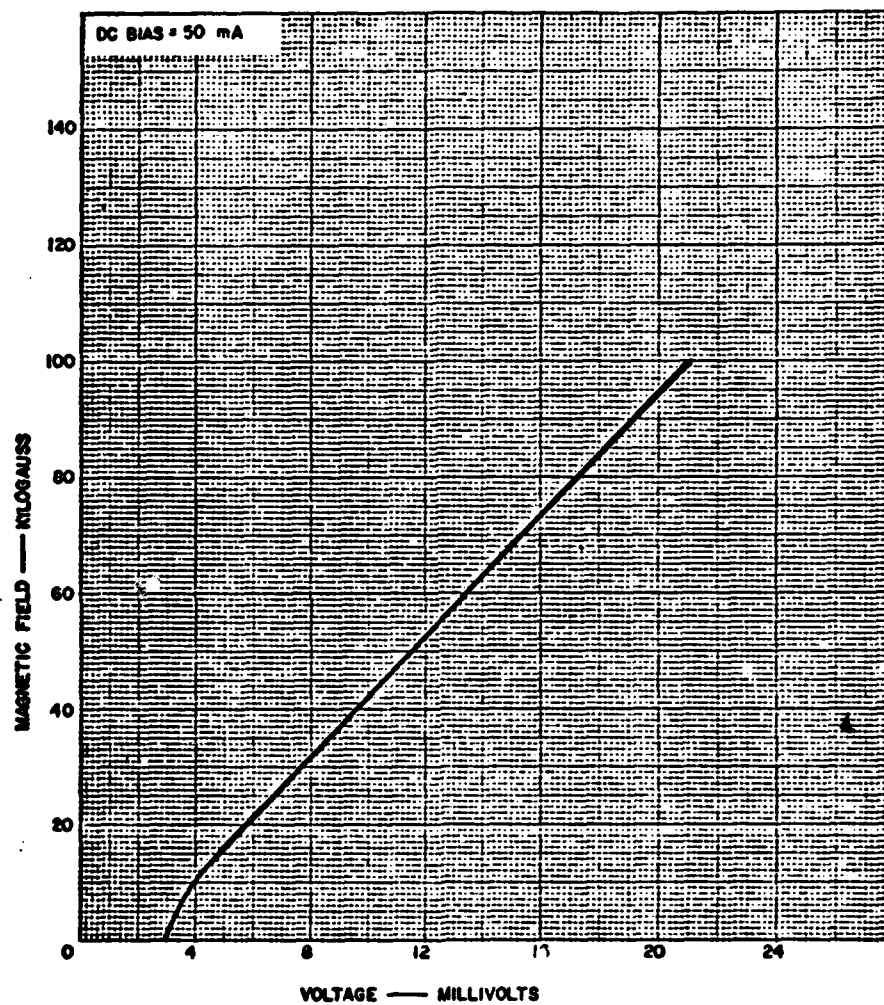
Fig. 57. Voltage output of magneto-resistive probe no. 1 as a function of magnetic field at center of magnet for RCA magnet. (34)

125
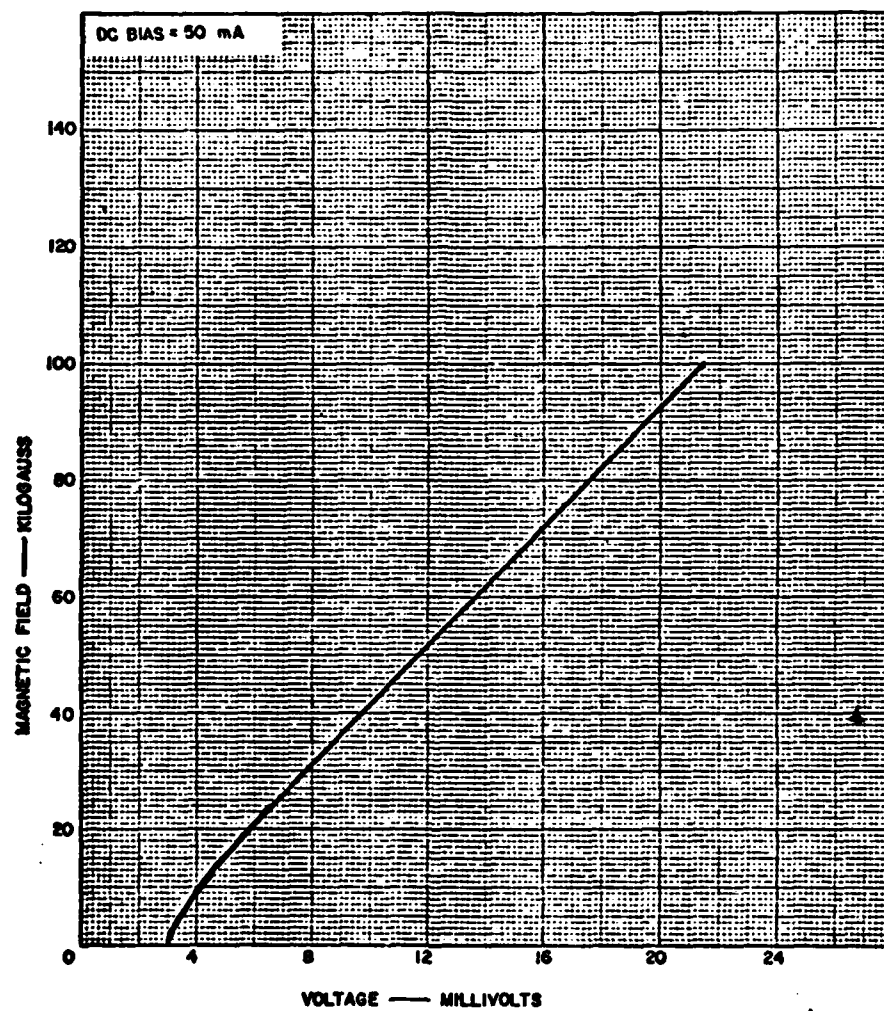
Fig. 58. Voltage output of magneto-resistive probe no. 2 as a function of magnetic field at center of magnet for RCA magnet. (34)

126

Appendix B

Preamplifier Circuit

Figure 59 shows the preamplifier circuit used in the LN-6 preamplifier used in the experiment.

Fig. 59. Infrared Laboratories LN-6 preamplifier circuit

R_L - SELECTED LOAD RESISTOR

R_S - sample

R_S - SELECTED RESISTOR
B2,B3 EVEREADY 146 X
B1 SELECTED BIAS BATTERY
Q,Q2 SELECTED 2N4867
OP AMP μL 776

128
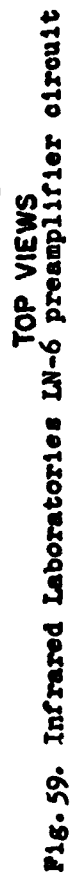
Appendix C

Software Instructions (30)

What follows are the software instructions used in the FTIR mode of the Nicolet 8000 spectrometer. Also listed are some of the macros (short programs) used on the mini-computer.

Data Collection Parameters

APE   Iris aperture control

BDL   Beam delay time

COR   Correlation function (NO, LO, IT, MD, HI)

DET   Detector select (1,2)

DSP   Display the interferogram during data collection (IG, NO)

FSZ   File size of data blocks on scratch disk (1408 to 360448)

GAN   Gain of the amplifier board (1,2,4,8,16,32,64,128)

HPS   High pass filter setting. Lower numbers select 3 dB roll-off

LPS   Loss pass filter setting. Higher numbers selects higher 3 dB roll-off (1,2,3,4,5,6,7)

MIR   Selects mirror positions for the sample bench, sample laser, GC bench or the GC laser (SB, SL, GB, GL)

NDP   Number of data points taken per scan (1024 to 262144)

NSx   Number of scans taken per data collect in the specified file (x=B,D,R,S)

NSK   Number of skipped points between white light and the start of data collection

NTP   Number of transform points (1024 to 524288)

SRC   Source select (1,2)

SSP   Sample spacing (1,2,4,8,16,32,64)

VEL   Velocity of mirror

Data Collection Commands

APx   Apodize the specified file (x=B,D,R,S)

CLx   Collect an interferogram into the specified file (x=B,D,R,S)

FPx   Phase calculate, apodize, Fourier transform (Cooley-Tukey algorithm) and phase correct an interferogram (x=B,D,R,S)

FTx   Fourier transform (Cooley-Tukey algorithm) the specified interferogram (x=B,D,R,S)

PCx   Phase calculate the specified interferogram (x=B,D,R,S)

PHx   Phase correct the interferogram after Fourier transformation (x=B,D,R,S)

RAx   Ratio the specified file to the background file then multiply times 100 (x=B,D,R,S)

Data Manipulation Parameters and Commands

ABx   Calculate absorbance from transmittance

AFN   Apodization functions (HG,TI,BX,TP,CS)

BKS   Subtract background file from sample file and store in sample file

BFN   Background file number (2 to highest file number)

CAD   Co-add the origin file into the destination file without scaling

CPY   Copy the entire monitor disk onto the scratch disk

DFN   Destination file number (2 to highest file number, based on FSZ)

130

GDx   Get data file from the monitor disk (x=B,D,R,S)

GPF   Get parameter file from monitor disk using a valid
      monitor name (ex. DPS41)

MBD   Move background file to destination file

MOx   Move the origin file to the specified file (x=B,D,R,S)

MRD   Move the reference file to the destination file

MSD   Move the sample file to the destination file

MTx   Print measurement time for specified file (x=B,D,R,S)

NPD   Number of data points used in phase calculation

NPT   Number of transform points used in phase calculation

OFN   Origin file number (2 to HFN, based on FSZ)

PAx   Reset parameters from specified file (x=B,D,R,S)

PDx   Put specified data file onto the monitor disk (x=B,D,
      R,S)

PFN   Parameter file number (0-63)

RFN   Reference file number (2 to HFN, based on FSZ)

RPF   Read parameter file from PFN

SFN   Sample file number (2 to HFN, based on FSZ)

STx   Print starting time of last data acquisition for the
      specified file (x=B,D,R,S)

SLG   Straight line generator for destination file

SPF   Store parameter file in the PFN

TIx   Print title of specified file (x=B,D,R,S)

TXx   Transform absorbance file back to transmittance

TXQ   Convert sample file to transmittance at a 200% scaling

131

Display Instructions

ASx   Autoscale YSP and YEP from XSP to XEP (x=B,D,R,S)

DSx   Display on scope the specified file (x=B,D,R,S)

XEP   X-axis end point

XSP   X-axis starting point

YEP   Y-axis end point

YSP   Y-axis starting point

Plot Instructions

PLx   Plot the specified file based on display parameters
      (x=B,D,R,S)

PAG   Go to new page after next plot (YS,NO)

PLO   Number of plotter steps above the lower limit switch
      to start plot

TIT   Yes or No for Nicolet 7199 FT-IR title on a plot

XSL   X-axis length in inches

YSL   Y-axis length in inches

XPN   X-axis pen movement in inches

YPN   Y-axis pen movement in inches

ZPN   Zero pen to reference y-axis

Macro Instructions

CRT xxx   Create a macro called xxx

Del xxx   Delete a macro called xxx

END   End a macro program

LST xxx   List to the printer the program xxx

LPF   List parameter file macro

FLS   List files macro

132

OMD	Output macro descriptor
MAC	Enter the macro processor-allows addition or deletion of macros
PAU	Pause and wait for a return
POF	Plotter off
PON	Plotter on
PRN xxx	Print the value of parameter xxx
RIR	Return to the FT-IR mode
SOF	Scope off indicates scope is no longer to be used as the macro print device
SON	Scope on indicates scope is to be used as the macro print device

MACROS (43)

Table VIII
LST-List parameters macro

```
:LST LST
SON
DFN=DFN
LPF
DFN=DFN
PRN XSL
PRN YSL
PRN XSP
PRN XEP
PRN FSZ
PRN NPD
PRN NPT
PRN COR
PRN PHZ
PRN SGH
PRN SGL
DFN=DFN
FLS
SOF
END
```

Table IX
OLR-Plot of two interferograms macro

```
:LST OLR
SON
OMD
ENTER RFN=FIRST FILE TO BE PLOTTED, DFN= 2ND
OMD
POSITION PEN AT BOTTOM OF PAGE
PRN XSL
PRN YSL
OMD
CHECK THAT XSL,YSL ARE CORRECT
SOF
RFN
DFN
AXS=NO
PAG=NO
PLO=100
ZPN
ASR
DSR
PAUPLOT? Y=RETURN ; N=CNTRL-8
PLR
AXS=YS
OMD
CHANGE PEN COLOR AND DO "PLT"
END
```

134

Table X
ISO-Macro used to collect high resolution interferograms

```
:LST ISO
OMD
ENTER NO. OF LOOPS
QIT
TEM=0
SFN
DFN
CLS
MSD
PRN SFN
STS
NSD=NSS
FOR III=1TILQIT
SFN=SFN+1
TEM=TEM+1
OFN=SFN
CLS
CAD
NSD=NSD+NSS
PRN SFN
STS
OMD
EARLY STOP? SET QIT=TEM
PRN TEM
NXT III
END
```

Table XI
SET-Set parameters and files macro

```
:LST SET
OMD
ENTER PARAMETER FILE NUMBER FOR RESOLUTION/DETECTOR DESIRED
PFN
RPF
PRN FSZ
LPF
TIT=NO
XPN=0.
YPN=0.
PLO=100.
SON
OMD
YOU MAY CHANGE THE FOLLOWING PARAMETER BY TYPING NEW VALUE,
OMD
THEN A RETURN--IF OK JUST RETURN
OMD
SUGGEST THAT NSB=NSS/2 IF T. 0 BACKGROUNDS WILL BE COLLECTED
SOF
NSS
NSB
GAN
SON
OMD
ENTER LAST FILE TO BE RETAINED FROM PREVIOUS DATA ON DISK
OMD
NEW DISK? TYPE DFN=2 HERE
SOF
DFN
DFN=DFN+1
RFN=DFN+1
SFN=DFN+2
OFN=RFN
BFN=2
LST
OMD
UNHAPPY WITH A PARAMETER? TYPE NAME,NEW VALUE,RETURN
OMD
REMEMBER TO SET THE APERTURE !!! 'APE'
END
```

Table XII
COL-Collect an interferogram macro

```
:LST COL
SON
OMD
PUT HELITRAN IN SAMPLE POSITION--PEAK UP WITH MICROMETERS,RETURN
OMD
GAN NOT HIGH ENOUGH? DO CNTRL-S, RESET GAN AND HIT COL AGAIN.
SOF
PAU
SFN=DFN+1
OFN=SFN
RFN=DFN+4
CLS
MOR
SON
OMD
TRANSFORMING DATA--MAY RETURN TO BACKGROUND POSITION IF DESIRED
SOF
OMD
TIMES FOR SAMPLE
STS
MTS
FPR
SFN=RFN
MSD
RAD
ASD
DSD
OMD
DFN IS RATIOED SPECTRA, IG IN RFN, SFN=DFN+4=NONRATIOED SPECTRA
PRN SFN
PRN DFN
RFN=DFN+1
PRN RFN
OMD
ENTER TITLE
TIR
OMD
THE LAST FILE YOU ARE PRESENTLY USING IS OFN
OFN=DFN+2
PRN OFN
END
```

137

Table XIII
BK1-Background collect one macro

```
:LST BK1
SON
OMD
PUT HELITRAN IN BACKGROUND POSITION--HIT RETURN
OMD
GAN NOT HIGH ENOUGH? CNTRL-S, RESET GAN AND HIT BK1 AGAIN
SOF
PAU
CFN=BFN
RFN=DFN+2
CLB
MOR
SON
OMD
TRANSFORMING DATA--MAY MOVE HELITRAN TO SAMPLE POSITION NOW
SOF
OMD
TIMES FOR BACKGROUND
STB
MTB
FPB
ASB
OMD
INTERFEROGRAM OF BACKGROUND IS IN REF FILE
PRN RFN
DSB
OMD
ENTER TITLE
TIR
END
```

Table XIV
BK2-Background collect two macro

```
:LST BK2
SON
OMD
MAKE SURE HELITRAN IS IN BACKGROUND POSITION,HIT RETURN
OMD
GAN NOT HIGH ENOUGH? CNTRL-S, RESET GAN, AND HIT BK2 AGAIN
SOF
PAU
SFN=DFN+4
MSD
RFN=DFN
BFN=DFN+3
OFN=2
SFN=DFN+4
MOS
CLB
SON
OMD
TRANSFORMING DATA--BEFORE AND AFTER BACKGROUNDS ADDED
OMD
DISPLAYED WILL BE DFN=SAMPLE/(BACKGROUNDS 1+2)
SOF
OMD
TIMES FOR SECOND BACKGROUND
STB
MTB
CMD
INTERFEROGRAM OF 2ND BACKGROUND IS IN BFN
PRN BFN
DFN=2
SFN=RFN+2
OFN=RFN+3
MSD
CAD
BFN=2
DFN=RFN
FPB
SFN=DFN+4
RAD
ASD
OMD
THE LAST FILE YOU ARE PRESENTLY USING IS RFN
RFN=DFN+3
PRN RFN
DSD
END
```

Table XV
PLT-Plot macro

```
:LST PLT
DSD
PRN XSL
PRN YSL
PAU FOLLOW PROCEDURE ON WALL--THEN RETURN
ZPN
PAD
PLD
PAU POSITION PEN FOR LABEL (OR STOP WITH CNTRL-S)
PAG=YS
PON
TID
STD
LPF
POF
ZPN
END
```

Table XVI
RNF-Renumber files macro

```
:LST RNF
OMD
OLD POSITIONS OF FILES
FLS
BFN=2
TEM=DFN
DFN=DFN+4
RFN=DFN+1
SFN=RFN+1
OFN=RFN
SON
OMD
NEW POSITIONS OF LABELLED FILES
RFN=RFN
FLS
SOF
END
```

140

David P. Svetz was born on 19 April 1951 in Greenville, South Carolina. He graduated from Punahou High School, Honolulu, Hawaii, in 1969 and attended Rensselaer Polytechnic Institute from which he received the degree of Bachelor of Physics in May 1973. Upon graduation, he received a commission in the USAF through the ROTC program. He attended Undergraduate Pilot Training at Williams AFB from which he received his pilot's wings in August 1974. He stayed at Williams AFB as a T-37 instructor pilot. He was assigned next to Beale AFB where he was an Aircraft Commander, Wing Training Flight Instructor Pilot, and Wing Standardization/Evaluation Instructor Pilot in the KC-135Q. He entered the School of Engineering, Air Force Institute of Technology, in June 1981. He is a member of the Order of Daedalians-National Fraternity of Military Pilots and Tau Beta Pi-National Engineering Honor Society.

          Permanent address: 6733 Hawaii Kai Dr.
                               Honolulu HI 96825

SECURITY CLASSIFICATION OF THIS PAGE *(When Data Entered)*

REPORT DOCUMENTATION PAGE	READ INSTRUCTIONS BEFORE COMPLETING FORM

1. REPORT NUMBER AFIT/GEP/PH/82D-22	2. GOVT ACCESSION NO. AD-A124 679	3. RECIPIENT'S CATALOG NUMBER

4. TITLE *(and Subtitle)* FAR-INFRARED PHOTOCONDUCTIVITY OF HIGH PURITY n-GaAs IN A MAGNETIC FIELD USING RAPID-SCAN FOURIER TRANSFORM SPECTROSCOPY	5. TYPE OF REPORT & PERIOD COVERED MS Thesis
	6. PERFORMING ORG. REPORT NUMBER

7. AUTHOR(s) David P. Svetz Capt	8. CONTRACT OR GRANT NUMBER(s)

9. PERFORMING ORGANIZATION NAME AND ADDRESS Air Force Institute of Technology (AFIT-EN) Wright-Patterson AFB, Ohio 45433	10. PROGRAM ELEMENT, PROJECT, TASK AREA & WORK UNIT NUMBERS

11. CONTROLLING OFFICE NAME AND ADDRESS Air Force Avionics Laboratory (AFWAL/AADR) Wright-Patterson AFB, Ohio 45433	12. REPORT DATE December 1982
	13. NUMBER OF PAGES 161

14. MONITORING AGENCY NAME & ADDRESS *(if different from Controlling Office)*	15. SECURITY CLASS. *(of this report)* Unclassified
	15a. DECLASSIFICATION/DOWNGRADING SCHEDULE

16. DISTRIBUTION STATEMENT *(of this Report)*

Approved for public release; distribution unlimited

17. DISTRIBUTION STATEMENT *(of the abstract entered in Block 20, if different from Report)*

18. SUPPLEMENTARY NOTES

Approved for public release: IAW AFR 190-17.

LYNN E. WOLAVER
Dean for Research and Professional Development
Air Force Institute of Technology (AIC)
Wright-Patterson AFB OH 45433

19 JAN 3

19. KEY WORDS *(Continue on reverse side if necessary and identify by block number)*
Gallium Arsenide
Fourier Transform Spectroscopy
Far-Infrared Photoconductivity
Photoconductivity in a Magnetic Field

20. ABSTRACT *(Continue on reverse side if necessary and identify by block number)*
The donor impurities in high purity n-GaAs can be described using a hydrogenic model. In a magnetic field the hydrogenic donor levels will split and the chemical shifts of the 1s-2p Zeeman transitions between donor states can be used to identify the impurities. The 1s-2p ($m=\pm1$) transitions are the strongest and best to use to identify the impurities. A rapid-scan Fourier transform spectrometer is used in conjunction with gold coated lightguide optics and a 125kG superconducting magnet

DD _{1 JAN 73} FORM 1473   EDITION OF 1 NOV 65 IS OBSOLETE

SECURITY CLASSIFICATION OF THIS PAGE *(When Data Entered)*

to obtain photoconductivity spectra. The experiemntal arrangement and procedure are described in detail. The necessary experiemntal data that had to be obtained on equipment, filters, temperature and electrical properties of GaAs to include carbon resistor resistances at cryogenic temperatures, spectral response of low pass optical filters, current-voltage characteristics of GaAs, Hall measurements, GaAs resistance versus temperature, and the best computer spectrum collection parameters for a Nicolet 8000 Fourier Transform Spectrometer are discussed. Zero field spectra from a sample with a carrier concentration of $1.25 \times 10^{14} cm^{-3}$ and liquid nitrogen mobility of 1.5×10^5 $cm^2/V\text{-sec}$ are presented and discussed along with the problems in setting up the experiment and obtaining spectra in a magnetic field.

END

FILMED

3-83

DTIC